PolyPublie
Polytechnique Montréal

POLYTECHNIQUE MONTRÉAL
UNIVERSITÉ D'INGÉNIERIE

Titre: Title:	Effect of Selective Oxidation on Temperature Measurements of AHSS with Pyrometry
Auteur: Author:	Quentin Somveille
Date:	2018
Type:	Mémoire ou thèse / Dissertation or Thesis
Référence: Citation:	Somveille, Q. (2018). Effect of Selective Oxidation on Temperature Measurements of AHSS with Pyrometry [Master's thesis, École Polytechnique de Montréal]. PolyPublie. https://publications.polymtl.ca/3084/

Document en libre accès dans PolyPublie
Open Access document in PolyPublie

URL de PolyPublie: PolyPublie URL:	https://publications.polymtl.ca/3084/
Directeurs de recherche: Advisors:	Myriam Brochu, & Kyle J. Daun
Programme: Program:	Génie mécanique

Ce fichier a été téléchargé à partir de PolyPublie, le dépôt institutionnel de Polytechnique Montréal
This file has been downloaded from PolyPublie, the institutional repository of Polytechnique Montréal

https://publications.polymtl.ca

UNIVERSITÉ DE MONTRÉAL

EFFECT OF SELECTIVE OXIDATION ON TEMPERATURE MEASUREMENTS OF AHSS WITH PYROMETRY

QUENTIN SOMVEILLE

DÉPARTEMENT DE GÉNIE MÉCANIQUE

ÉCOLE POLYTECHNIQUE DE MONTRÉAL

MÉMOIRE PRÉSENTÉ EN VUE DE L'OBTENTION

DU DIPLÔME DE MAÎTRISE ÈS SCIENCES APPLIQUÉES

(GÉNIE MÉCANIQUE)

AVRIL 2018

© Quentin Somveille, 2018.

UNIVERSITÉ DE MONTRÉAL

ÉCOLE POLYTECHNIQUE DE MONTRÉAL

Ce mémoire intitulé :

EFFECT OF SELECTIVE OXIDATION ON TEMPERATURE MEASUREMENTS OF AHSS WITH PYROMETRY

présenté par : SOMVEILLE Quentin

en vue de l'obtention du diplôme de : Maîtrise ès sciences appliquées

a été dûment accepté par le jury d'examen constitué de :

M. MARTINU Ludvik, Ph. D., président

Mme BROCHU Myriam, Ph. D., membre et directeur de recherche

M. DAUN Kyle J., Ph. D., membre et codirecteur de recherche

M. GROULX Dominic, Ph. D., membre

ACKNOWLEDGEMENTS

I would like to first thank the GAP (Galvanized Autobody Partnership) program, the NSERC (Natural Sciences and Engineering Research Council) and Polytechnique Montréal for funding this project. I also thank the members of the jury for accepting to read and evaluate my dissertation. I would also like to hugely thank my supervisor and co-supervisor, Professor Myriam Brochu and Professor Kyle Daun, for accepting to supervise my Master's project, for their precious help, their patience, their encouragements and their advice. I also thank Michel Dubois for his advice, Bill Baloukas for his help during the emissivity measurements and his precious tips and Patricia Moraille for the AFM measurements and her information.

I specially thank Paul Mosser, who also worked on the project, for his support all along my work and for his patience when he had to bear me in Japan.

I thank my family and my friends for their support despite the distance, especially my Sweetie pie and l'Archi Dudu. Finally, I want to thank the other students in the office for the great atmosphere: Paul and Paul, Cécile, Simon, Reza and Meyssam (aka Jigar).

Je tiens à remercier tout d'abord le programme GAP (Galvanized Autobody Partnership), le CRSNG (Conseil de recherches en sciences naturelles et en génie du Canada) et Polytechnique Montréal pour le financement du projet. Je remercie également les membres du jury qui ont bien voulu accepter de lire et évaluer mon mémoire. Je voudrais aussi énormément remercier ma directrice et mon co-directeur de recherche, la Professeure Brochu et le professeur Kyle Daun, pour avoir accepté de diriger ma maîtrise, pour leur aide précieuse, leur patience, leurs encouragements et leurs conseils. Merci également à Michel Dubois pour ses conseils; à Bill Baloukas pour son aide lors des mesures d'émissivité et ses précieux conseils et à Patricia Moraille pour les manipulations d'AFM et ses informations.

Je remercie spécialement Paul Mosser, qui a travaillé aussi sur le projet, pour son soutien tout au long de mon travail et sa patience pour m'avoir supporté au Japon.

Merci à ma famille et mes proches pour leur soutien malgré la distance parfois, en particulier ma Sweetie pie et l'Archi Dudu. Enfin, je tiens à remercier les autres étudiants du bureau pour la super ambiance qui y règne : Paul et Paul, Cécile, Simon, Reza et Meyssam (aka Jigar).

RÉSUMÉ

Le contrôle précis de la température dans les fours de traitement thermique sur les lignes de galvanisation continue est essentiel pour l'obtention des propriétés mécaniques désirées des aciers galvanisés. Des capteurs sans contact, typiquement des pyromètres monochromatiques ou polychromatiques, sont employés pour le contrôle de température. Les mesures de ces instruments sont influencées par l'émissivité du matériau traité, qui est elle-même sensible aux caractéristiques surfaciques comme la rugosité or l'oxydation sélective de surface.

Le travail présenté examine l'impact de la composition chimique du métal de base, de la rugosité de surface et de l'oxydation sur l'émissivité spectrale de deux grades d'aciers biphasés (DP) laminés à froid : le DP780 et le DP980. Un cycle de traitement thermique, représentatif du revenu intercritique effectué dans les fours industriels, a été appliqué aux deux alliages à l'aide d'un simulateur de galvanisation continue dans lequel l'atmosphère est composée de 95% N_2 et 5% H_2, avec un point de rosée de -30°C. Les cycles thermiques ont été interrompus à différents instants et les tôles ont été rapidement refroidies avec de l'azote dans le but d'observer l'évolution de l'oxydation au cours du cycle de revenu intercritique et son impact sur l'émissivité.

L'émissivité spectrale des échantillon obtenus a été mesurée à température ambiante et pour des longueurs d'onde entre 0.6 et 25 μm. Les résultats indiquent que l'émissivité spectrale du DP780 varie plus lors du revenu intercritique que celle du DP980. L'émissivité spectrale augmente pour les courtes longueurs d'onde (< 2 μm) et diminue pour les grandes longueurs d'onde (> 2.5 μm) avec la croissance d'oxyde. La différence de comportement provient des différentes interactions physiques entre les ondes électromagnétiques et la surface de l'échantillon, en fonction de l'échelle de la rugosité par rapport à la longueur d'onde de la lumière. Les résultats d'émissivité sont comparés à des observations de la topographie de surface (SEM) et à des profils chimiques (GDOES). Ces mesures montrent que l'oxyde externe est plus visible et plus épais dans le cas du DP780, par rapport au DP980. La différence de composition chimique, et en particulier le rapport Mn/Si peut expliquer ces différences de comportement entre les deux grades d'aciers biphasés.

Le point de rosée de l'atmosphère du four de chauffe a été modifié de façon à étudier l'effet de la concentration en oxygène dans l'atmosphère sur l'oxydation et l'émissivité spectrale. Le changement du point de rosée de -30°C à 0°C réduit l'oxydation de surface et les variations d'émissivité au cours du cycle. L'augmentation de la concentration en oxygène dans l'atmosphère

provoque la transition d'oxydation externe à oxydation interne. Dans le cas du DP980, modifier le point de rosée a peu d'effet sur l'émissivité spectrale. Il est possible que la transition d'oxydation externe à interne pour le DP980 ait lieu à un point de rosée inférieur à -30°C.

L'émissivité spectrale du DP980 a été mesurée à haute température dans un Gleeble pour se rapprocher des conditions industrielles et étudier expérimentalement l'effet de la température sur l'émissivité spectrale. Un contrôle inadéquat de l'atmosphère a produit des conditions d'oxydation différentes de celles du simulateur de galvanisation. Il est donc inapproprié de comparer l'émissivité spectrale de l'acier traité dans le simulateur de galvanisation et dans le Gleeble.

Les changements d'émissivité spectrale peuvent induire des écarts de température. Ces écarts ont été estimées théoriquement autour de ±45°C pour le DP780 et ±10°C pour le DP980 à une température de 800°C et pour des longueurs d'onde entre 1 et 2.5 µm, en considérant la pyrométrie monochromatique. Ces écarts de température sont réduits pour le DP780 lorsque le point de rosée est augmenté de -30°C à 0°C, du fait de la plus grande stabilité de l'émissivité spectrale du DP780 durant le traitement thermique avec un point de rosée de 0°C.

Cette étude a permis de comprendre l'effet de l'oxydation sélective de l'acier sur l'émissivité spectrale des AHSS, et son impact sur les mesures de température par pyrométrie. La croissance d'oxyde modifie l'émissivité spectrale des aciers et induit des erreurs dans les mesures de température par pyrométrie pouvant atteindre jusqu'à ±45 °C. Ce travail constitue la base pour de futures caractérisations de surface à haute température dans une atmosphère correspondante à celle des lignes industrielles et pour la modélisation de l'émissivité spectrale durant le cycle thermique dans le but d'anticiper les évolutions d'émissivité spectrale ainsi que les possibles écarts de température dans le but d'améliorer le contrôle de la température des aciers.

ABSTRACT

Precise steel temperature control in the soaking furnaces within the continuous galvanizing lines is essential for obtaining the desired mechanical properties of galvanized steel. Non-contact sensors, typically single and multi-wavelength pyrometers, are used for temperature control. The readings by these instruments are influenced by the spectral emissivity of the heat treated material, which is sensitive to surface characteristics like roughness or surface selective oxidation.

The present work investigates the impact of the chemical composition of the base steel, surface roughness and oxidation, on the steel spectral emissivity and temperature measurements by pyrometry. The study focuses on two grades of cold rolled dual phase (DP) steel: DP780 and DP980. A heat treatment cycle representative of intercritical annealing performed in the industrial furnaces was applied to coupons of both alloys, using a galvanizing simulator in which the atmosphere was composed of 95% N_2 and 5% H_2, with a dew point of -30. The heat cycles were interrupted at various points and coupons rapidly quenched with nitrogen to observe the evolution of oxidation during the intercritical annealing cycle and its impact on emissivity.

The spectral emissivity of the extracted coupons were measured at room temperature for wavelengths between 0.6 and 25 µm. Results indicate that the spectral emissivity of DP780 varies more during intercritical annealing than that of DP980. Spectral emissivity increases at short wavelengths (< 2 µm) and decreases at long wavelengths (> 2.5 µm) with the growth of oxide. The different behavior is explained by different physical interactions between electromagnetic waves and the surface, depending on the roughness length scale compared to the wavelength of light. Spectral emissivity results are compared with topography observations (SEM) and elemental profile measurements (GDOES). These measurements showed that external oxide is more visible and thicker for DP780 compared to DP980. These differences between these two dual phase steel grades originate from the different alloy composition, and especially the Mn/Si ratio.

The furnace atmosphere dew point was modified in order to investigate the effect of the atmosphere oxygen concentration on oxidation and spectral emissivity. Changing the dew point from -30°C to 0°C reduces surface oxidation and variations in spectral emissivity during the cycle. The increase in the atmosphere oxygen concentration causes the transition from external to internal oxidation. In the case of DP980, modifying the dew point has little impact on spectral emissivity. It is possible

than transition from external to internal oxidation happens at a lower dew point than -30 °C for DP980.

Spectral emissivity of DP980 was measured at high temperature in a Gleeble in order to simulate the industrial conditions and investigate experimentally the effect of temperature on emissivity. Inadequate atmosphere control induced oxidation conditions different from the ones in the galvanizing simulator. Therefore, it is inappropriate to compare spectral emissivity of steel annealed in the galvanizing simulator and in the Gleeble.

The changes in spectral emissivity can induce temperature deviations. These deviations were estimated theoretically around ±45°C for DP780 and ±10°C for DP980 at a temperature of 800°C for wavelengths between 1 and 2.5 µm, assuming single-wavelength pyrometry. Temperature deviations are reduced for DP780 when the dew points increases from -30 °C to 0 °C, because of the better stability of DP780 spectral emissivity during the heat cycle with a dew point of 0 °C.

This study elucidates the effect of steel selective oxidation on the spectral emissivity of advanced high strength steels during intercritical annealing, and its impact on pyrometrically-infered temperature measurements. The growth of oxide modifies spectral emissivity of the steels and induces errors in temperature measurements by pyrometry that can reach ±45 °C. This work is the basis for future surface characterizations at high temperature in an atmosphere relevant to the one of the industrial lines and spectral emissivity modeling during the heat cycle in order to anticipate spectral emissivity evolution as well as possible temperature excursions with the aim of improving steel temperature control.

TABLE OF CONTENTS

ACKNOWLEDGEMENTS III

RÉSUMÉ IV

ABSTRACT VI

TABLE OF CONTENTS VIII

LIST OF TABLES XI

LIST OF FIGURES XII

LIST OF SYMBOLS AND ABBREVIATIONS XVI

LIST OF APPENDICES XX

CHAPTER 1 INTRODUCTION 1

1.1 Context 1

1.2 Objective and Plan 5

CHAPTER 2 LITERATURE REVIEW 6

2.1 Temperature Measurement by Pyrometry 6

2.1.1 Single-Wavelength (SWL) Pyrometry 6

2.1.2 Dual-Wavelength (DWL) Pyrometry 8

2.1.3 Multi-Wavelength (MWL) Pyrometry 9

2.2 Selective Oxidation of AHSS During Intercritical Annealing 11

2.2.1 Intercritical Annealing 11

2.2.2 AHSS Selective Oxidation 13

2.2.3 Oxidation Control Methods 19

2.3 Emissivity of AHSS 23

2.3.1 Influence of Temperature 23

2.3.2 Influence of Oxide Films 24

2.3.3 Influence of Roughness 26
2.4 Synthesis 29
CHAPTER 3 EXPERIMENTAL METHODOLOGY 31
3.1 Results of the Industrial Survey 31
3.2 Sample Procurement 33
3.3 Measurements 35
3.3.1 Spectral Emissivity 36
3.3.2 Surface Alterations 41
3.4 Results Presentation Organization 46
CHAPTER 4 ARTICLE I: EFFECT OF OXIDATION ON EMISSIVITY FOR DP780 AND DP980 STEELS 47
4.1 Abstract 47
4.2 Introduction 47
4.3 Experimental Protocol 49
4.4 Results 53
4.4.1 Emissivity Results 53
4.4.2 GDOES Results 55
4.4.3 Roughness Results 57
4.4.4 Scanning Electron Microscopy 58
4.5 Discussion 60
4.6 Conclusions and Future Work 61
4.7 Acknowledgements 62
CHAPTER 5 SPECTRAL EMISSIVITY AND CONNECTION TO SURFACE STATE 63
5.1 Complements to the Article 63
5.1.1 GDOES Measurements 63

5.1.2 Topography Analysis 66
5.2 Change in Atmospheric Dew Point During Annealing 69
5.3 Spectral Emissivity Measurements Robustness Investigation 73
5.4 High-Temperature Spectral Emissivity Measurements 75
5.5 Coupon Temperature Inhomogeneity 80
5.6 Synthesis 82
CHAPTER 6 GENERAL DISCUSSION 83
6.1 Effect of Spectral Emissivity Evolution during Intercritical Annealing 83
6.2 Effect of Changing the Dew point 85
6.3 Effect of Temperature Inhomogeneity 86
6.4 Synthesis 88
CHAPTER 7 CONCLUSION AND RECOMMENDATIONS 89
7.1 Conclusions 89
7.2 Recommendations for Future Work 92
BIBLIOGRAPHY 94
APPENDICES 99

LIST OF TABLES

Table 2-1: Summary of pyrometry methods 11

Table 2-2: Example minimum mechanical properties required by standard ASTM A1079 for DP980 12

Table 3-1: Summary of the survey results 32

Table 3-2: Maximum acceptable compositions of DP780 and DP980 according to the ASTM A1079 standard [17] (maximum weight percent) 33

Table 3-3: Chemical Mn/Si ratio of DP780 and DP980 33

Table 3-4: Times and temperatures at which the cycles were interrupted 35

Table 3-5: Characteristics of the emissivity measurements instruments 39

Table 3-6: Matrix of room temperature spectral emissivity measurements 40

Table 3-7: GDOES operating parameters 41

Table 3-8: XPS operating parameters 42

Table 3-9: Matrix of chemical analyses 43

Table 3-10: Matrix of topography analysis 45

Table 3-11: Summary of the measurements presented in the thesis 45

Table 4-1: Maximal chemical composition of DP780 and DP980 [17] 50

Table 4-2: Chemical atomic composition of our steels 50

Table 4-3: Summary of the temperature at which the heat treatments were interrupted 51

LIST OF FIGURES

Figure 1-1: Mechanical properties of HSS and AHSS [2] 1

Figure 1-2: Schematic of a typical continuous hot-dip galvanizing line [1] 2

Figure 1-3: Illustration of wedge method pyrometry [3] 3

Figure 1-4: Temperature measurement in steel strips using the wedge method © 2011, IEEE [5] 4

Figure 1-5: Schematic of the use of a reflector for pyrometry applications © 2017, IEEE [4] 4

Figure 2-1: Microstructure of DP980 steel after intercritical annealing [16] 12

Figure 2-2: Ellingham diagram for several alloying elements of AHSS. Adapted from Buscarlet [19] 15

Figure 2-3: GDOES depth profile of Mn in a CMnAl TRIP steel after annealing, for several temperatures [25] 16

Figure 2-4: Schematic of different oxide morphologies ((a): vein-shaped; (b): elongated; (c): lens-shaped) [22] 17

Figure 2-5: Transport mechanisms in a dense oxide layer [37] 18

Figure 2-6: Variation of oxygen partial pressure as a function of temperature for several dew points [18] 20

Figure 2-7: TEM micrographs of CMnSi AHSS annealed with a DP of -50 °C ((a): overview of oxides; (b): elemental maps of zone A) [31] 21

Figure 2-8: TEM micrographs of CMnSi AHSS annealed with a DP of -30 °C ((a): overview of oxides in the cross-section; (b): detailed view of zone A; (c): detailed view of zone B; (d): elemental maps of zone B) [31] 21

Figure 2-9: Cross-section of a metallic substrate and oxide film [50] 25

Figure 2-10: Evolution of Armco iron spectral emissivity with time during heating [50] 25

Figure 2-11: Schematic illustrations of profiles with various R_q, skewness and kurtosis [63, 64] 28

Figure 2-12: Correlation of local scale roughness and global emissivity [61] 29

Figure 3-1: Intercritical annealing cycles applied to the steels 34

Figure 3-2: Schematic of a coupon that was processed in the simulator 35

Figure 3-3: Spectral reflectivity of Spectralon 37

Figure 4-1: Heat cycles applied to the steels (blue: DP780; red: DP980). 51

Figure 4-2: Schematic illustrations of profiles with various R_q, skewness and kurtosis [63] 52

Figure 4-3: DP780 emissivity results for both devices. “A”, “B”, and “Full” correspond to points in Figure 4-1, while “AR” denotes the as-received samples 54

Figure 4-4: DP980 emissivity results for both devices. “A”, “B”, and “Full” correspond to points in Figure 4-1, while “AR” denotes the as-received samples 54

Figure 4-5: Concentration profiles for DP980 B, obtained by GDOES 56

Figure 4-6: Oxide thickness on DP780 and DP980 using criterion $CO < 10\%_{at.}$ measured from GDOES data 56

Figure 4-7: Evolution of the surface atomic Mn/Si ratio throughout the heat treatment measured from GDOES data 56

Figure 4-8: Evolution of R_q, R_{sk} and R_{ku} for both materials during the heat treatment 57

Figure 4-9: SEM images of DP780 (as-received on the left, “A” on the right) 59

Figure 4-10: SEM images of DP980 (as-received on the left, “Full” on the right) 59

Figure 5-1: Surface elemental profiles obtained with GDOES ((a) and (b): DP980 “AR”; (c) and (d): DP780 “AR”; (e) and (f): DP780 “B”) 64

Figure 5-2: Oxide thickness on DP780 and DP980 for all conditions, from GDOES data 65

Figure 5-3: Atomic Mn/Si ratio for all conditions, from GDOES data 65

Figure 5-4: White light interferometry (WLI) results for DP780 “AR” and “Full” 67

Figure 5-5: Roughness measured by white light interferometry 67

Figure 5-6: Atomic force microscopy (AFM) micrographs on DP780 “AR” and “Full DP -30 °C” 68

Figure 5-7: Comparison of the spectral emissivities of “Full” specimens of DP780 for both instruments and dew points of -30 °C and 0 °C 70

Figure 5-8: Comparison of the spectral emissivities of “Full” specimens of DP980 for both instruments and dew points of -30 °C and 0 °C 70

Figure 5-9: Observation of the oxide layer of galvanized DP980 71

Figure 5-10: Influence on oxide thickness of changing the dew point 72

Figure 5-11: Influence on Mn/Si ratio of changing the dew point 72

Figure 5-12: Comparison of the results of three identical measurements with the SOC-100 73

Figure 5-13: Comparison of the emissivities of two samples of as-received DP780 74

Figure 5-14: Comparison of the emissivities of both faces of a sample of as-received DP980 (continuous upper curves: matte face; dashed lower curves: striped face) 75

Figure 5-15: Heat cycle applied to the steel in the Gleeble 76

Figure 5-16: Spectral normal emissivity in argon of DP980 as a function of temperature and wavelength 77

Figure 5-17: Spectral normal emissivity in argon at λ=2 µm of DP980 as a function of temperature 77

Figure 5-18: Comparison of spectral emissivity at room temperature of DP980 after annealing in the simulator and in the Gleeble 78

Figure 5-19: Ellingham diagram describing oxidation in the Gleeble [19] 79

Figure 5-20: Diagram indicating Regions (1) and (2) where samples were cut on the coupon to study temperature heterogeneity 80

Figure 5-21: Comparison of spectral emissivity of DP780 “AR” measured in Regions (1) and (2) in Figure 5-20 for DP780 “Full” 81

Figure 6-1: Spectral emissivity of DP780 “AR” and “Full” between 1 and 2.5 µm 83

Figure 6-2: Spectral emissivity of DP980 “AR” and “Full” between 1 and 2.5 µm 83

Figure 6-3: Expectable temperature errors for single-wavelength pyrometry 84

Figure 6-4: Effect of the change in dew point on the spectral emissivity of DP780 between 1 and 2.5 µm 85

Figure 6-5: Effect of the change in dew point on the spectral emissivity of DP980 between 1 and 2.5 µm 85

Figure 6-6: Expectable temperature errors for single-wavelength pyrometry when changing the dew point 86

Figure 6-7: Effect of steel temperature inhomogeneity during annealing on the spectral emissivity of DP780 between 1 and 2.5 µm 87

Figure 6-8: Expectable temperature errors in Regions (1) and (2) for single wavelength pyrometry 88

LIST OF SYMBOLS AND ABBREVIATIONS

α'_λ	Directional spectral absorptivity
α	Absorptivity
ΔG^0	Standard Gibbs free reaction energy (kJ)
ΔG	Gibbs free reaction energy (kJ)
ΔT	Temperature deviation
$\varepsilon_{\overline{\lambda}}$	Global emissivity
ε'_λ	Directional spectral emissivity
$\varepsilon'_{\lambda,s}$	Directional spectral emissivity set in the pyrometer
$\varepsilon'_{\lambda,t}$	True directional spectral emissivity
ε_r	Total emissivity of a rough specimen
ε_s	Total emissivity of a smooth specimen
λ	Wavelength (μm)
μ_0	Magnetic permeability of vacuum ($4\pi\times10^{-7}$ N/A^{-2})
ρ	Reflectivity
ρ'_λ	Directional spectral reflectivity
$\rho'_{\lambda-d/h}$	Spectral directional-hemispherical reflectivity
$\rho'_{\lambda-d/h,meas}$	Measured Directional-hemispherical reflectivity
$\rho'_{\lambda-d/h,true}$	True Directional-hemispherical reflectivity
$\rho'_{\lambda-h/d}$	Spectral hemispherical-directional reflectivity
$\rho'_{\lambda-h/d,meas}$	Measured hemispherical-directional reflectivity
$\rho'_{\lambda,\mathrm{Spect}}$	Directional spectral reflectivity of Spectralon

τ	Transmittivity
Ac_1, Ac_3	Steel transformation temperatures
AFM	Atomic force microscopy
AHSS	Advanced high-strength steel
AR	As-received
ASTM	American Society for Testing and Materials
BDRF	Bi-directional reflection function
c_0	Speed of light in vacuum (2.998×10^8 m/s)
C_1	$2\ h\ c_0^2 = 1.191\times10^{-16}$ W·m^2/sr
C_2	$h\ c/k_B = 1.439\times10^{-2}$ m·K
C_λ	Calibration constant
Cfdl	Confidential
CGL	Continuous galvanizing line
CP	Complex phase
DP	Dual phase
DP	Dew point
DWL	Dual-wavelengths
E	Total hemispherical emissive power
$E_{b\lambda}$	Hemispherical spectral emissive power (W/m^2·µm)
EDS	Energy-dispersive spectroscopy
F	Roughness factor
FIB	Focused ion beam
FTIR	Fourier transform infrared
GAP	Galvanized Autobody Partnership

GDOES	Glow-discharge optical emission spectroscopy
h	Planck's constant (6.626×10^{-34} J·s)
HSLA	High strength low alloy
HSS	High-strength steel
I'_λ	Directional spectral intensity (W/m^2·µm·sr)
$I'_{b\lambda}$	Blackbody directional spectral intensity (W/m^2·µm·sr)
$I'_{\lambda,r}$	Intensity reflected by the sample
$I'_{\lambda,r,\mathrm{gold}}$	Intensity reflected by the gold reference
$I'_{\lambda,r,\mathrm{Spect}}$	Intensity reflected by Spectralon
IZA	International Zinc Association
J'_λ	Directional spectral incandescence (W/m^2·µm·sr)
k_B	Boltzmann's constant (1.381×10^{-23} J/K)
LABe	Low angle backscatter electron
LaRFIS	Laboratoire des Revêtements Fonctionnels et Ingénierie
LWIR	Long-wavelength infrared
MART	Martensitic
MGS	McMaster Galvanizing Simulator
MWIR	Mid-wavelength infrared
MWL	Multi-wavelengths
NSERC	Natural Sciences and Engineering Council of Canada
$p_{\mathrm{sat,H_2O}}$	Saturation vapor pressure of water
$p_{\mathrm{H_2}}$	Partial pressure of molecular hydrogen
p_{O_2}	Partial pressure of molecular oxygen
R_a	Arithmetical average of the profile

r_e	Electrical resistivity (Ω·cm)
$r_{e,273}$	Electrical resistivity at 273 K (Ω·cm)
ReFaST	Reflector with a Fast Switching Tube
R_{ku}	Kurtosis of the profile
RMS	Root mean square
R_{sk}	Skewness of the profile
R_q	RMS of the profile
SEM	Scanning electron microscope
SWL	Single-wavelength
T	Temperature
T_m	Measured temperature
T_t	True temperature
TEM	Transmission electron microscope
TRIP	Transformation induced plasticity
WLI	White light interferometry
XPS	X-ray photoelectron spectroscopy

LIST OF APPENDICES

Appendix A – THERMAL RADIATION BASICS.....99

Appendix B – QUESTIONNAIRE SENT TO THE INDUSTRIAL PARTNERS.....105

Appendix C – RESULTS OF THE SURVEY 107

Appendix D – GDOES PROFILES 108

Appendix E – ILLUSTRATION OF THREE REGIMES OF INTERACTIONS BETWEEN SPECTRAL EMISSIVITY AND ROUGHNESS.....110

CHAPTER 1 INTRODUCTION

1.1 Context

With global warming escalating, green-house gas vehicle emission regulations are becoming more and more stringent. Consequently, car manufacturers' response is to decrease the weight of the vehicles. This vehicle lightweighting can be performed by developing new materials like advanced high-strength steels (AHSS). Due to their superior mechanical properties compared to conventional high strength steels (HSS), lighter parts can be produced having the same strength and crash performance [1]. Figure 1-1 presents elongation and tensile strength of different kinds of HSS and AHSS. AHSS were developed with two main goals: obtaining very high tensile strength for the vehicle safety cage parts by developing martensitic (MART) steels; and obtaining better energy absorption capacity for crumple zone parts by developing transformation-induced plasticity (TRIP), complex phase (CP) steels or dual phase (DP) steels, which are the focus of the present study.

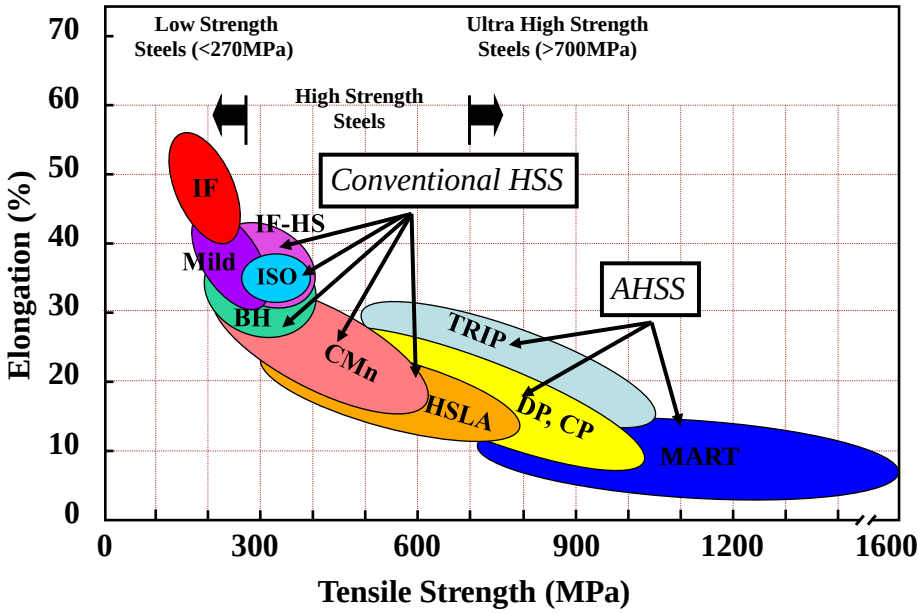

Figure 1-1: Mechanical properties of HSS and AHSS [2]

In order to obtain the required mechanical properties reported in Figure 1-1, heat treatments are applied to the steels. Steels are also galvanized to be protected from corrosion. One common galvanizing process consists in dipping the metal in liquid zinc after the annealing furnace. Heat

treatment and galvanizing steps are often performed back-to-back in a continuous galvanizing line (CGL). Figure 1-2 presents a schematic of CGL with the different steps. First, the new coil is welded to the one already in the line. Then, it is cleaned, annealed, cooled down to the temperature of liquid zinc and dipped in the zinc bath. Finally, finishing treatments are applied and the steel is coiled again.

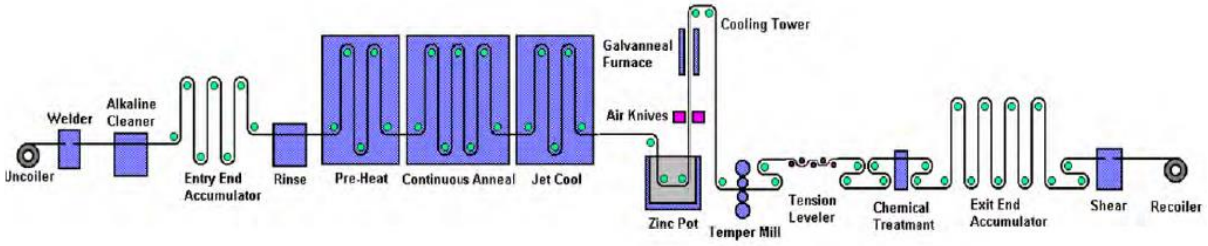

Figure 1-2: Schematic of a typical continuous hot-dip galvanizing line [1]

Given that the process is continuous, it is not possible to measure temperature in the annealing furnace using contact sensors. Therefore, temperature control is ensured by pyrometry, in which the temperature of a body is inferred from its incandescence. The complexity of this method is that it requires precise knowledge of the steel spectral emissivity to deliver accurate temperature readings. However, the steel oxidizes within the annealing furnace, changing surface roughness and surface chemical composition. This evolving surface state modifies the steel spectral emissivity and leads to measurement errors and steel temperature excursions. Consequently, at the end of the process, the required mechanical properties may not have been reached.

Different solutions allow to compensate for spectral emissivity uncertainty. A common solution is to perform wedge method pyrometry. Wedge method pyrometry consists of pointing the pyrometer at the wedge formed between a roll and a steel sheet in the industrial line, as illustrated in Figure 1-3. Due to the absorption and multiple reflections of light in this area, the wedge tends to create a local blackbody and the emissivity in that zone will be close to unity.

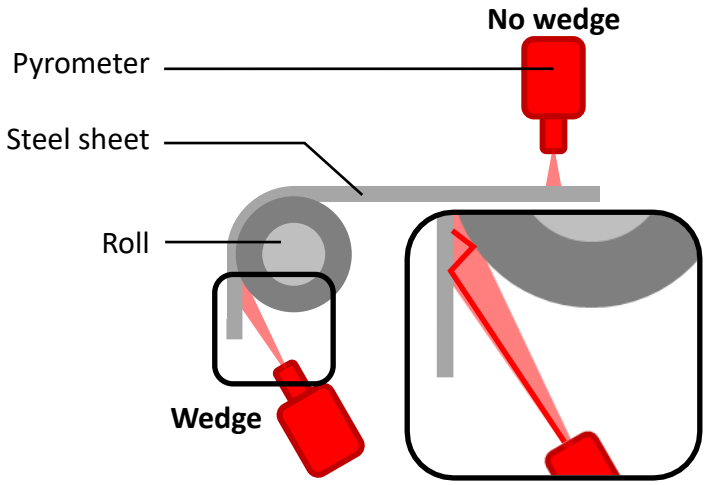

Figure 1-3: Illustration of wedge method pyrometry [3]

Figure 1-4 shows an example of an image taken with a thermal imaging camera. We can notice that the apparent temperature is higher in the wedge. This is due to an increase in emissivity; at the same temperature, this zone emits more radiation and its temperature seems higher through the camera. Setting up this method can be delicate since it requires good accessibility to the wedge and high precision in pointing the pyrometer. Furthermore, the wedge area might be smaller than the spot analyzed by the pyrometer. Thus, the apparent emissivity of the area targeted by the pyrometer can differ from unity and it can lead to temperature deviations up to 40 °C at 800 °C.

Another strategy to increase the apparent spectral emissivity in order to form a local blackbody is to equip the pyrometer with a reflecting mirror or “gold cup” as illustrated in Figure 1-5 [4]. The reflector is made with a highly reflective material, usually gold. It is placed over the surface so that its focal point is at the same height as the surface, where the pyrometer aims. Due to the multiple reflections between the measured surface and the surface of the reflector, emissivity at the focal point increases and tends to 1, in a manner similar to a blackbody.

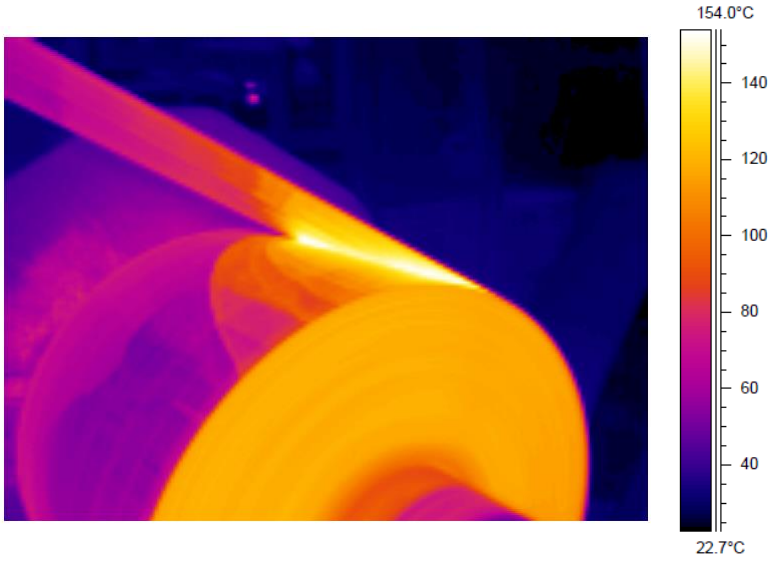

Figure 1-4: Temperature measurement in steel strips using the wedge method © 2011, IEEE [5]

One of the other issues with pyrometry measurements is that pyrometers actually measure the radiosity of the surface. The radiosity of the surface is the sum of the energy emitted by the sheet and the energy emitted by the walls of the furnace, reflected by the sheet into the pyrometer. The use of a reflector can help overcome this issue. If the mirror is cooled and is sufficiently reflective, only the radiation emitted by the measured surface will reach the pyrometer. Another common way to solve the problem of furnace radiation reflection is to use water-cooled sighting tubes around the pyrometer spot. These tubes only let radiation from the sheet reach the pyrometer. The radiation emitted by the tube itself is reduced owing to its water-cooling system.

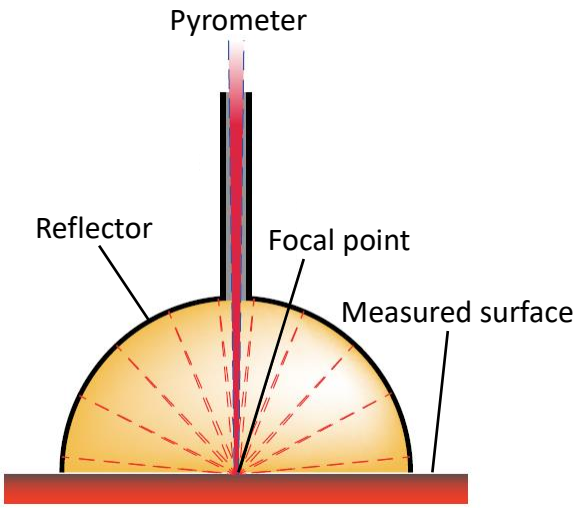

Figure 1-5: Schematic of the use of a reflector for pyrometry applications © 2017, IEEE [4]

1.2 Objective and Plan

The objective of the present study is to investigate the effect of intercritical annealing on steel radiative properties and temperature deviations for two dual phase steels (DP780 and DP980), in order to improve temperature control in the CGLs and reduce rejection rate, which can currently reach more than 30%. This research is part of the project ZCO-72 of the Galvanized Autobody Partnership (GAP). The GAP is an association of the steel, automobile and zinc industries and aims to improve the performance of galvanized AHSS for the automobile industry [6]. The GAP program is also part of the International Zinc Association (IZA), which contributes to improve the market and image of zinc [7]. The goals of the ZCO-72 project are to understand the influence of surface characteristics on temperature readings by pyrometry as well as investigating the effect of processing parameters during intercritical annealing on mechanical properties of AHSS and zinc coating at the end of the galvanizing line.

The present work starts with a review of the literature relevant to this project. Then, the article presented at the Galvatech 2017, gathering the main results of this project is shown, followed by additional results. Finally, a general discussion is proposed, before a conclusion and recommendations for future studies.

CHAPTER 2 LITERATURE REVIEW

The state of the art is presented here, beginning with an introduction to principles of pyrometry, followed by a presentation of AHSS oxidation phenomena during intercritical annealing. Then, the evolution of the emissivity of AHSS during intercritical annealing is investigated. Finally, a synthesis of the literature review exposes the research question.

2.1 Temperature Measurement by Pyrometry

As explained in the introduction, the continuous nature of the continuous galvanizing lines (CGL) prohibits measurement of the temperature of a component using contact sensors. Consequently, the temperature measurement method used in the CGL is pyrometry. Pyrometry estimates temperature by measuring radiative incandescence. Pyrometry methods can be classified by the number of wavelengths considered: single-wavelength (SWL), dual-wavelength (DWL), and multi-wavelength (MWL) pyrometry. Basics of thermal radiations, useful to understand pyrometry concepts, are presented in Appendix A.

2.1.1 Single-Wavelength (SWL) Pyrometry

Single-wavelength or monochromatic pyrometry is the most basic form of pyrometry [8]. Pyrometers in the CGL measure directional spectral incandescence of the steel, which is related to the steel temperature by

$$J'_\lambda(\lambda,T) = C_\lambda\, I'_\lambda(\lambda,T) = C_\lambda\, \varepsilon'_\lambda(\lambda,T)\, I'_{b\lambda}(\lambda,T) \tag{2-1}$$

where C_λ is a calibration constant that depends on the photoelectric efficiency of the detector, the detector solid angle, and the detector optics; I'_λ is the directional spectral intensity leaving the steel along a direction corresponding to the angle formed between the surface normal of the sheet steel and the detector view axis; ε'_λ is the directional spectral emissivity of the steel and where $I'_{b,\lambda}$ is the blackbody spectral intensity. The blackbody intensity follows Planck's law, with Wien's approximation,

$$I'_{b\lambda}(\lambda,T) = \frac{C_1}{\lambda^5\left(\exp\left(\frac{C_2}{\lambda\, T}\right)-1\right)} \approx \frac{C_1}{\lambda^5 \exp\left(\frac{C_2}{\lambda\, T}\right)} \tag{2-2}$$

where λ is the wavelength, T is temperature and where C_1 and C_2 are the constants $C_1 = 2\,h\,c_0^2 = 1.191\times10^{-16}$ W·m^2/sr and $C_2 = h\,c/k_B = 1.439\times10^{-2}$ m·K with h being Planck's constant (6.626×10^{-34} J·s), c_0 being the speed of light in vacuum (2.998×10^{8} m/s), k_B being Boltzmann's constant (1.381×10^{-23} J/K).

It is not physically possible to perform measurements for a single wavelength. Instead, pyrometers measure incandescence in a wavelength band. However, the wavelength bandwidth is narrow enough to consider that the measured intensity corresponds to a single wavelength value.

Temperature in Kelvins is calculated with Eqs. (2-1) and (2-2),

$$T = \frac{C_2}{\lambda \ln\left(\frac{C_1 C_\lambda \varepsilon'_\lambda}{\lambda^5 J'_\lambda}\right)} \tag{2-3}$$

It follows that the accuracy of a pyrometer will depend on the accuracy of the spectral emissivity estimation. Typically, the expected value of the spectral emissivity of the steel is input to the pyrometer. However, this spectral emissivity value may differ from the true spectral emissivity of the material. The pyrometer actually measures:

$$J'_\lambda = C_\lambda\, \varepsilon'_{\lambda,s}(\lambda, T_m)\, I'_{b,\lambda}(\lambda, T_m) = C_\lambda\, \varepsilon'_{\lambda,t}(\lambda, T_t)\, I'_{b,\lambda}(\lambda, T_t) \tag{2-4}$$

where $\varepsilon'_{\lambda,s}$ is the spectral emissivity value set in the pyrometer, T_m is the temperature measured by the pyrometer, $\varepsilon'_{\lambda,t}$ is the true spectral emissivity of the material and T_t is the true temperature of the material. The error in the temperature reading can be expressed as:

$$\frac{1}{T_m} - \frac{1}{T_t} = \frac{\lambda}{C_2} \ln\left(\frac{\varepsilon'_{\lambda,s}}{\varepsilon'_{\lambda,t}}\right) \tag{2-5}$$

Careful wavelength selection is critical for monochromatic pyrometry. Eq. (2-5) shows that the difference between T_m and T_t increases with wavelength. However, in order to maximize the signal/noise ratio, utilization of a short wavelength might not be optimal, especially at low temperatures. Wien's displacement law (cf. Appendix A) shows that the wavelength with the maximum intensity decreases with increasing temperature. Moreover, some atmospheric gases such as H_2O and CO_2 absorb light in specific ranges of wavelengths. This atmospheric absorption affects the pyrometry results and adds an error to the temperature readings. Consequently, the most

frequently used wavelengths for pyrometry are in the mid-wavelength infrared (MWIR) range (below 5 µm) and in the long-wavelength infrared (LWIR) range (8 to 14 µm) [9]. In these bands, atmospheric transmittance is maximized while limiting the influence of measurement noise and error.

As explained in the introduction, spectral emissivity uncertainties due to the furnace radiations reflected by the sheet into the pyrometers can be compensated by the wedge method [5] by using water cooled sighting tubes or gold cups [4].

2.1.2 Dual-Wavelength (DWL) Pyrometry

In the case of dual-wavelength or two-color pyrometry, pyrometers measure spectral incandescence at two wavelengths λ_1 and λ_2. The incandescence ratio for these wavelengths is:

$$\frac{J'_{\lambda_1}}{J'_{\lambda_2}} = \frac{C_\lambda\ \varepsilon'_{\lambda_1}(T)\ I'_{b,\lambda_1}(T)}{C_\lambda\ \varepsilon'_{\lambda_2}(T)\ I'_{b,\lambda_2}(T)}$$

$$\frac{J'_{\lambda_1}}{J'_{\lambda_2}} = \frac{\varepsilon'_{\lambda_1}}{\varepsilon'_{\lambda_2}}\frac{\lambda_2^5}{\lambda_1^5}\frac{\exp\left(\frac{C_2}{\lambda_2 T}\right)}{\exp\left(\frac{C_2}{\lambda_1 T}\right)} \tag{2-6}$$

Then, temperature is calculated as

$$T = \frac{C_2(\lambda_2^{-1} - \lambda_1^{-1})}{\ln\left(\frac{J'_{\lambda_1}}{J'_{\lambda_2}}\frac{\lambda_1^5}{\lambda_2^5}\frac{\varepsilon'_{\lambda_2}}{\varepsilon'_{\lambda_1}}\right)} \tag{2-7}$$

The usual hypothesis is that the material is a greybody, meaning that spectral emissivity is constant with wavelength and $\varepsilon'_{\lambda_2}/\varepsilon'_{\lambda_1}$ is taken as unity. The error in the temperature readings can then be expressed by

$$\frac{1}{T_m} - \frac{1}{T_t} = \frac{\ln\left(\frac{\varepsilon'_{\lambda_1}}{\varepsilon'_{\lambda_2}}\right)}{C_2(\lambda_2^{-1} - \lambda_1^{-1})} \tag{2-8}$$

where T_m is the temperature measured with the greybody assumption and T_t is the true temperature of the material. Eq. (2-8) shows that error can be reduced by increasing the difference between λ_1 and λ_2. However, if the material is not a perfect greybody, increasing the gap between the wavelengths causes a bigger difference in spectral emissivity and a larger error. Because of this, dual-wavelength pyrometers use wavelengths as close together as possible, yet different enough such that the spectral bandwidths of the measurements do not superimpose and thereby permit sufficient sensitivity. The interval between λ_1 and λ_2 is typically around 100-200 nm.

Contrary to single-wavelength pyrometry, dual-wavelength pyrometry is, in principle, less sensitive to uncertainties in spectral emissivity and can then be used for materials with unknown spectral emissivity. However, the fact that most materials are not perfect greybodies can lead to greater errors than when utilizing monochromatic pyrometry. A study by Thiessen et al. on TRIP steels showed that, during annealing, the deviation between temperature measured by a thermocouple and by a dual-wavelength pyrometer could reach more than 50 °C [10].

One of the advantages of two-color pyrometry is that it can be employed in an absorbing atmosphere. If λ_1 and λ_2 are near enough to one another, it can be considered that transmittance is the same for both wavelengths. Then, atmospheric absorption is compensated for by calculating the incandescence ratio at λ_1 and λ_2, as shown in Eq. (2-6).

Gold cups can also be employed with DWL pyrometry in order to enhance spectral emissivity and create blackbody conditions. Che and Xie developed a DWL pyrometry system, which uses a gold cup and is called Reflector with a Fast Switching Tube (ReFaST) [4]. The ReFaST pyrometer is equipped with a removable blackened tube which can be inserted in the gold cup in order to cancel out the effect of the cup. Consequently, a system of four equations (two measurements for each wavelength, with and without the tube) can be solved to estimate simultaneously the reflectivity of the gold cup, the true temperature of the material and the material spectral emissivity for both studied wavelengths.

2.1.3 Multi-Wavelength (MWL) Pyrometry

In the case of multi-wavelength pyrometry, incandescence is measured for n wavelengths. Spectral emissivity is then approximated by a mathematical formula using m parameters (a_1, a_2, …, a_m).

Temperature can be calculated by solving a system with n equations and $m+1$ variables (m parameters and temperature), provided that $n \geq m+1$:

$$\begin{cases} J'_{\lambda_1} = f(\lambda_1, a_1, a_2, \dots, a_m, T) \\ J'_{\lambda_2} = f(\lambda_2, a_1, a_2, \dots, a_m, T) \\ \dots \\ J'_{\lambda_n} = f(\lambda_n, a_1, a_2, \dots, a_m, T) \end{cases} \quad (2\text{-}9)$$

The choice of n and m is critical for accurate measurements. Taking $n = m+1$ may cause overfitting between the spectral emissivity model and the measured values, leading to an error in the temperature readings that can diverge for increasing n [11]. A better strategy is to take $n > m+1$, approximate measured spectral emissivity, and fit the model by the least squares method [12].

Two-color pyrometry can be considered as a form of multi-wavelength pyrometry with $n = 2$ and $m = 1$. The mathematical formula used to approximate spectral emissivity is the greybody assumption,

$$\varepsilon'_\lambda(\lambda, T) = a_1(T) \quad (2\text{-}10)$$

with $0 \leq a_1 \leq 1$.

The choice of an appropriate mathematical function to approximate spectral emissivity also participates in reducing the deviation in the temperature calculation: polynomial, exponential, inverse, logarithm, function of wavelength, temperature… Wen showed that temperature errors can be made as low as 0.1% or greater than 20% for temperatures between 700 and 900K depending on what function is used to approximate spectral emissivity [13]. However, Xing et al. proposed an iterative algorithm to estimate the true temperature of a body with multi-wavelength pyrometry, which does not need to assume in advance a model of spectral emissivity and only assumes linear variation of spectral emissivity with temperature [14]. Using the algorithm, deviations between true and measured temperature is less than 1% in the examined cases for a true temperature around 950°C.

Table 2-1 summarizes the advantages and drawbacks of the pyrometry methods. Pyrometry is the temperature measurement method utilized in the continuous galvanizing line, especially during the

intercritical annealing, to ensure appropriate mechanical properties of the steel at the end of the process.

Table 2-1: Summary of pyrometry methods

Pyrometry method	Advantages	Drawbacks
SWL	- Represents the simplest method.	- Requires good knowledge of spectral emissivity.
DWL	- Does not require a good knowledge of spectral emissivity. - Can be used in an absorbing atmosphere.	- Can lead to large errors if the material is not a greybody.
MWL	-Has the potential for the most accurate results.	- Requires knowledge of spectral emissivity as a function of temperature and of wavelength. - Is more complex and expensive.

2.2 Selective Oxidation of AHSS During Intercritical Annealing

Intercritical annealing is part of the continuous galvanizing process and its purpose is to develop the steel to the desired mechanical properties. This heat treatment modifies the microstructure of the base material. The treatment also leads to the formation of oxide on the surface due to the presence of a controlled concentration of oxygen in the furnace. In this section, the principles of intercritical annealing will first be presented, followed by a summary of the growth of selective oxides on the surface of the AHSS. Finally, some methods for controlling steel oxidation within a continuous galvanizing line will be presented.

2.2.1 Intercritical Annealing

Intercritical annealing consists of heating steel to a temperature between Ac_1 and Ac_3 in order to obtain a partially austenitized microstructure, typically around 800 °C. The quantity Ac_1 is the temperature at which ferrite starts transforming into austenite as it evolves towards thermodynamic equilibrium. The quantity Ac_3 is the temperature at which the microstructure becomes fully austenitic. At the end of the cycle, the austenite partially decomposes into ferrite and mostly transforms into martensite due to a pronounced cooling rate. The final microstructure for dual phase

steels after intercritical annealing consists of two phases, a ferrite matrix with martensite islands [15] as illustrated in Figure 2-1.

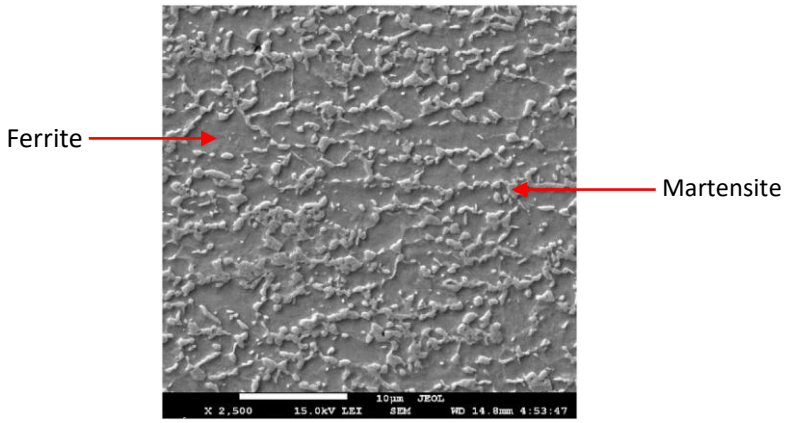

Figure 2-1: Microstructure of DP980 steel after intercritical annealing [16]

Ferrite is a ductile phase with low yield and ultimate tensile strengths. Martensite, conversely, has a low ductility but high mechanical strength. In order to obtain the mechanical properties required by standard ASTM A1079 [17], it is necessary to find a compromise between ductility and mechanical resistance. Consequently, an adequate martensite proportion may exist. Table 2-2 shows example requirements for DP980. One the one hand, annealing at high temperature and holding for a long time will lead to the formation of more austenite and thus more martensite. On the other hand, annealing at a lower temperature will lead to the formation of less austenite and thus less martensite. A compromise must be found to obtain adequate ductility and adequate strength at the end of the cycle.

Table 2-2: Example minimum mechanical properties required by standard ASTM A1079 for DP980

	Elongation (%)	Yield strength (MPa)	Ultimate tensile strength (MPa)
DP980	8	550	980

One of the issues is that insufficient temperature control can induce steel temperature deviations and inappropriate mechanical properties at the end of the process. According to a recent study

performed on DP980 by Mosser et al., a temperature precision of ±50 °C is required in order for mechanical properties to remain within typical required ranges [16].

2.2.2 AHSS Selective Oxidation

Due to the presence of oxygen in the annealing furnace, the steel surfaces are subjected to oxidation during the heat treatment. Oxide often decreases zinc adhesion, increasing the reject rate. Oxidation also affects the sheet spectral emissivity, which is a key parameter for accurate temperature measurements with pyrometry. Furnace atmosphere is therefore controlled in order to limit oxidation.

The quantity of oxygen in the atmosphere is evaluated by measurement of the dew point (DP). The dew point of an atmosphere is the temperature at which air would become saturated with water and at which water vapor would condense into a liquid or solid state [18].

An atmosphere with a higher dew point has a higher oxygen concentration. The partial pressure of oxygen can be determined by calculating the saturation vapor pressure of water as follows [18]:

$$\log p_{\mathrm{sat,H_2O}} = \begin{cases} 9.80\,\dfrac{DP}{273.8+DP} - 2.22 & for\ DP \le 0\ °C \\ 7.58\,\dfrac{DP}{240+DP} - 2.22 & for\ DP > 0\ °C \end{cases} \tag{2-11}$$

where $p_{\mathrm{sat,H_2O}}$ is the saturation vapor pressure of water (atm) and DP is the dew point (°C).

The oxygen pressure is obtained using

$$\frac{1}{2}\log p_{\mathrm{O_2}} = 3.00 - \frac{13088}{T+273.15} + \log\left(\frac{p_{\mathrm{sat,H_2O}}}{p_{\mathrm{H_2}}}\right) \tag{2-12}$$

where p_{O_2} is the partial pressure of oxygen (atm), T is temperature (°C), and $p_{\mathrm{H_2}}$ is the partial pressure of molecular hydrogen (atm). For instance, in annealing conditions typical of galvanizing lines, the atmosphere is composed of 95% N_2 and 5% H_2 by volume with a total pressure of 1 atm and a dew point of -30 °C. For a temperature of 800 °C, this would result in $p_{\mathrm{sat,H_2O}}$ = 3.75×10^{-4} atm and $p_{\mathrm{O_2}}$ = 2.31×10^{-18} Pa.

In these conditions, selective oxidation occurs; thermodynamic conditions favor oxidation of elements most readily oxidized. During annealing, oxidation is thermodynamically favored for the typical main alloying elements of AHSS, which include Mn, Si, Cr and Al. Iron is more stable in its metallic form as illustrated in the Ellingham diagram in Figure 2-2. Figure 2-2 shows the standard Gibbs free reaction energy ΔG^0 in blue as a function of temperature for some oxidation reactions. In order to know whether a metal or its oxide is stable for a given temperature and given oxygen partial pressure p_{O_2}, one needs to calculate Gibbs free reaction energy (ΔG):

$$\Delta G = \Delta G^0 - RT \ln p_{O_2} \quad (2\text{-}13)$$

where R is the ideal gas constant (8.314 J/(mol·K)), T is temperature (K) and p_{O_2} is the partial pressure of oxygen (atm) in the annealing conditions as calculated above.

When $\Delta G < 0$, the oxidation progresses and the reacting element is stable in its oxidized form. When $\Delta G > 0$, the oxidation regresses and the reacting element is stable in its metallic form.

In Figure 2-2, the function $RT \ln p_{O_2}$ is plotted in orange for p_{O_2}=2.31×10^{-18} Pa following the bottom right scale giving partial pressure of oxygen p_{O_2}.

Thus, the annealing conditions described above correspond to the black circle where the temperature is 800 °C. Then, considering the standard free energy ΔG^0 of the reaction 2Fe+O_2⇌2FeO, it can be noticed that $\Delta G^0(T = 800\ °C) > RT \ln p_{O_2}$. Consequently, through Eq. (2-13), $\Delta G > 0$ and Fe is stable in its metallic form in these annealing conditions. In the same way, considering the reaction Si+O_2⇌SiO_2, ΔG^0 is lower than $RT \ln p_{O_2}$ at 800 °C, meaning that $\Delta G > 0$ and Si is stable in its oxidized form in the annealing conditions.

In short, every element for which the standard Gibbs free oxidation reaction energy ΔG^0 (blue line) is lower than $RT \ln p_{O_2}$ (orange line) at 800 °C is stable in its oxidized form. The oxidation reactions corresponding to these elements are indicated with the red circles. In the opposite case, the elements are stable in their metallic forms and the reactions are indicated with green circles. According to Figure 2-2, Fe is stable in its metallic form in the annealing conditions while the main alloying elements like Mn, Si, Cr and Al are stable in oxidized form. It can then be expected to observe manganese, silicon, chromium or aluminium oxide on the surface of the steel but no iron oxide.

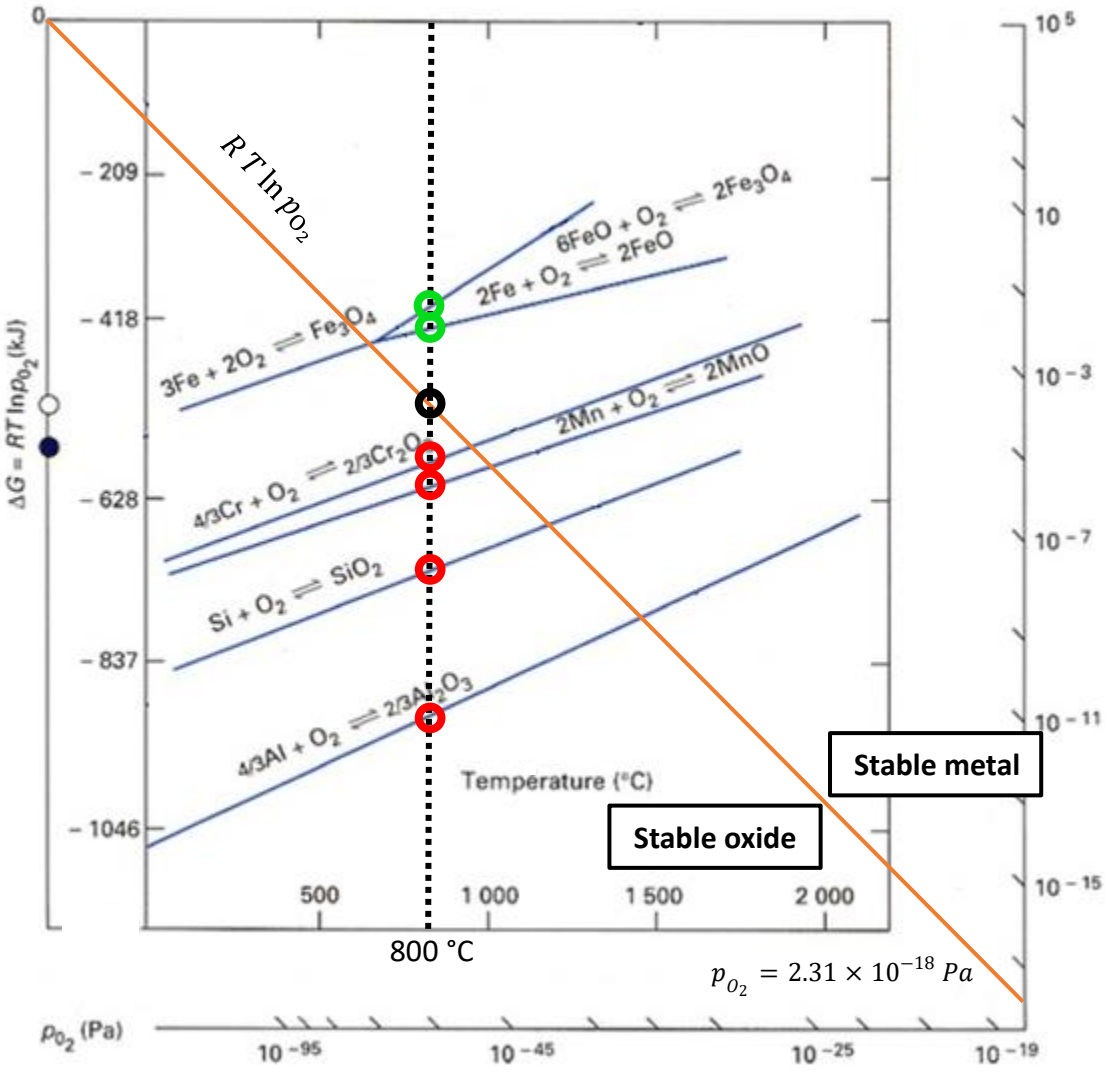

Figure 2-2: Ellingham diagram for several alloying elements of AHSS. Adapted from Buscarlet [19]

Many X-ray photoelectron spectroscopy (XPS) or glow-discharge optical emission spectroscopy (GDOES) measurements have been performed on steel after applying intercritical annealing in order to observe the concentration profiles of the elements on the surface of AHSS [20-23]. These analyses showed an enrichment of the surface in its content of alloying elements including Mn and Si. The analyses also showed a decrease in Fe concentration when compared to the nominal steel chemistry. This diffusion of alloying elements to the surface is accompanied by a decrease in concentration below the surface [24]. Figure 2-3 illustrates these phenomena. Atomic

concentrations of Mn in an as-rolled CMnAl TRIP steel are plotted as a function of sputter time, which is proportional to depth. The Mn concentrations after annealing at several temperatures are also shown. Mn concentration after annealing shows a peak at the surface, then decreases close to the surface before slightly increasing again deeper in the material and stabilizing around the nominal concentration.

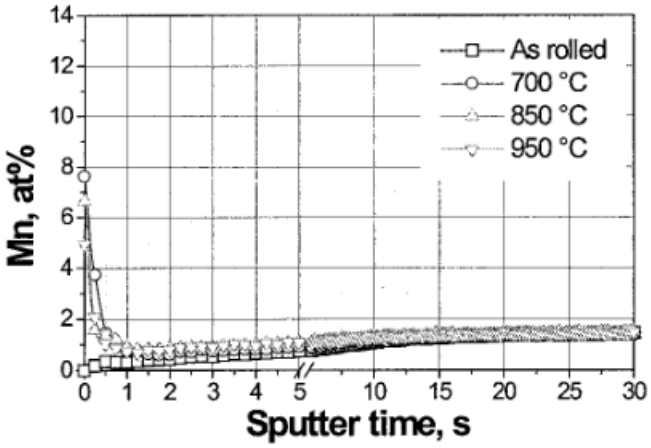

Figure 2-3: GDOES depth profile of Mn in a CMnAl TRIP steel after annealing, for several temperatures [25]

XPS results showed that alloying elements are oxidized on the surface in accordance with the indications in Figure 2-2. Several factors influencing selective oxidation of the steel during intercritical annealing can be identified: steel chemical composition, heating time, and annealing temperature.

Steel chemical composition has an impact on oxidation since some alloying elements are more susceptible to form oxides than others (cf. Figure 2-2). It was shown that most of the oxide on the surface of AHSS is composed of manganese and silicon oxide. Mn and Si, which are typically the main alloying elements of AHSS, can form mono-oxides such as SiO_2 and MnO during intercritical annealing [21, 23, 26-30]. Mn and Si may also form more complex oxides including binary or ternary oxides ($MnSiO_3$, Mn_2SiO_4, Mn_3O_4) [23, 26, 27, 31, 32]. Other alloying elements may also form oxides, such as Al_2O_3, Cr_2O_2, TiO_2, Cu_2O, NiO, and SnO or may bond with Mn and Si to form complex oxides like $MnAl_2O_4$ [33]. The growth of an oxide layer may cause zinc adhesion problems later in the process and lead to an increase in rejection rates because zinc and aluminium from the bath must react with the iron from the steel in order to form an intermetallic inhibition

layer ($Fe_2Al_5Zn_X$) that will guarantee zinc adhesion on the steel. Thus, the presence of a thick oxide film makes surface iron unavailable to zinc and aluminium and disrupts the intermetallic layer formation. Most of the literature studying selective oxidation of steel during annealing investigates the relationship between oxidation and zinc coating adhesion; a thick and compact layer of oxide will lead to poor adhesion of zinc on the surface. The shape of surface oxide has more influence on zinc wetting than on its chemical composition. It was shown in a study by Cho et al. that the presence of Ti, Cu, Ni and Sn could improve the zinc wettability by changing the shape of silicon-rich oxide from a film shape form to vein-shaped (a), elongated (b), or lens-shaped islands (c) [22]. Such islands are illustrated in Figure 2-4. A silicon oxide film will often have more of a negative impact on wettability than manganese oxide, which can be reduced in the zinc bath [34].

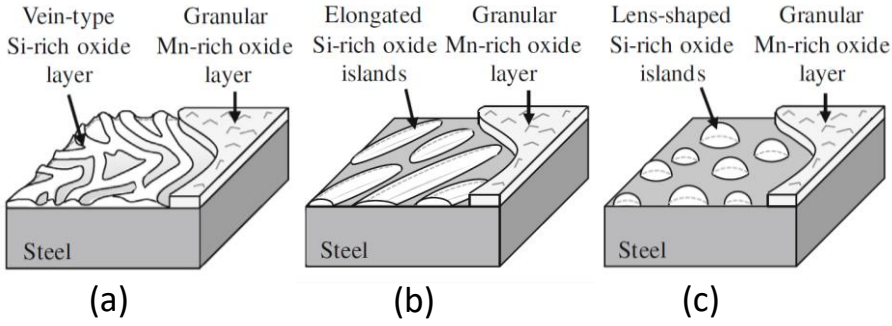

Figure 2-4: Schematic of different oxide morphologies
((a): vein-shaped; (b): elongated; (c): lens-shaped) [22]

However, having a high concentration of Mn compared to Si leads to the formation of a compact and thick layer of manganese-rich oxide. Suzuki et al. determined theoretically that zinc wettability should be good if the mass concentration ratio Mn/Si of the steel is kept greater than 2, so that Mn-Si oxide is formed on the surface instead of SiO_2 for dew points between -25 °C and -10 °C [29]. However, Menguelti et al. showed that, in practice, even if Mn/Si = 2, wettability is not perfect due to the presence of Mn and Si oxides on the surface [35]. Increasing the Mn/Si ratio even more leads to greater oxide surface coverage rates and to the formation of Mn-rich oxides on the whole surface, suppressing zinc adhesion [32]. Like chemical composition of the steel surface, the roughness of the steel surface could have an impact on selective oxidation. Indeed, it was shown that for the same alloy, there was less oxide after annealing on the surface of a polished sample than on an unpolished one [23, 36] because roughness increases the surface area for oxidation and improves oxide nucleation on the surface of the sheet.

Annealing time is another factor influencing oxide growth on AHSS. The choice of annealing time depends on the mechanical properties required for the steel. A longer annealing time will lead to the formation of more austenite and eventually more martensite, giving a higher mechanical strength but a lower ductility to the steel. Increasing annealing time also leads to the formation of thicker oxide on the surface [31, 34], which could have a negative impact on zinc wetting. Simple model of oxidation assume a linear growth of the oxide layer with time [37]. However, the most studied model in the literature is Wagner's model [38], which predicts a parabolic growth of oxide with time. Wagner's main assumptions are as-follows:

- The superficial oxide layer adheres well to the metal surface, is dense and non-porous
- Oxygen in the metal has a limited solubility.
- There are no charge effects at the gas/oxide and oxide/metal interfaces as well as across the oxide.
- Local thermodynamic equilibrium is established at every point in the oxide layer and at the interfaces.

Wagner's model considers a binary alloy. Oxide growth mechanisms are due to the diffusion of metal ions, oxygen ions and electrons in the oxide layer (cf. Figure 2-5) [37]. The model also considers a gradient in oxygen concentration within the oxide layer.

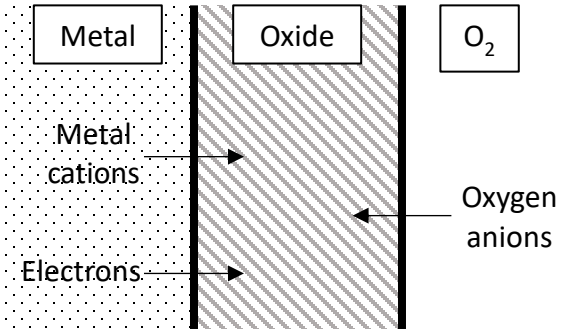

Figure 2-5: Transport mechanisms in a dense oxide layer [37]

Annealing temperature also has an impact on the mechanical properties of steels. Increasing annealing temperature also leads to the formation of more austenite. It was furthermore shown that increasing annealing temperature leads to the formation of more oxide and decreases zinc wettability [35].

2.2.3 Oxidation Control Methods

Oxidation has a negative impact on zinc wettability, and several strategies are employed to limit this reaction. These methods include steel preoxidation, alumino-reduction, and control of the annealing atmosphere.

As explained in a work by Norden et al. [39], preoxidation consists of heating steel, prior to annealing, in a chamber containing enough oxygen to grow iron oxide on the surface. This layer will protect against further oxidation of other alloying elements since they will oxidize under the Fe oxide layer, while the iron oxide will reduce during the annealing because of the low dew point (cf. Figure 2-2). This leads to the presence of more metallic iron on the surface and a better zinc wetting than annealing without preoxidation [39]. However, the iron oxide layer grown during preoxidation can be too thick to be reduced and inhibit zinc adhesion when O_2 concentration is too high [40].

Manganese oxide at the surface can be reduced in the zinc bath through alumino-reduction due to the presence of aluminium in the liquid zinc bath (≈ 0.2 wt.%) [41]. Aluminium reduces manganese and forms oxide following the equation $MnO_{(solid)} + Al_{(solution)} = Mn_{(solution)} + Al_2O_{3(solid)}$. Surface oxide reduction leads to the availability of more metallic Fe for the formation of the intermetallic $Fe_2Al_5Zn_x$ and enables a satisfying zinc coating. However, alumino-reduction may have low impact on wettability due to the formation Al oxide around Mn oxide, preventing the further diffusion of Al in the external oxide layer and reduction of Mn oxide [42].

The most common way to limit the impact of oxidation is to control the annealing atmosphere. For example, increasing the dew point decreases surface oxidation [24, 27, 30, 43]. Figure 2-6 shows the partial pressure of oxygen for several dew points. Oxygen concentration increases with temperature and with dew point. As an example, the oxygen pressure at a temperature of 800 °C is more than 250 times greater with a dew point of 0 °C in comparison with a dew point of -30 °C.

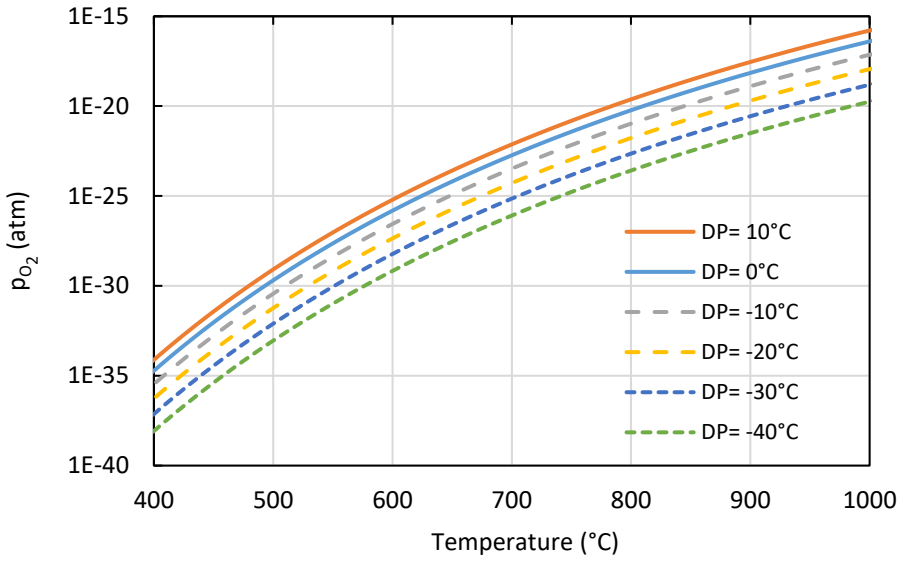

Figure 2-6: Variation of oxygen partial pressure as a function of temperature for several dew points [18]

It may seem counterintuitive at first that increasing the dew point decreases surface oxidation since oxygen concentration in the atmosphere increases. In fact, increasing the DP does not decrease steel oxidation but rather displaces the oxidation from the external surface to underneath the surface. At low dew point, alloying elements diffuse to the surface and oxidize on contact with oxygen. On the other hand, at higher dew point, oxygen pressure is higher, oxygen diffuses in the steel, and alloying elements are oxidized below the surface. Surface oxide is still present after annealing, but its thickness and coverage rate is lower than for a low DP. This decrease in external oxide improves zinc wetting. Figure 2-7 and Figure 2-8 taken from a study by G. Seyed Mousavi et al. [31] present transmission electron microscope (TEM) cross-section micrographs taken from CMnSi AHSS annealed at a temperature of 819 °C for 120 s under two atmospheres with a dew point of -50 °C (Figure 2-7) and -30 °C (Figure 2-8) [31]. Nevertheless, a very low atmospheric dew point also leads to less oxidation due to a lower oxygen partial pressure. Mardethaner et al. showed that there was less oxidation on the surface of DP steels at the end of annealing with a dew point of -58 °C than with a dew point of -30 °C [44]

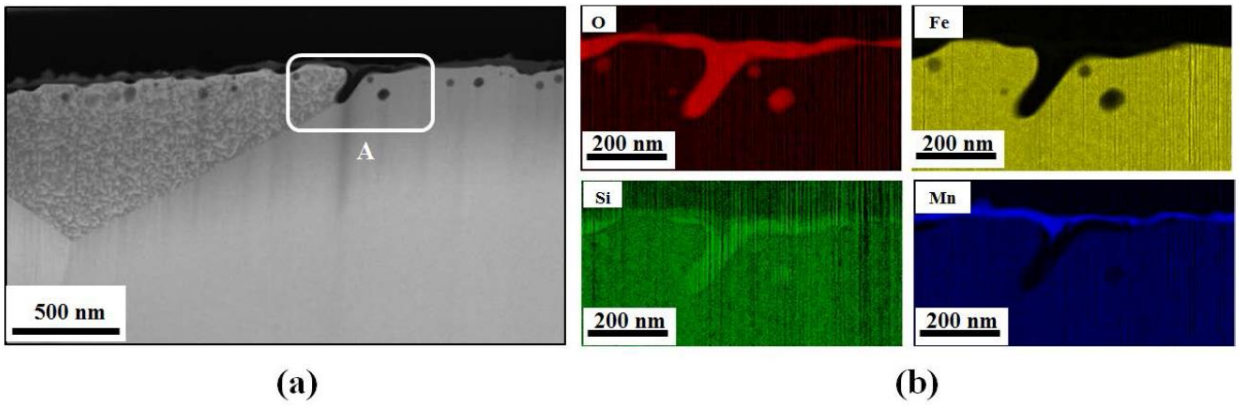

Figure 2-7: TEM micrographs of CMnSi AHSS annealed with a DP of -50 °C ((a): overview of oxides; (b): elemental maps of zone A) [31]

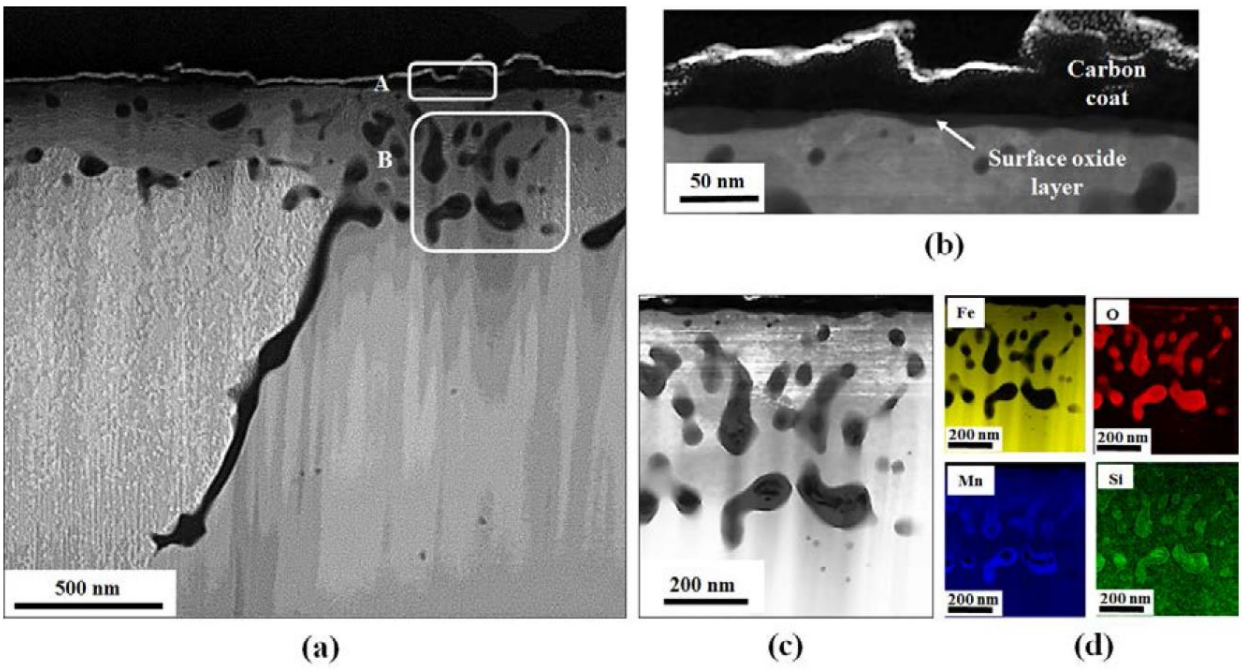

Figure 2-8: TEM micrographs of CMnSi AHSS annealed with a DP of -30 °C ((a): overview of oxides in the cross-section; (b): detailed view of zone A; (c): detailed view of zone B; (d): elemental maps of zone B) [31]

As seen in Figure 2-7, there is oxide on the surface of the steel after annealing. Oxide starts to grow in the base steel along grain boundaries and some internal oxide is already visible in the dark patches in Figure 2-7 (a). The top part of the oxide layer is rich in Mn and the oxide deeper in the material has a higher concentration in Si, as shown in Figure 2-7 (b). After annealing with a dew point of -50 °C, internal oxide grew significantly more than for DP -30 °C, as shown in Figure 2-8 (a); the external oxide is thinner (Figure 2-8 (b)). Internal oxide also grows preferably along grain boundaries and a superficial dendritic oxide network is visible close to the surface (Figure 2-8 (c)). Internal oxide is mainly composed of Si oxide (SiO_2) for the core with a shell of Mn-Si oxide ($MnSiO_3$) around it; the external oxide is once again rich in Mn for this steel. The dew point was then increased to +5 °C in the same study and micrographs showed even more differences as compared with the results for a dew point of -50 °C [31]. Internal oxide forms a dendritic network down to 700 nm on average and down to several microns along grain boundaries. Internal oxide had the same chemical composition for +5 and -30 °C dew points.

In summary, intercritical annealing is necessary to obtain required mechanical properties in steel prior to galvanization. Temperature control during this process is critical owing to the narrow range of acceptable deviations.

Manganese and silicon oxides grow on the surface of the steel during annealing. These oxides can lead to zinc wettability issues later in the process if the oxide layer is too compact and too thick. The composition ratio Mn/Si seems to have an impact on the chemistry and shape of the oxide. When the Mn/Si ratio is too low, Si-rich oxide films will grow. Conversely, when the Mn/Si ratio is very large, a thick, compact layer of Mn-rich oxide is present on the surface. The most common way to control oxidation is to have a high dew point, and thus a high oxygen partial pressure, for the annealing atmosphere. In this way, oxidation is transferred from the surface to below the surface.

The surface changes induced by oxidation can modify the sheet's spectral emissivity, which is the key parameter to obtain accurate temperature readings through pyrometry.

2.3 Emissivity of AHSS

This section discusses the impacts on spectral emissivity of the parameters that are expected to evolve during intercritical annealing as a consequence of heating and oxide growth. These parameters are temperature, the presence and growth of an oxide film, and surface roughness.

2.3.1 Influence of Temperature

Assuming nonpolar radiation Fresnel's equation [45] implies that

$$\rho'_\lambda = \frac{(n-1)^2 + k^2}{(n+1)^2 + k^2} \tag{2-14}$$

where ρ'_λ is the normal spectral reflectivity of the material, and n and k are respectively the refractive index and extinction coefficient of the material. Then, given that $\varepsilon'_\lambda = 1 - \rho'_\lambda$,

$$\varepsilon'_\lambda = \frac{4n}{(n+1)^2 + k^2} \tag{2-15}$$

where ε'_λ is the normal spectral emissivity of the material. n and k can be estimated using the Hagen-Rubens equation:

$$n \approx k \approx \sqrt{\frac{\mu_0\, c_0\, \lambda}{4\pi\, r_e}} \approx \sqrt{\frac{0.003\, \lambda}{r_e}} \tag{2-16}$$

where μ_0 is the magnetic permeability of vacuum ($4\pi\times10^{-7}$ N/A^{-2}), c_0 is the speed of light in vacuum (2.998×10^8 m/s), λ is the wavelength of the radiation (μm) and r_e is the electrical resistivity of the material (Ω·cm). This relation is valid for metals (low resistivity) and for high values of wavelength ($\lambda > 5\ \mu m$). In the infrared range, $\frac{r_e}{\lambda} \ll 1$, and spectral emissivity can be considered proportional to $\left(\frac{r_e}{\lambda}\right)^{1/2}$. Moreover, electrical resistivity increases proportionally to temperature:

$$r_e(T) = r_{e,273}\left(\frac{T}{273}\right) \tag{2-17}$$

where $r_{e,273}$ is the electrical resistivity of the material at a temperature of 273 K and T is temperature (K). The result is that normal spectral emissivity of metals at long wavelengths should theoretically increase proportionally to the square root of temperature:

$$\varepsilon'_{\lambda}(T) \propto \sqrt{T} \tag{2-18}$$

This relation was shown to be valid for liquid metals for temperatures up to 1000K above their melting point [46].

In practice, it is very complex to isolate the influence of temperature on spectral emissivity from the influence of other parameters, such as oxidation state. This is because oxide appears on the surface of steel even with a very low partial pressure of oxygen, as seen in part 2.2.2.

It is possible to isolate the effect of oxydation on spectral emissivity by measuring spectral emissivity at room temperature before and after the treatment. If in-situ measurements are also available, the effect of temperature can be deduced by comparing the spectral emissivity with the values measured in-situ at high temperature. Using this strategy, Del Campo et al. showed that spectral emissivity of certain Ni and Co based aeronautical alloys increases with temperature at long wavelengths [47], in accordance with electromagnetic theory.

2.3.2 Influence of Oxide Films

The growth of oxide on the surface of metals has been shown to increase spectral emissivity [45, 48]. This result is due to the fact that oxide usually has a lower reflectance than the base metal because of its higher resistivity and lower extinction coefficient. Moreover, the growth of iron oxide film modifies the optical path of incident radiation and changes spectral emissivity due to constructive and destructive interferences, as illustrated in Figure 2-9. Optical path is proportional to the oxide thickness d and is modified by reflections between the substrate (in grey) and the surface of the oxide (in purple). Constructive interference are observed when the difference in optical path between the beam reflected by the oxide surface and beam diffracted in the oxide film is a multiple of the radiation wavelength. Destructive interference is observed when dephasing due to the difference in optical path between the reflected and refracted beams is a multiple of the wavelength plus half a wavelength [49]. Therefore, the wavelengths corresponding to spectral

emissivity extrema depends on oxide thickness. This phenomenon of interferences can be observed even for an unpolished base metal surface or when oxide does not fully cover the surface.

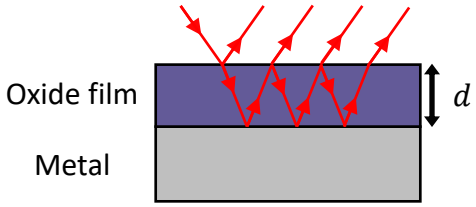

Figure 2-9: Cross-section of a metallic substrate and oxide film [50]

The oscillations can be observed by measuring spectral emissivity directly [50] (as shown in Figure 2-10) or by comparison of material true temperature and temperature readings acquired by pyrometry [51]. Figure 2-10 presents the evolution of the spectral emissivity of Armco iron measured by del Campo et al. at various times during soaking at 480 °C in air [50].

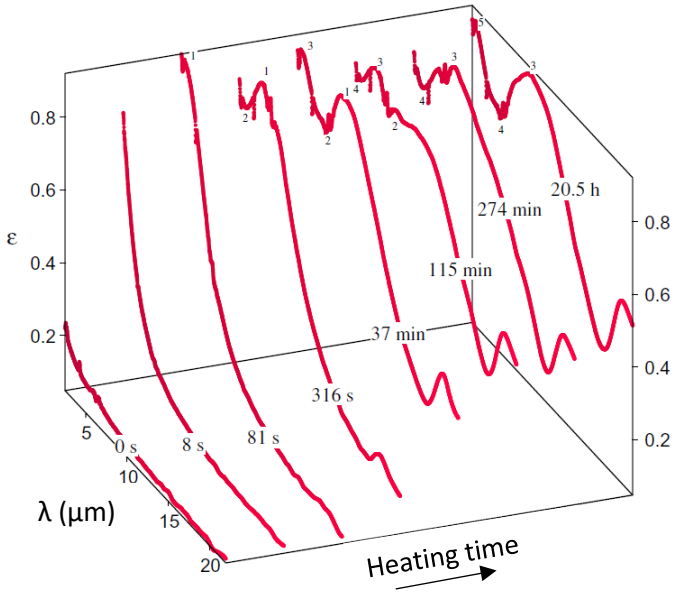

Figure 2-10: Evolution of Armco iron spectral emissivity with time during heating [50]

The spectral emissivity in Figure 2-10 increases from the start of the heating with the thickening of the oxide layer. Oscillations are visible only for 81 s and above. Interference extrema are numbered on the graph and the wavelengths of the peaks increase with time, which is in accordance with an increase in oxide thickness. Interference can be observed until the oxide becomes too thick and all incident radiation that is not reflected by the surface is absorbed [52-54]. Then, spectral emissivity tends to a constant value that is the contribution of the oxide emissivity alone.

Thiessen et al. showed that the growth of oxide during annealing changed the shape of spectral emissivity of AHSS due to temperature deviations observed with dual-wavelength pyrometry [10]. Spectral emissivity is affected by oxidation even when oxide partially covers the surface [10]. The chemical nature of the oxide affects the shape of spectral emissivity [55]. Ham et al. were able to identify aluminium oxide as well as Mn-Si mixed oxides on the surface of a TRIP steel after annealing due to "bumps" in AHSS spectral emissivity at wavelengths corresponding to their vibrational signature around 10, 10.5 and 10.8 μm.

2.3.3 Influence of Roughness

There are few studies relating roughness with spectral emissivity of AHSS. However, numerous studies have shown that roughness has an impact on emissivity for other metals than steel. Increasing roughness leads to an increase in emissivity. The most commonly studied roughness parameters are R_a [56] and R_q [57], which are the arithmetic average and the root mean square (RMS) of a two-dimensional surface profile. The parameters R_a and R_q are measured by a profilometer and are defined as:

$$R_a = \frac{1}{L}\int_0^L |z(x)|\, dx$$
$$R_q = \sqrt{\frac{1}{L}\int_0^L z^2(x)\, dx} \qquad (2\text{-}19)$$

where L is the profile measurement length and z is the height measured by the profilometer. Some early publications by Agababov proposed a formal relationship between total emissivity and R_a through a roughness factor F [58-60]:

$$F = [1 + (1.25\, \pi\, n\, R_a)^2]^{-1} \qquad (2\text{-}20)$$

and

$$\varepsilon_r = \left[1 + \left(\frac{1}{\varepsilon_s} - 1\right) F\right]^{-1} \tag{2-21}$$

where n is the number of intersections of the profile with the profile mean line per unit length; the quantity ε_r is the total emissivity of a "rough" specimen for which the roughness factor is F; finally, ε_s is the emissivity of a smooth specimen of the same material with a roughness factor close to unity. Eqs. (2-20) and (2-21) are only valid for diffuse greybodies. The roughness factor F does not take into account interactions between roughness and wavelength, nor does it account for the influence of roughness on spectral emissivity at different scales. For these reasons, roughness is now studied in terms of optical roughness (R_q/λ), which is defined as the ratio between the RMS roughness R_q and light wavelength λ.

Several regimes can be identified, depending on the value of optical roughness, as proposed by Wen and Mudawar [57]. In the geometric region ($R_q/\lambda > 1$), geometric optics can be applied. Typical surface cavities are greater than incident light wavelength. These cavities behave like local blackbodies due to the multiple reflections and absorptions of incident light by the surface. In the intermediate region ($0.2 < R_q/\lambda < 1$), directional spectral emissivity can be modeled as a combination of a purely specular model and of a purely diffuse model. Increasing roughness makes the surface more diffuse and increases spectral emissivity. In the specular region ($0 < R_q/\lambda < 0.2$), the surface is considered as optically smooth and the reflection is specular. Spectral directional emissivity decreases with wavelength according to an exponential decay function of optical roughness R_q/λ.

According by the model by Wen and Mudawar, roughness has greatest effects on spectral emissivity in the geometric and intermediate region. Nevertheless, Ham et al. showed that small scale roughness evolution due to oxide growth was correlated with emissivity evolution in the long wavelength infrared [61]. Moreover, Yu et al. showed that optical roughness is insufficient to fully describe the effect of roughness on spectral emissivity [62]. Other roughness parameters may be studied, such as skewness R_{sk} and kurtosis R_{ku}. Those parameters are the third and fourth moments of RMS roughness:

$$R_{sk} = \frac{1}{L\,R_q^3}\int_0^L z^3(x)\,dx$$
$$R_{ku} = \frac{1}{L\,R_q^4}\int_0^L z^4(x)\,dx \qquad (2\text{-}22)$$

While R_a and R_q characterize profile height, R_{sk} and R_{ku} describe the profile shape [63], as illustrated in Figure 2-11. Skewness describes height distribution above and below the mean line. When $R_{sk} < 0$, the surface topography may include deep valleys. Conversely, peaks may be pronounced when $R_{sk} > 0$. Kurtosis describes how height distribution is concentrated around the mean line. When $R_{ku} > 3$, a surface should present a "sharp" topography, while a surface should look "smoother" for $R_{ku} < 3$. A value of R_{ku} equal to 3 corresponds to a Gaussian distribution of the profile height around the mean line.

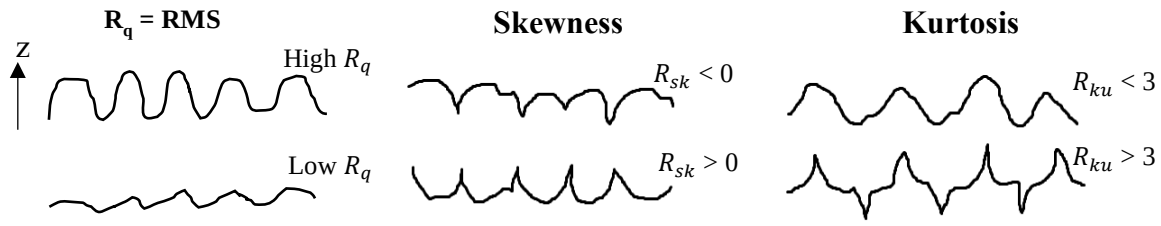

Figure 2-11: Schematic illustrations of profiles with various R_q, skewness and kurtosis [63, 64]

Regarding AHSS, a recent article by Ham et al. showed a correlation between surface roughness measured with white light interferometry and the emissivity of a TRIP steel [61]. As shown in Figure 2-12, a greater roughness is accompanied with a greater emissivity. Figure 2-12 shows global emissivity $\varepsilon_{\overline{\lambda}}$ and roughness for samples annealed at different dew points and for different times.

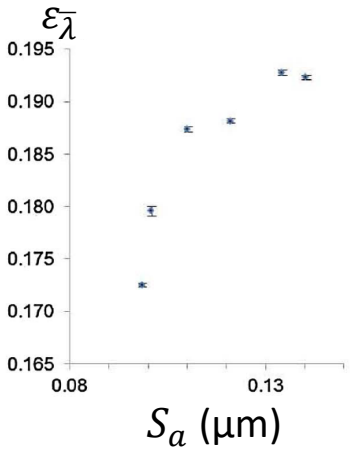

Figure 2-12: Correlation of local scale roughness and global emissivity [61]

Global emissivity is the equivalent emissivity of a greybody which would emit the same energy as the steel in the long-wavelength infrared (8 to 12 µm). The roughness parameter presented is S_a, which is the arithmetic average of a three-dimensional surface measuring around 700 × 500 mm. S_a was calculated after filtering the low frequency topography patterns in order to isolate the patterns induced by oxide formation.

In summary, surface roughness has an impact on spectral emissivity, not only when valleys are in the same range or higher than wavelength ($R_q/\lambda > 0.2$) [61]. Increasing roughness increases spectral emissivity. However, there is no simple parameter or model that enables exhaustive characterization of the influence of roughness on spectral emissivity.

The growth of oxide also increases spectral emissivity. During this process, spectral oscillations may be observed due to light interference, but such oscillations vanish in the presence of sufficiently thick oxide.

2.4 Synthesis

Review of the literature has shown that selective oxidation occurs on the steel during intercritical annealing. The formation of oxide modifies surface chemistry and can also modify surface roughness because of the nodular shapes of the oxide islands, for instance. Surface chemistry and surface roughness, as well as the increase in temperature during heating, are known to have an impact on material spectral emissivity. Nevertheless, since the industrial process is continuous,

temperature measurement is performed by pyrometry and the variations in spectral emissivity induce temperature deviations during annealing. The temperature deviations eventually lead to rejected material when the mechanical properties of the steel may not meet requirements.

Most of the literature studying selective oxidation only focuses on the impact of oxide on reactive zinc wetting during galvanization. Moreover, the literature studying the impact of oxide on spectral emissivity focuses on iron oxide. Few articles focus on the impact of selective oxidation on spectral emissivity of AHSS [10, 55, 61]. To the best of the author's knowledge, no published work focuses on spectral emissivity in the near infrared.

The present work tackles the following research question:

How does selective oxidation during intercritical annealing of dual phase steels affect temperature measurements acquired by pyrometry?

The research hypothesis is that selective oxidation affects the sheet spectral emissivity. The evolution of spectral emissivity would then induce errors in the temperature measurements with pyrometry.

This research question can be divided into the following specific objectives:

1) How does near-normal spectral emissivity of dual phase steel evolve during intercritical annealing?
2) How does surface oxidation evolve during annealing?
3) What is the relationship between oxidation state and spectral emissivity?
4) What is the impact of spectral emissivity variation on temperature measurement?

The next chapter presents the experimental protocol and the different measurements that were executed in order to tackle the research question.

CHAPTER 3 EXPERIMENTAL METHODOLOGY

This chapter details the experimental design and includes the results of a survey conducted among six GAP industrial partners in order to acquire insight into industrial application of pyrometry.

Then, in order to address the research questions formulated in Chapter 2, the objectives of the present work are as follows:

- Quantify spectral emissivity evolution at several points during intercritical annealing;
- Observe and compare oxidation states and surface modifications at the same points; and
- Find a possible link between surface modifications and changes in spectral emissivity to eventually predict spectral emissivity evolution.

In order to achieve the first objective, annealing cycles were applied to the steels. The cycles were interrupted at several points in order to obtain specimens corresponding to various stages of the CGL intercritical annealing process. The near-normal spectral emissivity of the steel was then measured for these conditions.

The oxide characterization methods used to meet the second objective are detailed further in this chapter. The methods include: glow discharge optical emission spectroscopy (GDOES) analyses, scanning electron microscopy (SEM) observations, and roughness measurements.

This chapter finally concludes with an explanation of the strategy chosen to present the results derived from the experiments, as part of a paper based thesis.

3.1 Results of the Industrial Survey

The objective of the survey was to acquire better knowledge of industrial pyrometry practices, with respect to, for instance, the methods used and the range of wavelengths employed, in order to respond more appropriately to topical challenges. The survey was conducted during the summer of 2014 among six galvanizing companies that use continuous galvanizing lines.

These companies responded to the questionnaire presented in Appendix B. The results of the survey are presented in Appendix C and are summarized in Table 3-1.

Table 3-1: Summary of the survey results

Question	Result
Type of sensor	Single-wavelength (100%)
Wavelength range	1.0-3.0 µm
Expected temperature deviations	5-40 °C
Use of wedge configuration	Yes (67%), No (33%)
Wedge aiming method	Manual, visual (100%)
Pre-oxidation	Yes (60%), No (40%)
Emissivity adjustment	No (100%)

The survey indicates that all the companies polled use single-wavelength pyrometry. However, beside the survey, many companies also reported using dual-wavelength pyrometry. The wavelengths used for pyrometry range from 1 to 3 µm. The same industrial partners expect temperature errors of up to 40 °C between the true sheet temperature and the temperature measured by pyrometry. Two thirds of the companies polled make use of the wedge effect for pyrometry. Nevertheless, pyrometer wedge aiming is performed manually with visual help systems; manual aiming incurs issues due to the lack of precision. Aiming is sometimes even performed when the galvanizing line is cold, thus not taking into account thermal expansion of the rolls when the line is operated at high temperature. The survey also indicated that 60% of the responding companies indicated that they were using a pre-oxidizing step in the CGL. Finally, it appears that steel spectral emissivity estimates are not adjusted during the process from one material to another for all the surveyed companies, which could be another source of temperature reading errors. Moreover, the change in spectral emissivity during pre-oxidation and iron reduction during annealing can induce temperature deviations and is not taken into account for temperature control.

The experimental plan was designed based on the result of this survey. It was decided to measure spectral emissivity for wavelengths covering the range from 1 to 3 µm and to focus on temperature deviations during annealing that can be induced by spectral emissivity modifications for single-wavelength pyrometry. Moreover, surface alterations were characterized in terms of chemical composition with glow-discharge optical emission spectroscopy (GDOES) and in terms of

topography with scanning electron microscopy (SEM), profilomtery, white light interferometry (WLI) and atomic force microscopy (AFM).

3.2 Sample Procurement

The materials studied in the present work are two grades of cold rolled dual-phase steel: DP780 and DP980. The grades of these steels indicate their minimum ultimate tensile strengths in MPa [17]. These materials were chosen for this study because of their high mechanical strength and because they are becoming widely used in the industrial continuous galvanizing lines. The steels were provided in the shape of 1.6 mm thick sheets for DP780 and 1.3 mm thick sheets for DP980.

The chemical compositions of the steels is proprietary and cannot be disclosed. However, the composition were measured by spark atomic emission spectroscopy in compliance with standard ASTM E415-14 [65]. The compositions meet the requirements of the ASTM A1079 standard [17] shown in Table 3-2. The values listed are the maximum acceptable percent elemental concentrations for both DP780 and DP980.

Table 3-2: Maximum acceptable compositions of DP780 and DP980 according to the ASTM A1079 standard [17] (maximum weight percent)

	C	**Mn+Al+Si**	**P**	**S**	**Cu**	**Ni**	**Cr+Mo**	**V+Nb+Ti**
DP780	0.18	5.40	0.080	0.015	0.20	0.50	1.40	0.35
DP980	0.23	6.00	0.080	0.015	0.20	0.50	1.40	0.35

Nevertheless, the chemical Mn/Si ratio of DP780 and DP980 is reported in Table 3-3.

Table 3-3: Chemical Mn/Si ratio of DP780 and DP980

Mn/Si	**% mass**	**% atomic**
DP780	11.3	5.8
DP980	4.3	2.2

Intercritical annealing was applied to the materials on coupons in the McMaster Galvanizing Simulator (MGS) at the McMaster University Automotive Resource Centre. This simulator was

manufactured by Iwatani-Surtec [66]. The atmosphere in the annealing chamber was controlled and composed of 95% N_2 and 5% H_2 by volume. Annealing cycles were performed at two dew points: -30 °C and 0 °C. -30 °C is the typical dew point in the industrial galvanizing lines. A dew point of 0°C was used to study the effect of dew point on the steels. A value of 0°C was shown to induce internal oxidation on AHSS [43]. Figure 3-1 presents the annealing cycles that were applied to the steels, with blue triangle for DP780 and red circles for DP980. The cycles were suggested by the industrial partners and are representative of the ones used in the industrial continuous galvanizing lines for these specific steel grades. The cycles consist of heating the material, then soaking the material, and finally fast cooling the material down to a temperature close to the temperature of the liquid zinc (460 °C). The cycle for DP780 is twice as long as for DP980. In order to be able to compare the materials sensitivities to intercritical annealing, a longer cycle was applied to DP980 (dashed line). This cycle is not representative of the galvanizing lines. The purpose of this cycle is to investigate sensitivity to the annealing cycle without the influence of heating time. The spectral emissivity and oxidation evolution during annealing was studied at multiple points during a heat treatment cycle denoted “A”, “B”, “Full” and “Long”. To do so, the heat treatment cycles were interrupted and the samples rapidly cooled down to room temperature with N_2 gas at a rate between 20 and 40 °C/s and sometimes up to 100 °C/s. The temperatures and times corresponding with these interruption points are listed in Table 3-4. After cooling, the samples were stored in a desiccator in order to maintain the samples oxidation state.

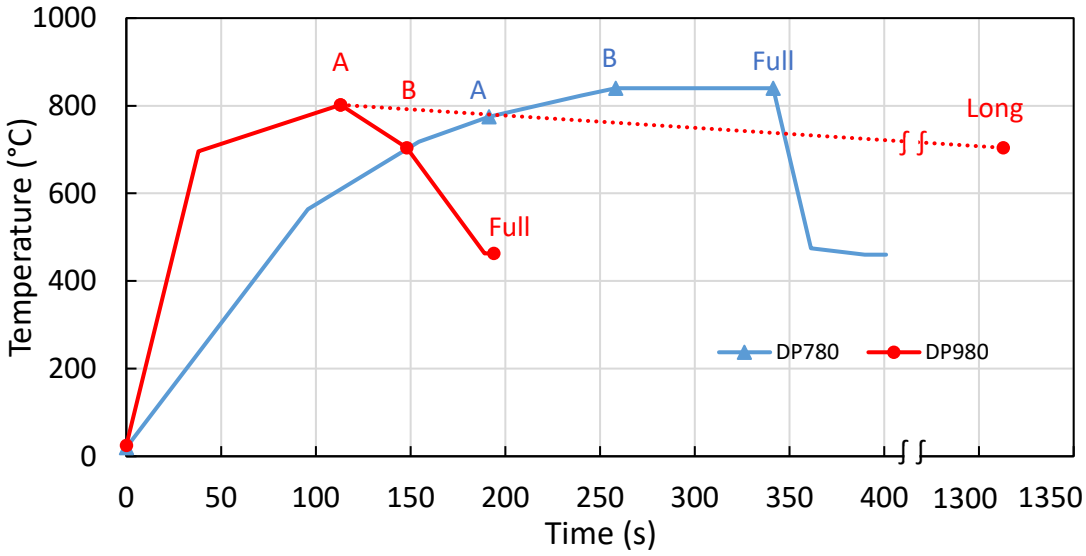

Figure 3-1: Intercritical annealing cycles applied to the steels

Table 3-4: Times and temperatures at which the cycles were interrupted

		A	B	Full	Long
DP780	*t* (s)	191	258	341	N.A.
	T (°C)	775	840	840	N.A.
DP980	*t* (s)	113	148	194	1313
	T (°C)	802	704	463	704

The steel was cleaned with isopropanol prior to annealing. The steel temperature in the simulator was measured using a thermocouple welded to the top half of the coupons and heating was performed using quartz lamps. Figure 3-2 presents a schematic of the coupons that were annealed in the simulator at McMaster University. The size of the coupons was 200 × 120 mm. The samples used for emissivity measurements and the other analyses were cut preferentially in the bottom part of the coupon in the grey area denoted (1) in Figure 3-2.

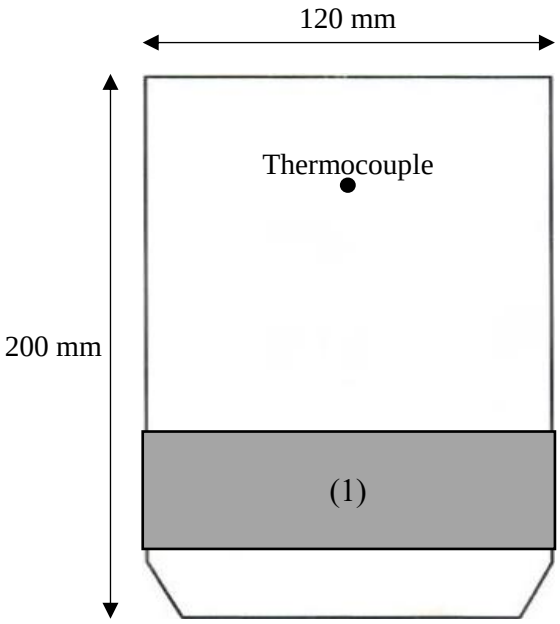

Figure 3-2: Schematic of a coupon that was processed in the simulator

3.3 Measurements

The measurements performed during this project were spectral emissivity measurements and evaluations of surface evolution during intercritical annealing. All measurements were performed at room temperature except for one exploration experiment within a Gleeble chamber.

3.3.1 Spectral Emissivity

3.3.1.1 Room Temperature Measurements

There is no window in the heating part of the galvanizing simulator through which in-situ pyrometric measurements could have been performed. Therefore, for this project, spectral emissivity was measured ex-situ at room temperature. The choice of measuring at room temperature is based on the hypothesis that oxidation will not significantly evolve after quenching. In other words, it is considered that the oxide formed at high temperature in the simulator remains stable. However, it does not take into account the possible evolution of spectral emissivity with temperature.

Two instruments were used for the measurements: a Perkin Elmer Lambda 1050 spectrophotometer and a Surface Optics SOC-100 Fourier-transform infrared (FTIR) reflectometer, both in the Laboratoire des Revêtements Fonctionnels et Ingénierie de Surface (LaRFIS) of Polytechnique Montréal. Specimens were cleaned with isopropanol prior to measurements.

The Lambda 1050 measures directional hemispherical spectral reflectivity ($\rho'_{\lambda-d/h}$) while the SOC-100 measures hemispherical directional spectral reflectivity ($\rho'_{\lambda-h/d}$). Spectral near-normal emissivity can be calculated from one or the other measurement using Eq. (3-1):

$$\varepsilon'_{\lambda} = 1 - \rho'_{\lambda-d/h} = 1 - \rho'_{\lambda-h/d} \tag{3-1}$$

The wavelengths considered by the devices have complementary ranges. The Lambda 1050 measures spectral reflectivity partly in the visible spectrum and in the near infrared spectrum (0.6 to 2.5 µm) and the SOC-100 in the more distant infrared for (2.5 to 25 µm). The use of both instruments enables study of the entire wavelength range that the industrial partners reported using (1-3 µm) in the survey.

The Lambda 1050 uses a monochromatic incident beam which reflects off the sample and is diffused in an integrating sphere. The wall of the sphere is covered with Spectralon, which is a highly reflective and diffuse material. A detector located in the bottom of the sphere measures reflected intensity. Reflectivity is only measured in the incidence direction of the monochromatic

beam on the sample. Reflectivity is determined by comparing the intensity reflected by the specimen with the intensity reflected when the sample is replaced by Spectralon, by simple ratio:

$$\rho'_{\lambda-d/h,meas} = \frac{I_{\lambda,r}}{I_{\lambda,r,\mathrm{Spect}}} \tag{3-2}$$

where $\rho'_{\lambda-d/h,meas}$ is the measured directional hemispherical reflectivity, $I_{\lambda,r}$ is the intensity reflected by the sample and $I_{\lambda,r,\mathrm{Spect}}$ is the intensity reflected by Spectralon. The latter is measured during the calibration of the instrument. Nevertheless, Spectralon is not a perfect reflector ($\rho'_\lambda = 1$), as illustrated in Figure 3-3.

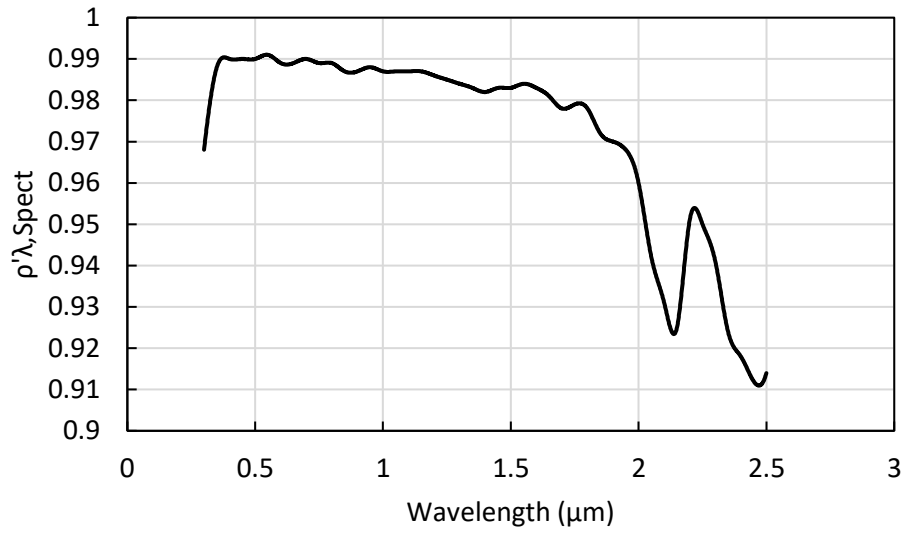

Figure 3-3: Spectral reflectivity of Spectralon

Figure 3-3 presents the Spectralon reflectivity for wavelengths between 0.3 and 2.5 µm. Reflectivity differs from unity in the presented range of wavelengths, especially at long wavelengths. Therefore, reflectivity values measured by the Lambda 1050 were corrected in order to obtain the true sample reflectivity using the following equation:

$$\rho'_{\lambda-d/h,true} = \rho'_{\lambda-d/h,meas} \times \rho'_{\lambda,\mathrm{Spect}} \tag{3-3}$$

where $\rho'_{\lambda-d/h,true}$ is the true sample directional hemispherical reflectivity and $\rho'_{\lambda,\mathrm{Spect}}$ is the Spectralon directional reflectivity.

In the case of the SOC-100, a specular gold ellipsoidal mirror reflects all radiation emanating from a black body simulant source located at one focal point of the mirror. The radiation is reflected uniformly in power for all directions on a sample located at the other focal point of the mirror. Radiation reflected by the sample in one direction is transferred to a FTIR interferometer via a plane reflector. The direction in which reflectivity is measured depends on the position of the collector. Similar to the Lambda 1050, reflectivity is determined by comparing the intensity reflected by the specimen with the intensity reflected by the reference material (specular gold) using the following equation:

$$\rho'_{\lambda-h/d,meas} = \frac{I'_{\lambda,r}}{I'_{\lambda,r,\text{gold}}} \tag{3-4}$$

where $\rho'_{\lambda-h/d,meas}$ is the measured hemispherical directional reflectivity, $I'_{\lambda,r}$ is the intensity reflected by the sample, and $I'_{\lambda,r,\text{gold}}$ is the intensity reflected by the gold reference. In the same manner as Spectralon, specular gold is not a perfect reflector and the instrument software automatically adjusts the measured spectra using specular gold reference reflectance values.

Thermal radiation emitted by the samples at room temperature is negligible in the wavelength range of the Lambda 1050. However, the SOC-100 performs a background measurement with the "blackbody" source occluded so as to correct for background radiation, isolating the radiation from the sample. Measurement uncertainties are in the range of 1-3 %. The main sources of errors for the Lambda 1050 are the accuracy of the photometric sensors and the fact the integrating sphere coating is not perfectly diffuse. In the case of the SOC-100, the main sources of error are the accuracy of the sensors and the calibration with specular gold.

Table 3-5 presents the characteristics of both instruments.

Table 3-5: Characteristics of the emissivity measurements instruments

Instrument	Lambda 1050	SOC-100
Measured quantity	Directional-hemispherical reflectivity ($\rho'_{\lambda-d/h}$)	Hemispherical-directional reflectivity ($\rho'_{\lambda-h/d}$)
Wavelength range (µm)	0.6-2.5	2.5-25
Measurement angle	8°	7°-80°
Sample size	Min. 25 × 25 mm	Max. 25 × 25 mm
Spot size	10 x 7 mm	Ø7 mm

Since pyrometers are typically oriented normally to the steel surface, spectral reflectivity was measured near-normal to the surface in order to obtain near-normal spectral emissivity. However, it is not possible to measure normal reflectivity with the instruments: the only incident angle for the Lambda 1050 is 8° from normal and the lowest collection angle is 7° from normal for the SOC-100. Radiative properties have little dependence to direction at low incident angle [67]. So it will be assumed that near-normal reflectivity measured by the Lambda 1050 and the SOC-100 equals normal reflectivity.

Samples were cut from the annealed coupons with a manual ribbon saw without lubrication. The samples were cut to the dimensions 25 × 25 mm so that they could be used with both measurement instruments. Eight spectral emissivity measurements were performed per condition and per instrument. Two measurements were performed per sample face on two specimens per condition. The samples were rotated by 90° between each measurement so that possible effects of the sample orientation on near-normal spectral emissivity were compensated for. Table 3-6 presents the number of near-normal spectral emissivity measurements performed at room temperature with each instrument overall and for each condition.

Table 3-6: Matrix of room temperature spectral emissivity measurements

		Lambda 1050	SOC 100
DP780	AR	8	8
	A	8	8
	B	8	8
	Full DP -30 °C	8	8
	Full DP 0 °C	8	8
DP980	AR	8	8
	A	8	8
	B	8	8
	Full DP -30 °C	8	8
	Full DP 0 °C	8	8
	Long	8	8
Total		**88**	**88**

3.3.1.2 High Temperature Measurements

Spectral emissivity was also measured at high temperature to better approximate actual annealing conditions. Samples of raw material were heated by resistive heating with an electric current in a Gleeble 3500 at the University of Waterloo, following the same cycle as for DP980 in Figure 3-1. Argon with a purity of 99.999% by volume was used for the atmosphere in the heating chamber. The Gleeble was equipped with an O_2 pressure sensor. However, the sensor was not calibrated when the measurements were performed; heating was initiated when the value indicated by the sensor stabilized after an argon purge effected in order to minimize the quantity of oxygen in the chamber. Nevertheless, oxygen partial pressure in the Gleeble could be much greater than the one in the galvanizing simulator because of oxygen in the argon bottle (up to 2 ppm) and the oxygen trapped in the chamber during the purge.

The size of the samples used in the Gleeble was around 150 × 40 mm. Temperature measurements was were acquired using a thermocouple welded to the center of a face of the sample.

The intensity of radiation emitted by the sample was measured with a NIRQuest 512 spectrometer. The instrument was calibrated with a blackbody source (Model 463 from Infrared Industries). Spectral emissivity was estimated by calculating the ratio of the intensity radiated by the sample to the intensity radiated by the blackbody reference at the same temperature, (cf. Eq. (A-6)). The

radiation sensor pointed at the center of the sample, normally to sample's surface, at the face opposite to the thermocouple. It was assumed that the measured reflectivity was representative of the region sampled by the thermocouple.

3.3.2 Surface Alterations

Surface modifications during annealing were evaluated in terms of chemical composition and in terms of topography evolution.

3.3.2.1 Chemical Analyses

Chemical analyses of the surface were effected by glow-discharge optical emission spectroscopy (GDOES) and X-ray photoelectron spectroscopy (XPS). Both methods are destructive sputtering methods.

In the case of GDOES, the sample is used as an electrode to create an argon plasma on its surface. Argon ions hit the sample surface and sputter the material layer by layer. Atoms of the sample are projected into the plasma and are electronically excited. When the atoms de-excite, they emit photons the wavelengths of which are characteristic of the excited atoms.

In this study, GDOES was used on steel to analyse the composition and thickness of the oxide layer down to 500 nm with a vertical resolution of about 5 nm. Table 3-7 shows GDOES operating parameters used for this study.

Table 3-7: GDOES operating parameters

Model	GD Profiler HR (Horiba)
Ionized gas	Argon
Power	40 W
Excitation mode	Radiofrequency (RF)
Anode diameter	4 mm
Pressure	600 Pa
Average measurement time	0.1 s/point

In the case of XPS, the sample is irradiated by a monochromatic X-ray source. Surface atoms are then ionized and photoelectrons can be emitted by the surface. The energies of these photoelectrons are characteristic of the ionized elements and of their oxidation states. XPS can then differentiate chemical compounds.

XPS by itself does not sputter the surface. However, it is often combined with an ion gun able to sputter the surface so that elemental profiles can be measured.

Table 3-8 lists the XPS operating parameters.

Table 3-8: XPS operating parameters

Model	**VG ESCALAB 3 MKII**
X-ray source	Al Kα
Power	300 W (15 kV, 20 mA)
Analysed area	2 mm × 3 mm
Analysed depth	< 10 nm
Ion gun	Ar +
Sputtering rate (estimation)	3.3 nm/min

The main advantage of GDOES is that measurements are very quick. When evaluating elemental profiles, it is possible to perform many measurements in a relatively short amount of time and to obtain depth resolution better than 5 nm. Measurements for XPS take longer than measurements with GDOES do. However, XPS reveals chemical structure, whereas GDOES reveals only atomic composition.

Table 3-9 presents the number of elemental analyses overall and for each condition.

Table 3-9: Matrix of chemical analyses

		GDOES	XPS
DP780	AR	2	
	A	2	1
	B	2	
	Full DP -30 °C	2	1
	Full DP 0 °C	2	
DP980	AR	2	1
	A	2	1
	B	2	
	Full DP -30 °C	2	2
	Full DP 0 °C	2	1
	Long	2	
Total		**22**	**7**

3.3.2.2 Topography Evolution

Steel surface topography evolution was evaluated with different methods at several stages during annealing described in Figure 3-1: scanning electron microscopy (SEM), profilometry, white light interferometry (WLI) and atomic force microscopy (AFM).

The SEM used for this study is a JEOL JSM7600F equipped with a field emission gun. Acceleration voltage was limited to 3 keV in order to have a small interaction volume, given the thinness of the oxide layer and the smallness of the oxide nodules.

SEM can be used to observe surface topography qualitatively with secondary electrons and evaluate surface composition with backscattered electrons.

When performing a SEM micrograph with secondary electrons, contrast is a function of topography and it is possible to observe changes in surface roughness, growth of oxide nodules, and topography smoothing.

The detection of backscattered electrons at a given point of the surface in a SEM micrograph is a function mostly of the chemical composition of the studied area. With backscattered electron micrographs, contrast is a function of the atomic number and it is possible to observe changes in the surface composition or growth of oxide particles.

A cross-section of a sample of galvannealed (annealed, then galvanized) DP980 was obtained using a focused ion beam (FIB), in order to observe possible internal oxidation. It consisted of sputtering the surface using a beam of ions until a cross-section was visible by SEM.

In order to monitor and quantify the surface evolutions observed with the SEM, a profilometer was used to measure surface roughness. Results for parameters R_q, R_{sk} and R_{ku} are presented in this study. These parameters are defined in Eq. (2-19) and (2-22). The profilometer used in this study was a Surftest SJ-210 with a tip radius of 4 µm. Measurements were performed with a cutoff length of 0.8 mm, with five sampling lengths per measurement and a measurement speed of 0.5 mm/s, following the ISO 4287:1997 standard [68]. Roughness evaluations were performed similarly to room temperature spectral emissivity measurements; eight measurements were performed for each condition: two measurements of both face of two samples with a sample rotation of 90° between each reading. Due to the large tip radius of the instrument, it was impossible to detect small surface details such as oxide islands. It was then decided to investigate additional topography analysis methods.

Roughness measurements were then performed by white light interferometry (WLI). The advantages of this technique are the good measurement speed the possibility to build surface topography maps. However, the technique was also dismissed due to insufficient spatial resolution and the decision was taken to start using atomic force microscopy (AFM).

An atomic force microscope uses a cantilever in contact with the sample surface. The tip of the cantilever rises and falls following surface topography. An inclined laser points at the top of the cantilever and is reflected into a photodiode with four quadrants. The movement of the cantilever due to sample topography deflects the reflected beam. It is then possible to determine surface height by analyzing the position of the light beam on the diode. In the end, a map of the surface can be built by rastering. AFM measurements have excellent precision but are time consuming, especially when scanning a large area.

AFM images were acquired in air at room temperature on a Bruker Dimension ICON. Intermittent contact imaging (i.e., “tapping mode”) was performed at a scan rate of 1 Hz using etched silicon cantilevers (ACTA from AppNano Inc.) with a resonance frequency of about 300 kHz, a spring constant of about 42 N/m, and tip radius below 10 nm. All Images were acquired with a medium setting for tip oscillation damping (20-30% damping).

Table 3-10 presents the number of roughness measurements performed with the profilometer overall and for each condition, as well as the conditions for which WLI and AFM analyses were performed (identified with "x").

Table 3-10: Matrix of topography analysis

		Profilometer	**WLI**	**AFM**
DP780	AR	8	x	X
	A	8		
	B	8		
	Full DP -30 °C	8	x	X
	Full DP 0 °C	8		
DP980	AR	8	x	
	A	8	x	
	B	8		
	Full DP -30 °C	8	x	
	Full DP 0 °C	8		
	Long	8	x	
Total		**88**		

Table 3-11 presents a summary of the methods used in this research project and the measured properties.

Table 3-11: Summary of the measurements presented in the thesis

Measurement	**Instrument or method**	**Details**
Near-normal spectral emissivity	Lambda 1050	Room temperature $0.6\ \mu m < \lambda < 2.5\ \mu m$
	SOC-100	Room temperature $2.5\ \mu m < \lambda < 25\ \mu m$
	Gleeble	High temperature $2.5\ \mu m < \lambda < 25\ \mu m$
Chemical analysis	GDOES	Elemental profiles
	XPS	Elemental profiles and compound identification
Topography investigations	SEM	Oxide morphology
	AFM	Oxide morphology, roughness
	Profilometry	Roughness
	WLI	Oxide morphology, roughness

3.4 Results Presentation Organization

The spectral emissivity and surface evolution main results were presented in the conference peer reviewed paper entitled “Effect of oxidation on emissivity for DP780 and DP980 steels” during Galvatech 2017 [64]. The objective of the research was to correlate the evolution of spectral emissivity with physical and chemical surface characteristics. The article presents room temperature near-normal spectral emissivity of DP780 and DP980 for as-received (AR), “A”, “B”, “Full” and “Long” conditions. The paper showed that it is possible to observe the shape and composition of surface oxide and to relate changes of spectral emissivity with oxide shape and composition. Spectral emissivity of DP780 varies significantly during intercritical annealing. Moreover, surface oxide thickness and Mn/Si ratio increase throughout the heat cycle. However, spectral emissivity, oxide thickness and Mn/Si ratio are more stable in the case of DP980 than for DP780. The differences in behavior between the two alloys could be due to the Mn/Si ratio of the base material, which is higher for DP780 than for DP980. Changes in spectral emissivity induced by oxidation can lead to temperature deviation during temperature measurements by pyrometry.

Following the article, this thesis presents additional spectral emissivity measurements and surface analysis including AFM and WLI results that were not presented in the article. Furthermore, the effect of increasing the dew point during annealing on spectral emissivity and oxidation with the aim of reducing surface oxidation and spectral emissivity variations is investigated. Finally, spectral emissivity values measured in the Gleeble for temperatures more relevant to intercritical annealing in the Gleeble in order to quantify the effect of temperature on spectral emissivity are presented.

CHAPTER 4 ARTICLE I: EFFECT OF OXIDATION ON EMISSIVITY FOR DP780 AND DP980 STEELS

Article published in the proceedings of the 11th International Conference on Zinc and Zinc Alloy Coated Steel Sheet, November 12th-16th 2017, The University of Tokyo, Tokyo, Japan, pp. 210-217.

Authors : Quentin Somveille[1], Paul Mosser[1], Myriam Brochu[1] and Kyle Daun[2]

[1] École Polytechnique de Montréal, Département de Génie Mécanique

[2] University of Waterloo, Department of Mechanical and Mechatronics Engineering

4.1 Abstract

Temperature control during heat treatment of AHSS steels is critical for obtaining the desired mechanical properties, but accurate pyrometry requires detailed knowledge of the spectral emissivity of the steel. The present work explores the relationship between spectral emissivity and the surface state of two types of cold-rolled dual-phase steels, DP780 and DP980, along with the consequential impact on pyrometrically-inferred temperatures. Results show that the spectral emissivity of DP780 is more influenced by the heat treatment cycle than that of DP980. SEM observations and GDEOS measurements show that the oxide coverage and thickness are smaller for DP980 when compared to DP780.These measurements indicate that low wavelength spectral emissivity increases with oxide thickness and coverage.

Keywords: emissivity, pyrometer, advanced high-strength steel, temperature control, oxidation

4.2 Introduction

Obtaining the desired properties of galvanized steel relies on precise temperature control throughout the heat treatment process. Temperature measurements must be carried out by infrared thermometry, usually with single or dual-wavelengths pyrometers. Unfortunately, these readings are sensitive to the spectral emissivity of the material, which often changes in an uncertain way throughout the continuous galvanizing process [55]. Therefore, a detailed understanding of the

relationship between the surface state, in terms of roughness and oxide layer formation, is needed to obtain correct pyrometric temperatures. The influence of atmosphere on surface state has been studied for a long time, as it pertains to galvanizing, but to the best of the authors' knowledge, only Ham et al. [55] have attempted to connect surface state to spectral emissivity for galvanizing. Our study focuses on two grades of dual phase (DP) steels widely used in the automotive industry: DP780 and DP980. Both studied alloys were cold rolled. Mechanical properties of DP steels were shown to be more sensitive to temperature deviation during annealing than other AHSS steels like HSLA [16].

In the case of single-wavelength pyrometry, the spectral incandescence measured by the pyrometer is related to the steel temperature by

$$J_\lambda = C_\lambda \, I'_\lambda(\lambda, T) = C_\lambda \, \varepsilon'_\lambda(\lambda, T) \, I'_{b\lambda}(\lambda, T) \tag{4-1}$$

where C_λ is a calibration constant that depends on the photoelectric efficiency of the detector, the detector optics, and the detector solid angle, I'_λ is the directional intensity leaving the steel corresponding to the angle formed between the surface normal of the steel sheet and the detector view axis, $I'_{b\lambda}(\lambda, T)$ is the blackbody spectral intensity,

$$I'_{b\lambda}(\lambda, T) = \frac{C_1}{\lambda^5 [\exp\left(\frac{C_2}{\lambda T}\right) - 1]} \approx \frac{C_1}{\lambda^5 \exp\left(\frac{C_2}{\lambda T}\right)} \tag{4-2}$$

with C_1=3.7418×10^{-16} W·m^2 and C_2=14,388 μm·K, and $\varepsilon'_\lambda(\lambda, T) = I'_\lambda(\lambda, T)/I'_{b\lambda}(\lambda, T)$ is the directional spectral emissivity.

Equation (4-1) can be rearranged to solve for temperature provided that the spectral emissivity at the detection wavelength is known. Unfortunately, ε'_λ is rarely known with a high degree of certainty, which severely limits the reliability of temperatures inferred from single-wavelength pyrometry. Because of this multi-wavelengths pyrometry is sometimes used in the steel industry. For two-wavelength (or "two-color") pyrometry,

$$T = \frac{C_2(\lambda_2^{-1} - \lambda_1^{-1})}{\ln\left(\frac{J'_{\lambda_1}}{J'_{\lambda_2}} \frac{\lambda_1^5}{\lambda_2^5} \frac{\varepsilon'_{\lambda_2}}{\varepsilon'_{\lambda_1}}\right)} \tag{4-3}$$

where $\varepsilon'_{\lambda_2}/\varepsilon'_{\lambda_1}$ is usually taken to be unity. The temperature inferred from two-color pyrometry is, in principle, more robust to uncertain spectral emissivity as long as the surface can be approximated as grey over the detection wavelengths.

This is often not the case for steel, however, and it has been shown that neglecting the spectral dependence of ε'_{λ} can lead to uncertainties in the inferred temperature on the same order as those expected from monochromatic pyrometry [10]. While this error can be mitigated by choosing the detection wavelengths to be close to each other, this is done at the expense of measurement sensitivity. It is sometimes possible to mitigate the error caused by uncertain spectral emissivity by aiming the pyrometer at a wedge formed by the metal sheet and the conveyor rollers, which increases the "effective" spectral emissivity [9]. The quality of this approximation depends on the measurement spot size and the angle formed by the rollers, and the effective emissivity may still be significantly less than unity and vary with wavelengths. Moreover, the steel temperature often needs to be measured where a wedge is not present, or the configuration of the line will disallow location of a pyrometer.

An alternative approach is to incorporate the spectral emissivity in the pyrometry measurement model, which is possible if there is detailed knowledge about how the spectral emissivity varies with surface composition, roughness, and temperature throughout the process. This study focuses on characterizing how the spectral emissivity evolves during the heat treatment and explains the modification mechanism in terms of roughness and oxidation. The final goal of this project is to propose values of spectral emissivity throughout the heat treatment process in order to improve temperature control in the furnace and investigate certain physical and chemical characteristics of the steel and how their evolution correlates with the one of emissivity.

4.3 Experimental Protocol

This study focuses on two dual phase steels: DP780 and DP980. Their nominal chemical composition conforms to ASTM A1079-17 [17] detailed in Table 4-1.

Table 4-1: Maximal chemical composition of DP780 and DP980 [17]

% mass max.	C	Mn+Al+Si	P	S	Cu	Ni	Cr+Mo	V+Nb+Ti
DP780	0.18	5.40	0.080	0.015	0.20	0.50	1.40	0.35
DP980	0.23	6.00	0.080	0.015	0.20	0.50	1.40	0.35

While the exact composition of the coupons is proprietary, Table 4-2 reports the Mn/Si ratio measured by spark atomic emission spectrometry [65].

Table 4-2: Chemical atomic composition of our steels

Mn/Si	% mass	% atomic
DP780	11.3	5.8
DP980	4.3	2.2

Steel samples were processed within a galvanizing simulator at McMaster University [66] according to two heating schedules representative of those used in industry, as shown in Figure 4-1. The dew point inside the chamber was maintained at 243K (-30°C) using a reducing (95% N_2+5% H_2) atmosphere to suppress oxidation. Ex situ characterization was performed on samples obtained by interrupting the cycles at points A, B and Full Cycle ("Full"), as shown in Figure 4-1, and then rapidly quenching the samples with nitrogen to suspend the surface state. In order to investigate the influence of process time on surface state, we carried out a second cycle on DP980 (denoted "Long") that extended the duration between points A and B to 20 min instead of 35 s, corresponding to sample temperature of 977K (704°C). The temperatures at which the cycles are interrupted are summarized in Table 4-3.

All samples were cleaned in isopropanol before the heat treatment and prior to radiative and metallurgical characterization. A spectrophotometer (Perkin Elmer Lambda 1050) measured the spectral directional-hemispherical reflectivity $\rho'_{\lambda-d/h}$ between 0.6-2.5 μm. At longer wavelengths (2.5-25 μm) an FTIR reflectometer (Surface Optics SOC-100) was used to measure the spectral hemispherical-directional reflectivity $\rho'_{\lambda-h/d}$. Both instruments measure the near-normal (7°) directional-hemispherical reflectivity, and given that the specimens are opaque, the near-normal spectral emissivity is obtained through Kirchhoff's law

$$\varepsilon'_{\lambda} = \alpha'_{\lambda} = 1 - \rho'_{\lambda - d/h} = 1 - \rho'_{\lambda - h/d} \quad (4\text{-}4)$$

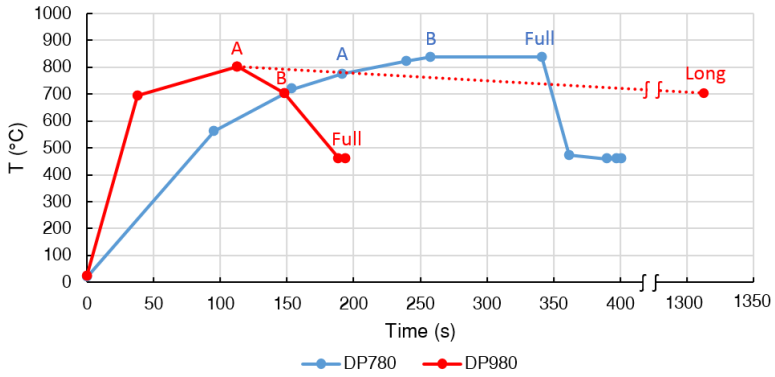

Figure 4-1: Heat cycles applied to the steels (blue: DP780; red: DP980).

Table 4-3: Summary of the temperature at which the heat treatments were interrupted

	A	**B**	**Full**	**Long**
DP780	1048 K (775°C)	1113 K (840°C)	1113 K (840°C)	-
DP980	1075 K (802°C)	977 K (704°C)	736 K (463°C)	977 K (704°C)

Roughness was measured using a contact profilometer (Surftest SJ-210). The surface profile is usually quantified by parameters like R_q, which is the root mean squared value of height of the profile (RMS). However, this parameter by itself is known to be insufficient for describing the relationship between surface roughness and spectral emissivity [67]. Thus, we also measured the skewness R_{sk}

$$R_{sk} = \frac{1}{L.R_q^3} \int_0^L z^3(x)\, dx \quad (4\text{-}5)$$

and kurtosis R_{ku}

$$R_{ku} = \frac{1}{L.R_q^4}\int_0^L z^4(x)\,dx \tag{4-6}$$

which are the third and fourth moments of the RMS roughness heights, respectively. In Eqs. (4-5) and (4-6), L denotes the measurement length, which is 4 mm for the present study. The relationship between R_q, R_{sk} and R_{ku} and surface morphology is depicted in Figure 4-2.

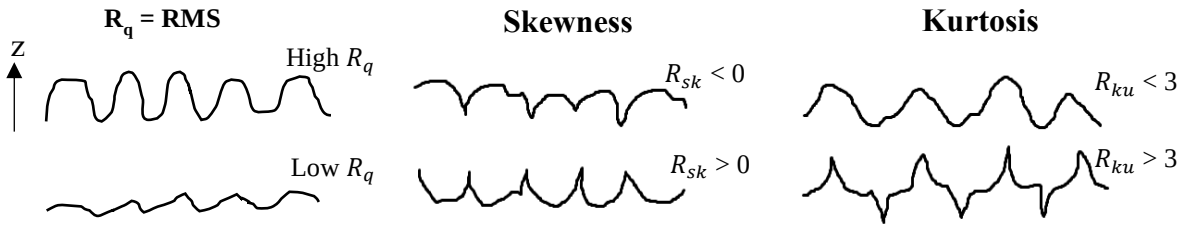

Figure 4-2: Schematic illustrations of profiles with various R_q, skewness and kurtosis [63]

Glow-discharge optical emission spectroscopy (GDOES) was used to infer the presence and thickness of an oxide layer based on time-resolved concentration profiles of oxygen and other elements. SEM surface observations were also performed along with energy dispersive X-ray spectrometry (EDS) analysis to identify oxide on the surface and inspect the oxide coverage evolution during the heat treatments.

4.4 Results

4.4.1 Emissivity Results

Spectral emissivity results for DP780 obtained using the spectrophotometer and FTIR reflectometer are presented in Figure 4-3. Each curve is the average of eight measurements: two measurements on each face of two specimens. In order to compensate for any effect of the specimen orientation due to, for instance, the rolling direction, the samples were rotated by 90° between every measurement, although there was no obvious correlation between sample orientation and spectral directional emissivity. The spectral emissivity data for the as-received, ("AR") metal before heat treatment is also plotted.

The results show that the spectral emissivity decreases and tends to a constant value with wavelengths for both the as-received and heat treated samples. The spectral emissivity of DP780 at short wavelengths ($\lambda < 2.5\ \mu m$) increases during the heat treatment, while, in contrast, the spectral emissivity at longer wavelengths ($\lambda > 2.5\ \mu m$) decreases during the heat treatment. This phenomenon may be due to the fact that surface oxidation appears preferentially in valleys of the as-received steel and tends to smoothen the surface, which is most pronounced at short wavelengths, since optical roughness depends on the ratio of the physical roughness and the wavelength (e.g. R_q/λ) [57].

Spectral emissivity results for DP980 are presented in Figure 4-4. Spectral emissivity for as-received DP980 is higher than the as-received DP780. Again, the spectral emissivity becomes larger with heat treatment time at short wavelengths ($\lambda < 2\ \mu m$), and lower at longer wavelengths ($\lambda > 2\ \mu m$). DP980 appears to be less sensitive to heat treatment than DP780, since spectral emissivities of "A", "B" and "Full" specimens are closer to those of as-received specimens for DP980 than for DP780. Spectral emissivities for "A", "B" and "Full" specimens are nearly indistinguishable in Figure 4-4, and the emissivity of the "Long" specimens remains nearly unchanged after an additional 20 min of heating.

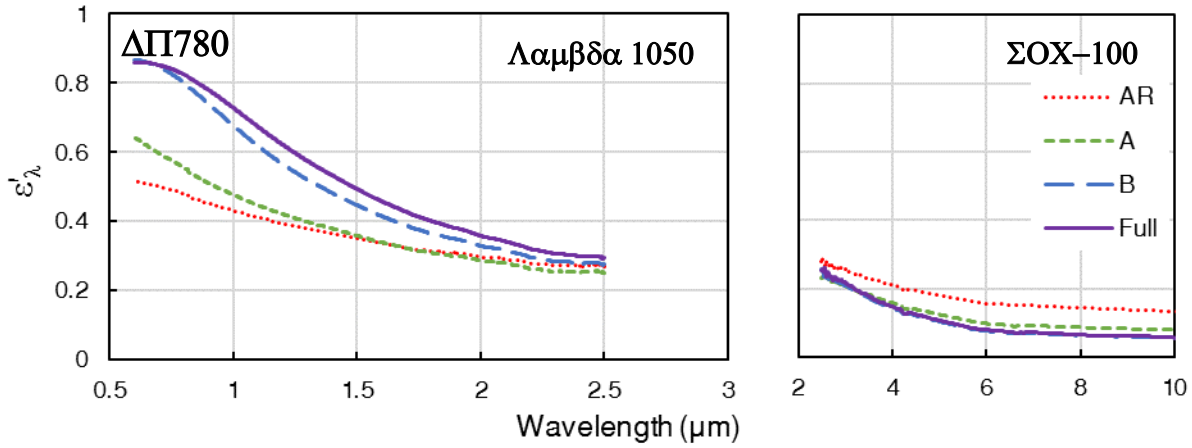

Figure 4-3: DP780 emissivity results for both devices. “A”, “B”, and “Full” correspond to points in Figure 4-1, while “AR” denotes the as-received samples

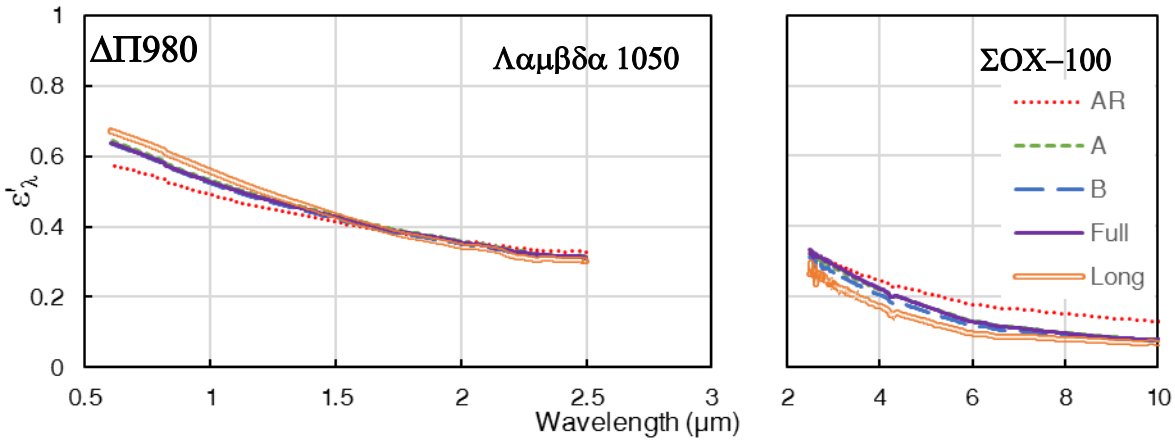

Figure 4-4: DP980 emissivity results for both devices. “A”, “B”, and “Full” correspond to points in Figure 4-1, while “AR” denotes the as-received samples

4.4.2 GDOES Results

GDOES measurements were performed in order to investigate the composition and growth of the oxide layer during heat treatment. Atomic concentration with depth was measured for O, Fe, Mn, Si and Cr. Each test consisted of two trials. Samples of DP780 “A” and “Full” were studied as well DP980 “A”, “B”, “Full” and “Long”. Figure 4-5 illustrates an example profile obtained on a specimen of DP980 “B”[1].

The concentration values are normalized so that the concentrations of Fe, O, Mn, Si and Cr summed to 100%, without accounting for other elements present in the base metal. The iron concentration is lower relative to O, Mn, Si and Cr on the surface compared to the base metal composition, which could indicate a surface layer composed of manganese oxides and silicon oxides. As the surface depth increases, the concentrations approach constant values, although it is notable that oxygen is detected at a large depth (more than 0.2 μm), which may indicate oxidation within the base metal [69]; also, because the sputtering front is spatially-nonuniform, the measured signal consists of contributions from all sample depths. Figure 4-6 shows oxide layer thicknesses inferred from the GDOES results; oxide layer thickness was taken to be the depth at which oxygen atomic concentration is less than 10 %. Each bar is the average of two measurements performed on two specimens and the error bars correspond to each sample. Note that these results assume a continuous oxide layer on the surface of the steel, which is addressed later in the paper.

The DP780 oxide thickness grows by a factor of 2-3 between “A” and “Full”, and corresponds to a visible change in coloration and matification of the specimen surface. In contrast, while the GDOES-inferred oxide thickness for DP980 is larger than that for DP780, it remains nearly constant at 70 nm throughout the heat treatment. There is also no visible coloration of the DP980 samples during heat treatment. This could be due to the fact that Mn/Si ratio is almost three times higher for DP780 than for DP980, cf. Table 4-2. Thus, silicon oxide, which behaves as a dielectric, could grow preferentially on DP980 and protect the steel from further oxidation [10, 30] whereas manganese oxide would grow more on DP780 during the heat treatment. This hypothesis is supported by Figure 4-7, which shows the GDOES-derived surface atomic Mn/Si ratio is higher

[1] All the GDOES profiles analyzed in the article are shown in Appendix D.

for DP780 than for DP980, and the ratio grows with heat treatment for DP780 while it remains nearly constant for DP980. This phenomenon was also observed by Staudte et al. [32] who found that oxidation resistance of AHSS steels improved as the Mn/Si ratio became lower.

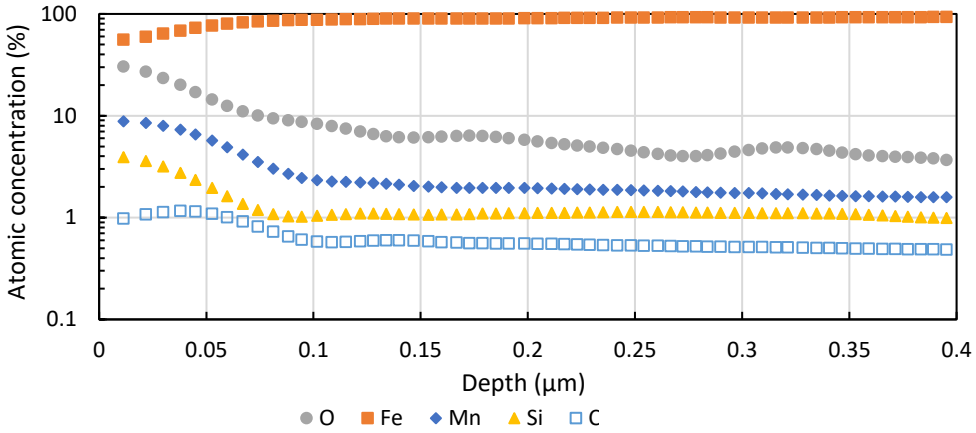

Figure 4-5: Concentration profiles for DP980 B, obtained by GDOES

Overall, the DP780 oxide layer grows significantly throughout the heat treatment, while that of DP980 is comparatively stable. We also observe that the spectral emissivity of DP780 also varies more during the heat treatment than that of DP980, which could imply a causal relationship between spectral emissivity and oxide layer growth.

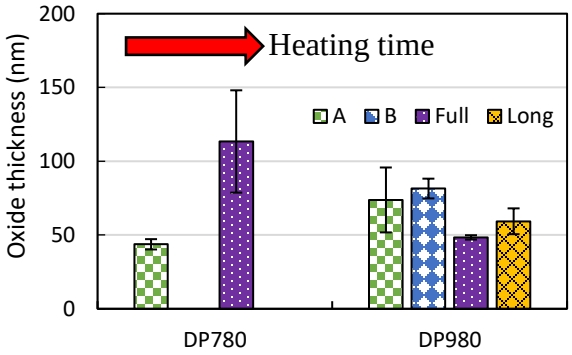

Figure 4-6: Oxide thickness on DP780 and DP980 using criterion C_O < 10%$_{at.}$ measured from GDOES data

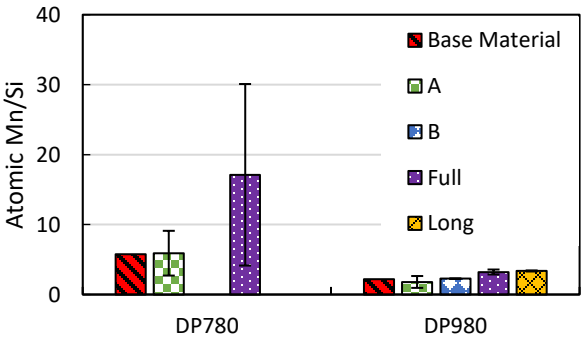

Figure 4-7: Evolution of the surface atomic Mn/Si ratio throughout the heat treatment measured from GDOES data

4.4.3 Roughness Results

Profilometry was used to infer how oxidation altered the surface morphology. Profilometer results for R_q, R_{sk} and R_{ku} are presented in Figure 4-8. Each bar corresponds to the average of eight measurements performed in the same way as the spectral emissivity measurements: two readings on both faces of two specimens for each cycle, and every specimen was rotated by 90° between each measurement. Error bars correspond to the standard deviation of the mean.

The RMS roughness for DP780 is 2-3 times higher than for DP980. While one may expect the spectral emissivity to increase with surface roughness for the same material [56, 57], the spectral emissivity of as received DP780 is lower than that of DP980. This result could be attributed to differences in the composition of the base metals, or the presence of an oxide layer on the as-received specimens (these samples were not tested with GDOES). Figure 4-8 also shows that R_q remains approximately constant for both materials during heating. These results should be interpreted with caution, however, since in principle the instrument cannot distinguish surface features smaller than the tip radius (5 µm), while the R_q values obtained from the instrument are below the extremity tip radius of the profilometer. This suggests that the profile measured by the profilometer is smoother than the actual surface, and aspects of the surface roughness that may affect spectral emissivity at short wavelengths are not captured by the profilometer [70].

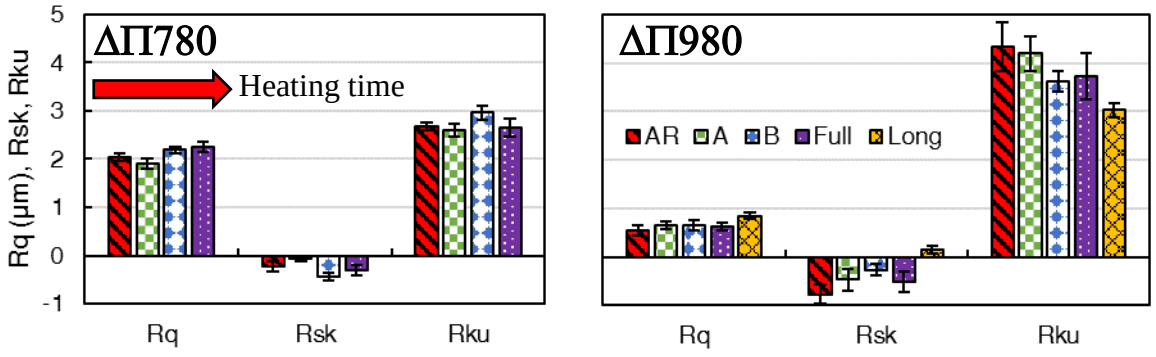

Figure 4-8: Evolution of R_q, R_{sk} and R_{ku} for both materials during the heat treatment

Skewness and kurtosis are presented in Figure 4-8. The skewness for DP780 is negative, indicating a surface topography of more "valleys" than "peaks". The profile density function distribution is platykurtic since $R_{ku} < 3$. Neither of these parameters varies significantly during the heat treatment. In contrast, the skewness of DP980 surfaces increases during the heat treatment, especially when comparing as-received and "Long" specimens. Moreover, R_{sk} is negative for "AR", "A", "B" and "Full" and is positive for "Long" specimens. The profile density function distribution is leptokurtic for all series of data since $R_{ku} > 3$. Kurtosis decreases for DP980 during the heat treatment, which means that the surface becomes progressively blunter during heating. The variation of R_{sk} and R_{ku} for DP980 could be explained by progressive oxidation during heating and peaks of oxide appeared on the surface during the long heat treatment presented in Figure 4-1. It should be noted that this hypothesis appears to be at odds with the GDOES measurements in Figure 4-6, which suggests that the surface phase composition of DP980 remains stable during heating.

4.4.4 Scanning Electron Microscopy

Scanning electron microscopy (SEM) was used to observe the evolution of oxide coverage. Images were taken using a low angle backscatter electron detector (LABe). A low acceleration voltage was used (3keV) in order to minimize the interaction volume, given that the oxide layer is less than 150 nm thick (*cf.* Figure 4-6), while receiving enough signal with the detectors. Oxide was identified from the base metal with EDS analysis.

Figure 4-9 presents SEM images of DP780. The image on the left shows an as-received specimen, while the one on the right shows a sample removed at "A". Oxide appears as small islands less than 100 nm wide, which appear to follow a network of crossing lines spaced at approximately 0.5 µm intervals. This result is consistent with Cvijovic et al. [26], who also observed oxide islands forming on grain boundaries and on the grains of DP steel. Sohn et al. showed the presence of an oxide film between oxide islands on the surface of DP steel [30]. However, this film is not visible on Figure 4-9 using SEM but could be possibly observed using transmission electron microscope.

While the oxide islands would be expected to increase surface roughness, their size (< 0.1 μm) is too small compared to the tip radius of the profilometer (5 μm) to be detected by the instrument. Moreover, the nanoscale roughness is small relative to the wavelengths of light considered in this study (0.6-10 μm), so the impact these oxide islands have on spectral emissivity is unclear.

Figure 4-10 presents SEM images of as-received DP980 (left) as well as a sample heated to the "Full" point as indicated in Figure 4-1. The oxidation for DP980 also follows a network of crossing lines but islands are not visible, and the overall extent of oxidation appears less compared to DP780 on SEM images.

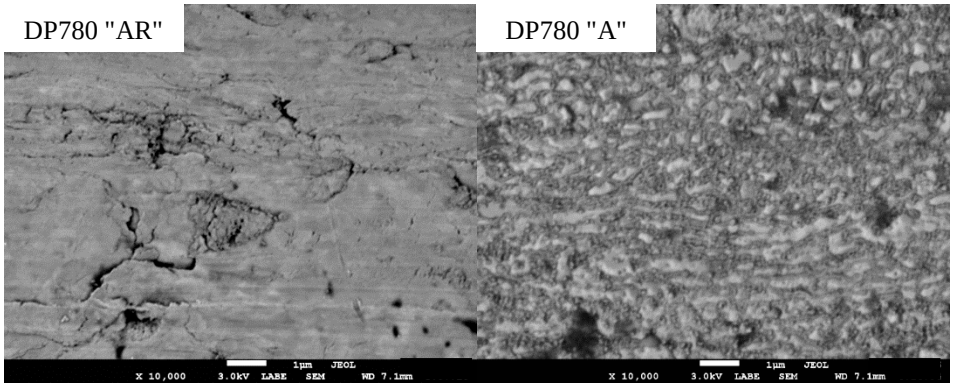

Figure 4-9: SEM images of DP780 (as-received on the left, "A" on the right)

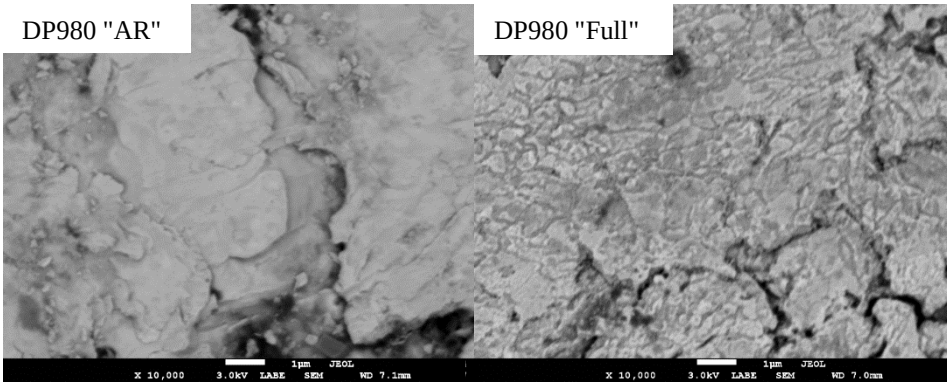

Figure 4-10: SEM images of DP980 (as-received on the left, "Full" on the right)

A comparison of the spectral emissivity measurements with the electron micrographs shows that variations in spectral emissivity and oxide surface state for DP780 is more pronounced than those of DP980, which suggests a relationship between spectral emissivity and oxidation.

4.5 Discussion

Figure 4-3 and Figure 4-4 show that spectral emissivity changes with heat treatment and decreases with wavelengths for all specimens. Wen and Mudawar proposed a model to explain the evolution of the emissivity with roughness [57] depending on the optical roughness defined as R_q/λ. Three regimes were identified: the geometric optics; intermediate; and smooth regimes[2].

In the geometric optics regime, when $R_q/\lambda > 1$ ($\lambda < 2$ μm for DP780 and $\lambda < 0.6$ μm for DP980), the spectral emissivity increases with surface roughness according to a "blackbody cavity effect" [45]. The spectral emissivity of DP780 increases with heat treatment over this wavelength range, which could be attributed to an increase of roughness or the formation of oxide with a higher emissivity than the base metal. We observed a growth of oxide on the surface of the steel as seen in Figure 4-9 but no roughness evolution was observed with our profilometer. For DP980, spectral emissivity was not measured for wavelengths shorter than 0.6 μm.

In an intermediate regime, when $0.2 < R_q/\lambda < 1$ (2 μ$m < \lambda < 10$ μm for DP780 and 0.6 μ$m < \lambda < 3$ μm for DP980), emissivity behavior is difficult to predict. However, if roughness increases, spectral emissivity should also increase and the surface will become more diffuse. For DP780, spectral emissivity decreases with heat treatment in this spectrum while it changes little with heat treatment for DP980. The trend for DP980 is supported by the results of R_q in Figure 4-8 that show no variation of R_q with heat treatment. The trend for DP780 could be due to a decrease of R_q even if no evolution was observed with our profilometer.

[2] Evolution of spectral emissivity of DP780 during intercritical annealing in the three regimes of optical roughness is illustrated in Appendix E.

In the optically smooth or specular regime, when $R_q/\lambda < 0.2$ ($\lambda > 10\ \mu m$ for DP780 and $\lambda > 3\ \mu m$ for DP980), spectral emissivity tends to a constant value with respect to the wavelengths that can be calculated from Fresnel's equation and Kirchoff's law. This trend was confirmed by Wen and Mudawar: spectral emissivity follows an exponential decay with wavelengths, function of R_q/λ due to diffraction effects [57]. All specimens follow this trend. Although, emissivity value at long wavelengths decreases for heat treated specimens compared to as-received ones for both materials. This can be explained by the fact that R_q decreases during the heat treatment or that the chemical composition of the specimens' surface was covered by a material with low emissivity for this range of wavelengths.

Some studies that relate spectral emissivity to the formation and growth of an oxide layer on steel (e.g. Iuchi et al. [71]) attribute changing radiative properties to constructive and destructive wave interference induced by a phase shift caused by the oxide (dielectric) layer, following thin solid film theory. In our case, oxide is not a continuous film, which would appear to disallow this phenomenon.

4.6 Conclusions and Future Work

The spectral emissivity of both materials increases with oxidation during the heat treatment at short wavelengths ($\lambda < 2\ \mu m$) and decreases at longer wavelengths ($\lambda > 2.5\ \mu m$). Moreover, spectral emissivity of DP780 changes more than for DP980 during the heat treatment. DP780 is more prone to oxidation than DP980: oxide is detected up to higher depth with GDOES and is more visible on SEM images. This difference could be explained by the difference in Mn/Si concentration within the base metal: a higher proportion of Si compared to Mn fosters the formation of Si oxide that could protect the surface from further oxidation. The Mn/Si ratio is higher for DP780 than for DP980 and even increases on the surface during the heat treatment for DP780 while this ratio is stable for DP980.

Spectral emissivity measurements for this study were all performed at room temperature. Is it known, however, that spectral emissivity increases proportionally to $T^{1/2}$ via Hagen Rubens theorem [13] so the variation trends observed in Figure 4-3 and Figure 4-4 need to be confirmed at the temperatures of the furnaces. The surface state also depends on the annealing atmosphere, the

dew point, the gas flow rate or H_2 concentration [26, 30, 55, 69]. Also, GDOES was used to measure oxide thickness but since it assumes a continuous layer of oxide on the surface, the obtained values are approximate. Another way to measure oxide thickness would be to use transmission electron microscopy (TEM) on the cross-section of a specimen [30]. Moreover, TEM can reveal the presence of a homogeneous thin oxide film that may not be visible on SEM micrographs. Furthermore, the tip radius of the profilometer is too big to measure the evolution of roughness with the heat treatment, especially R_q. A white light interferometer was also used for the present study but did not give satisfying results. In the future it would be desirable to use atomic force microscopy to better characterize roughness over the scales that may influence spectral emissivity [55, 72].

4.7 Acknowledgements

The authors would like to acknowledge the sponsorship of this project by the Natural Sciences and Engineering Research Council of Canada (NSERC) and the Galvanized Autobody Partnership (GAP) program of the International Zinc Association (IZA). The authors also warmly thank Professor Joseph McDermid and Dr. Beth McNally of the University of McMaster (Hamilton, ON) for the GDOES measurements, making available the galvanizing simulator and their technical assistance and Dr. Bill Baloukas of the Ecole Polytechnique de Montreal (Montreal, QC) for his technical assistance for emissivity measurements.

CHAPTER 5 SPECTRAL EMISSIVITY AND CONNECTION TO SURFACE STATE

This chapter considers additional results that complement the findings in the previous chapter. The chapter begins with additions to Chapter 4, in which GDOES elemental profiles and topography analyses are presented. Then, an investigation on spectral emissivity measurement robustness is presented followed by an analysis of the spectral emissivity of DP780 and DP980 annealed in an atmosphere with 0 °C dew point, and a comparison with the values obtained when the dew point was -30 °C. Finally, spectral emissivity of DP980 at high temperature as measured in the Gleeble is shown and analyzed.

5.1 Complements to the Article

GDOES elemental profiles had not been performed for all conditions by the time the conference paper was submitted; notably results for DP980 “AR” and DP780 “AR” and “B” were incomplete. These results are shown in this section. Moreover, additional topography analyses (as suggested in the paper’s conclusion) were performed with white light interferometry and atomic force microscopy. These results are also presented in this section.

5.1.1 GDOES Measurements

Figure 5-1 presents the GDOES profiles performed on samples of DP980 “AR” and DP780 “AR” and “B” for Fe, O, Si and Mn. The plots (a) and (b) correspond to DP980 “AR”, the plots (c) and (d) correspond to DP780 “AR” and the plots (e) and (f) correspond to DP780 “B”. The grey bands are considered as the surface oxide layer, the thickness of which was calculated as the depth at which the concentration in oxygen reached 10 %, similarly to Chapter 4. According to Figure 5-1, there is no increase in surface concentration in Mn and Si for the as-received samples, contrary to the heat-treated samples. Consequently, detection of oxygen on the surface of as-received samples

could be due to the presence of impurities or oxidation of the superficial alloying elements, while detection of oxygen on the surface of annealed samples could be due to a layer of Mn and Si oxide.

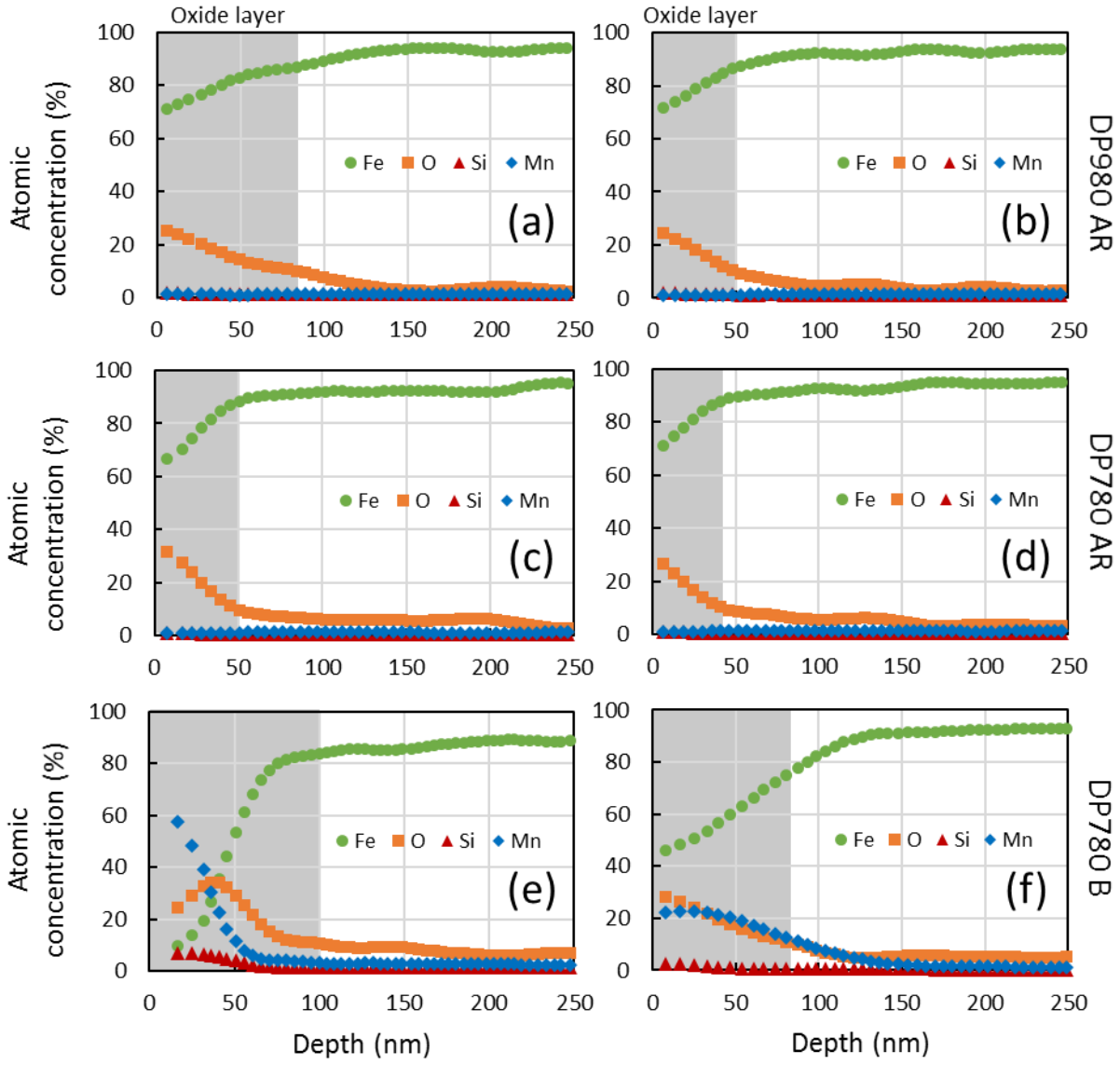

Figure 5-1: Surface elemental profiles obtained with GDOES ((a) and (b): DP980 “AR”; (c) and (d): DP780 “AR”; (e) and (f): DP780 “B”)

Figure 5-2 and Figure 5-3 summarize oxide thickness results and surface Mn/Si ratio values for all conditions. The heat treatment cycles applied to DP780 and DP980 are also recalled. Similar to Chapter 4, each bar in Figure 5-2 and Figure 5-3 is the average of two measurements and the error bars extremities correspond to the measurements performed on each samples. The results confirm the conclusions formulated in the published paper; oxide thickness increases significantly during annealing for DP780, whereas there is no obvious trend for DP980 and similarly for the atomic Mn/Si ratio

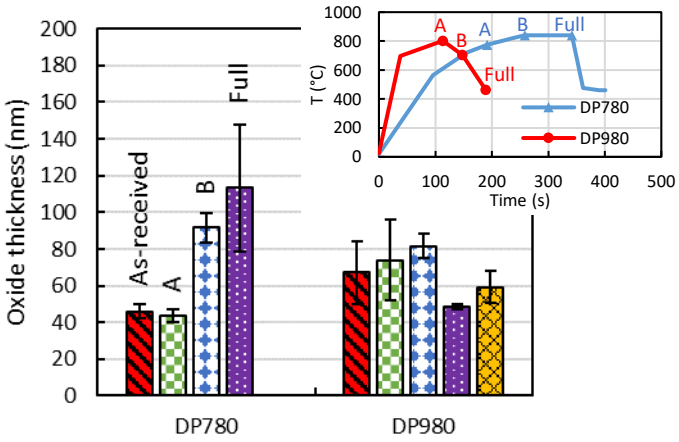

Figure 5-2: Oxide thickness on DP780 and DP980 for all conditions, from GDOES data

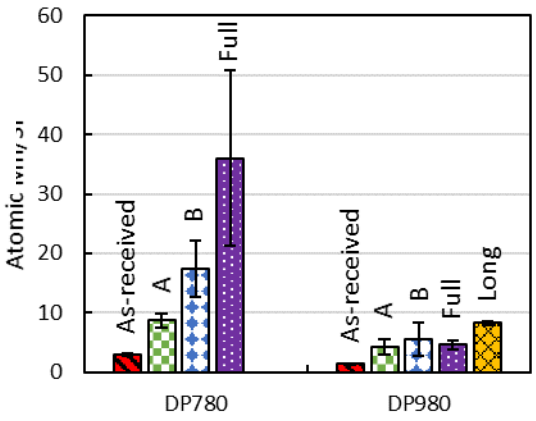

Figure 5-3: Atomic Mn/Si ratio for all conditions, from GDOES data

Only two GDOES measurements were performed per condition; they are represented as the error bars in the graphs presenting oxide thickness (i.e. Figure 4-6, Figure 5-2 and Figure 5-10) and Mn/Si ratio (i.e. Figure 4-7, Figure 5-3 and Figure 5-11). Results presented in this document can be considered qualitative only. Obtaining quantitative results would require more measurements.

Moreover, measurements were not performed on polished specimens ($R_q \approx 2$ µm for DP780 and $R_q \approx 1$ µm for DP980). The oxide thickness measured (≈ 100 nm) is significantly smaller than the topographic amplitudes and this might affect the shape of the sputtering front [73]. Consequently, oxygen could be detected even after sputtering on a height equivalent to oxide thickness. Moreover, numerous alloying elements are present in the alloy. Preferential sputtering could then occur because of the different sputtering yields and could induce uncertainty in the oxide thickness calculation [74].

Furthermore, oxide thickness estimation assumes a continuous oxide layer. This is not perfectly representative of surface oxidation. For instance, it was shown that oxide on the surface of DP780 is distributed as nodules.

In addition, the choice of criterion for oxide thickness determination (10 at.% of O) was arbitrary. This criterion was chosen because it gave results consistent with the literature [30, 31]. Other criteria are used in the literature to determine oxide thickness. For instance, oxide thickness can be considered as the depth at which oxygen concentration reaches 2% [75]. However, using this criterion, the oxide layer thickness estimation would be more than 600 nm on as-received material before annealing, for the present study. This result would be aberrant in regards to the literature.

5.1.2 Topography Analysis

Additional topography analyses were performed with white light interferometry and atomic force microscopy in order to quantify the impact of oxidation growth on topography and roughness with a better definition than with a profilometer. White light interferometry (WLI) measurements were performed first. Figure 5-4 shows typical results obtained with WLI measurements on a 4.4 mm × 1 mm sample. The results shown are for DP780 “AR” and “Full”, which were the conditions that showed most visual differences under SEM inspection. Roughness parameters were also evaluated and did not reveal any significant change between “AR” and “Full”, similarly to what was observed with the profilometer (Figure 4-8). The differences in values between the methods could be due to the differences in cut-off length. Roughness measured by white light interferometry is presented in Figure 5-5. Roughness was measured from the WLI data by a virtual profilometer, following a direction perpendicular to the rolling direction of the steel sheet and over an area of 1 mm × 2.7 mm. Error bars correspond to the standard deviation of the values measured by the virtual profilometer. No significant differences were observed between “AR” and “Full”. The oxide nodules visible on the SEM micrographs are not visible with WLI. The lateral resolution of the instrument may not be sufficient (about 200 nm) to detect the surface oxide nodules (about 100 nm).

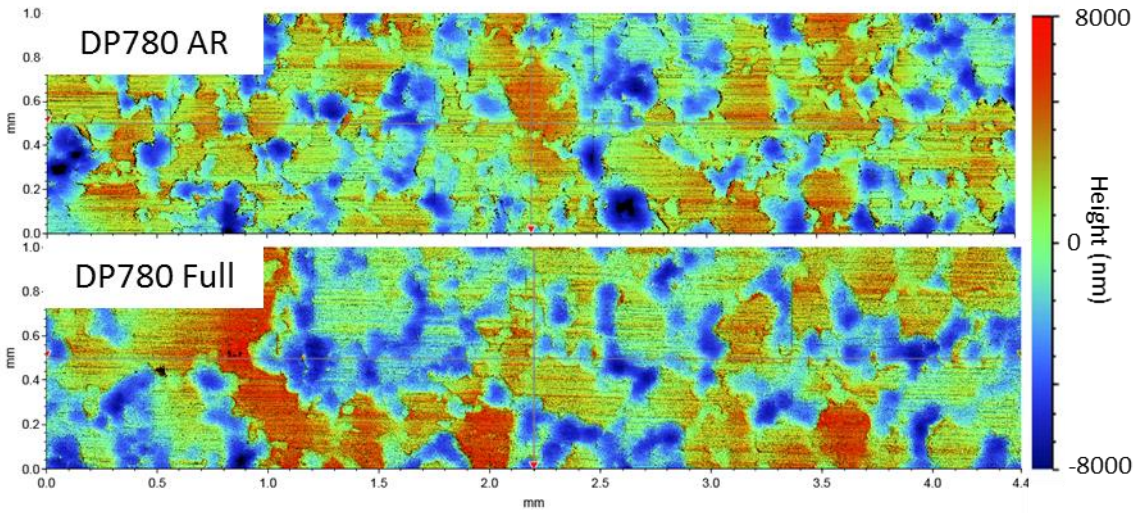

Figure 5-4: White light interferometry (WLI) results for DP780 "AR" and "Full"

(the rolling direction of the steel sheet is horizontal)

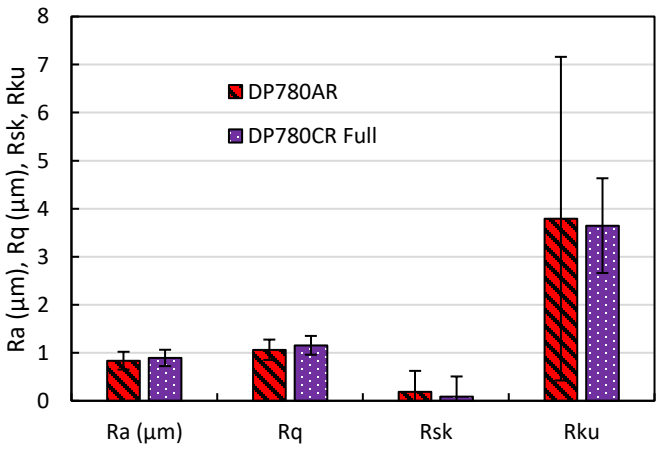

Figure 5-5: Roughness measured by white light interferometry

Atomic force microscopy was then employed on DP780 in the as-received condition and "Full" annealed condition with a dew point of -30 °C, as shown in Figure 5-6. Oxide nodules are visible on the surface of DP780 "Full" but not on the "AR" sample. The oxide nodule size was visually estimated to between 100 and 500 nm, which is similar to what was observed with the SEM micrographs presented in Figure 4-9. This method soundly captures surface topography evolution induced by selective oxidation and is promising for future quantitative measurements.

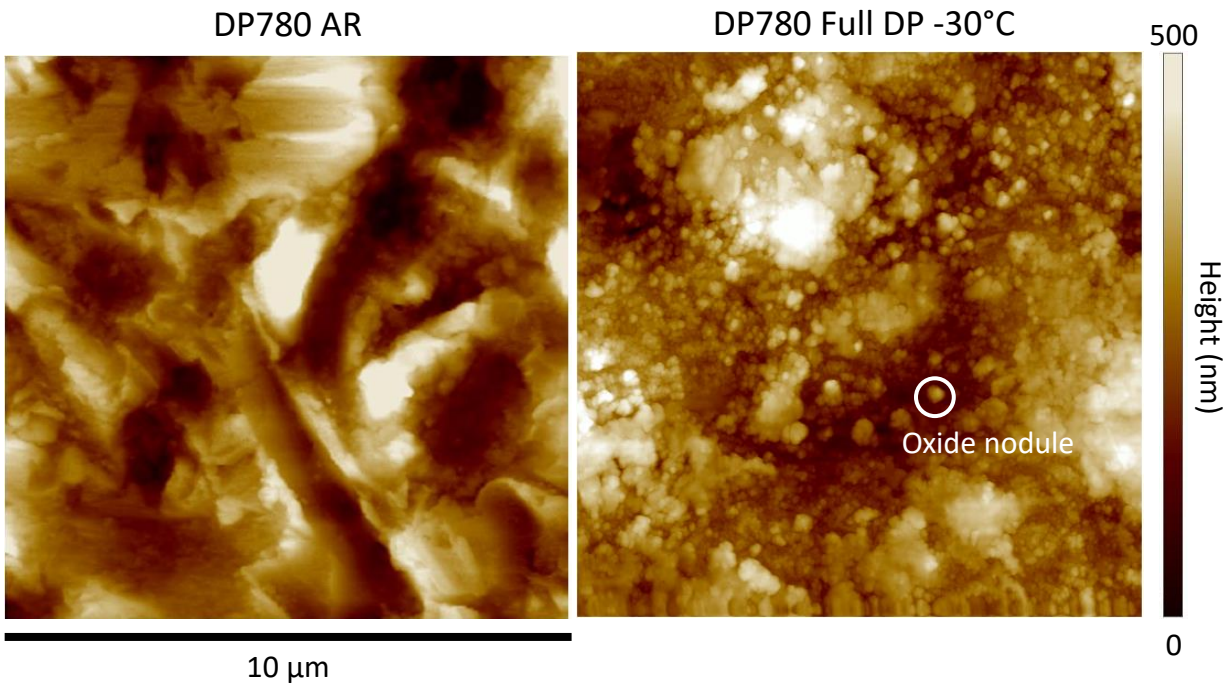

Figure 5-6: Atomic force microscopy (AFM) micrographs on DP780 “AR” and “Full DP -30 °C”

As presented in Chapter 2, roughness affects emissivity. Then, identifying variations trends in surface roughness during annealing could contribute to modeling and predicting the steel spectral emissivity evolution during intercritical annealing and consequently improve the accuracy of temperature measurements by pyrometry.

5.2 Change in Atmospheric Dew Point During Annealing

The impact of the atmospheric dew point on spectral emissivity during annealing was investigated by annealing samples in an atmosphere having a dew point of 0 °C instead of -30 °C. According to Eqs. (2-11) and (2-12), the partial pressure of oxygen at a dew point of 0 °C is 5.89×10^{-21} atm, meaning that the oxygen partial pressure is more than 250 times greater than for a dew point of -30 °C. The emissivities of the samples annealed with dew points of -30 °C and 0 °C were then measured using the spectrophotometer and the FTIR interferometer. Figure 5-7 and Figure 5-8 compare spectral emissivity values of specimens annealed at dew points of -30 °C and 0 °C with as-received specimens for both DP780 and DP980. The change of dew point has a significant impact on DP780 spectral emissivity at short and long wavelengths. At short wavelengths ($\lambda <$ 1.2 μm), spectral emissivity decreases for this material when the dew point increases. At long wavelengths ($\lambda >$ 3 μm), spectral emissivity is greater when the dew point is 0 °C. The difference is negligible for wavelengths between 1.2 and 3 μm

The spectral emissivity of DP780 annealed with a dew point of 0 °C is closer to the spectral emissivity of the as-received material than when it is annealed with a dew point of -30 °C. This could be explained by the fact that oxidation, which happened to surface elements, partially occurs below the surface at a dew point of 0 °C because of the increase in oxygen partial pressure in the annealing chamber. However, in the case of DP980, the change of dew point has little impact on the spectral emissivity for wavelengths longer than 1.2 μm. This may be because the transition from external to internal oxidation occurs at dew point below -30 °C, suggesting that oxidation already occurs below the surface when the dew point is -30 °C.

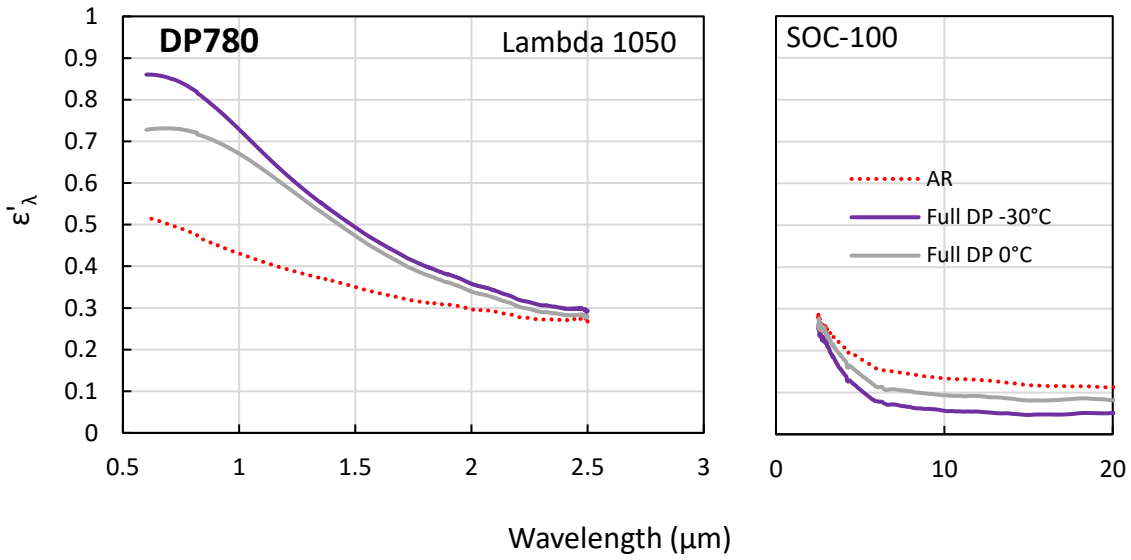

Figure 5-7: Comparison of the spectral emissivities of "Full" specimens of DP780 for both instruments and dew points of -30 °C and 0 °C

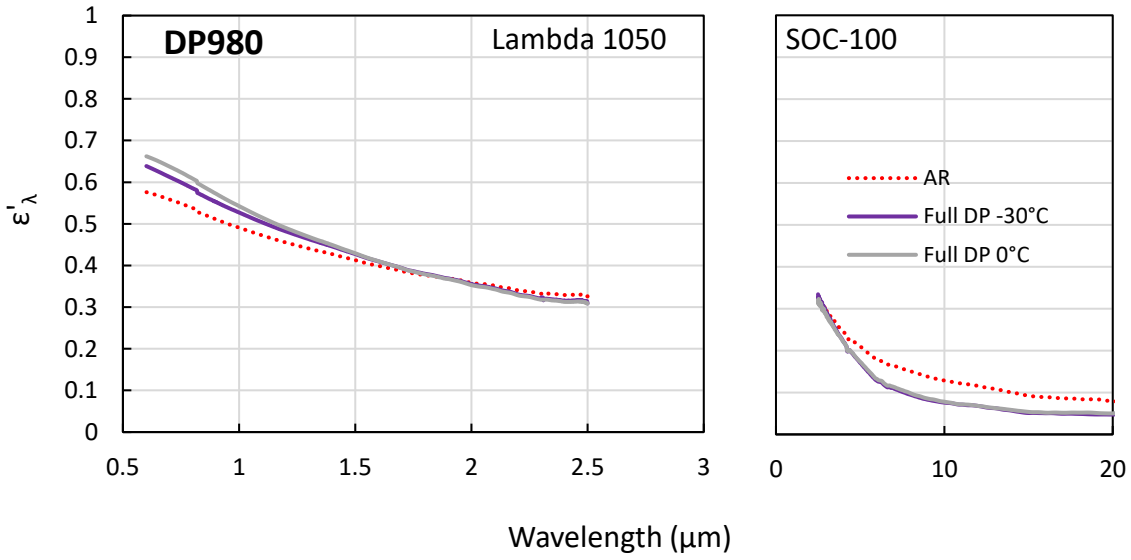

Figure 5-8: Comparison of the spectral emissivities of "Full" specimens of DP980 for both instruments and dew points of -30 °C and 0 °C

In order to inspect the presence of internal oxide in DP980, scanning electron microscopy was carried out on a cross-section cut with focused ion beam (FIB) on a sample of DP980 after intercritical annealing with a dew point of -30 °C, followed by galvanizing. Figure 5-9 Shows that the zinc coating is visible on top of the base metal and was identified by electron dispersive spectroscopy (EDS). The intermetallic layer $Fe_2Al_5Zn_X$ can be observed on the surface and so can internal and external oxide be seen. External oxide is very thin (less than 50 nm) and the surface does not seem to be fully covered by oxide. This, added to the fact that internal oxide is present, supports the hypothesis that the transition from external to internal oxidation for DP980 happens at a dew point below -30 °C.

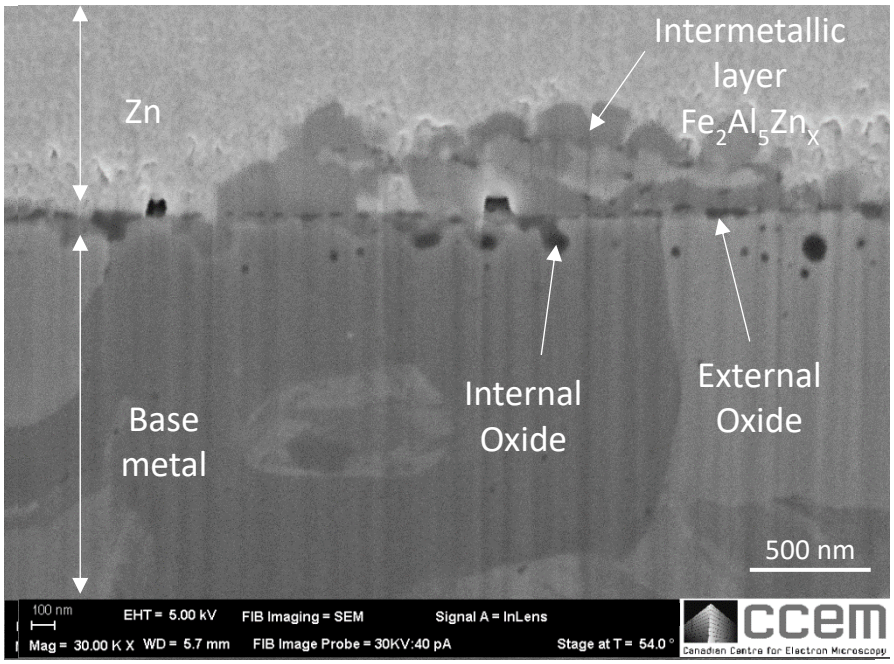

Figure 5-9: Observation of the oxide layer of galvanized DP980

GDOES chemical profile measurements were also performed on samples annealed with a dew point of 0 °C. Thickness estimates and Mn/Si ratio estimates for “AR” and “Full” conditions are presented in Figure 5-10 and Figure 5-11. It can be observed that changing the dew point from -30 °C to 0 °C has little influence on oxide thickness and surface Mn/Si ratio of DP980, in agreement with the fact that the spectral emissivity of DP980 changes little when the dew point

goes from -30 °C to 0 °C (cf. Figure 5-8). Oxide thickness as determined from the GDOES data is in the same range as oxide thickness estimated visually on the SEM micrograph in Figure 5-9.

In the case of DP780, the oxide layer is thinner when the steel is annealed with a dew point of 0 °C than it is with a dew point of -30 °C. This is in agreement with the observed trends in spectral emissivity shown in Figure 5-7 and Figure 5-8. The spectral emissivity of DP780 "Full DP 0 °C" is closer to the spectral emissivity of the as-received material than for the spectral emissivity of "Full DP-30 °C" (cf. Figure 5-7). However, it seems that the surface Mn/Si atomic ratio for "Full" with a dew point of 0 °C is greater than it is with a dew point of -30 °C. This could be explained by the fact that silicon is more oxidizable than manganese (ΔG^0(Si) < ΔG^0(Mn)). Thus, silicon atoms would oxidize at the contact of oxygen below the steel surface, while manganese atoms would migrate to the surface before oxidizing, leading to surface enrichment in manganese compared to silicon. No significant trend is observed for DP980.

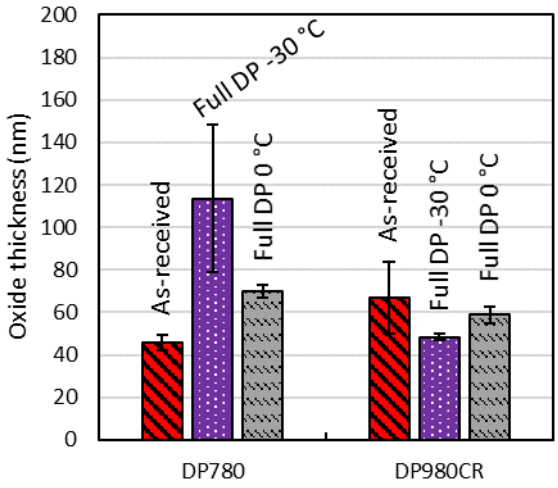

Figure 5-10: Influence on oxide thickness of changing the dew point

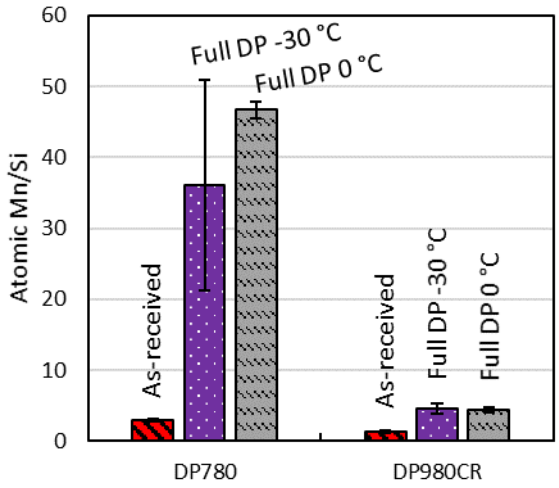

Figure 5-11: Influence on Mn/Si ratio of changing the dew point

5.3 Spectral Emissivity Measurements Robustness Investigation

All the spectral emissivity data presented so far are the average of eight measurements performed for each condition in order to limit the possible effect of random noise and differences between the samples. A focused study was also carried out to assess the robustness and repeatability of the spectral emissivity measurement instruments (Lambda 1050 and SOC-100). The influence of the sample face on spectral emissivity is also examined.

In order to evaluate repeatability of spectral emissivity measurements, three successive identical measurements were performed with the Lambda 1050 and the SOC-100 on a sample without moving the sample between the measurements. The three series of data obtained with the Lambda 1050 are almost identical and indistinguishable on a plot. In the case of the SOC-100, Figure 5-12 presents the results of the three successive identical measurements. There is little difference between results except at short wavelengths (below 3 µm) and long wavelengths (over 20 µm). The deviations observed at short and long wavelengths are due to random noise since average values of eight measurements presented in Figure 4-3, Figure 4-4, Figure 5-7 and Figure 5-8 are stable in these ranges of wavelengths.

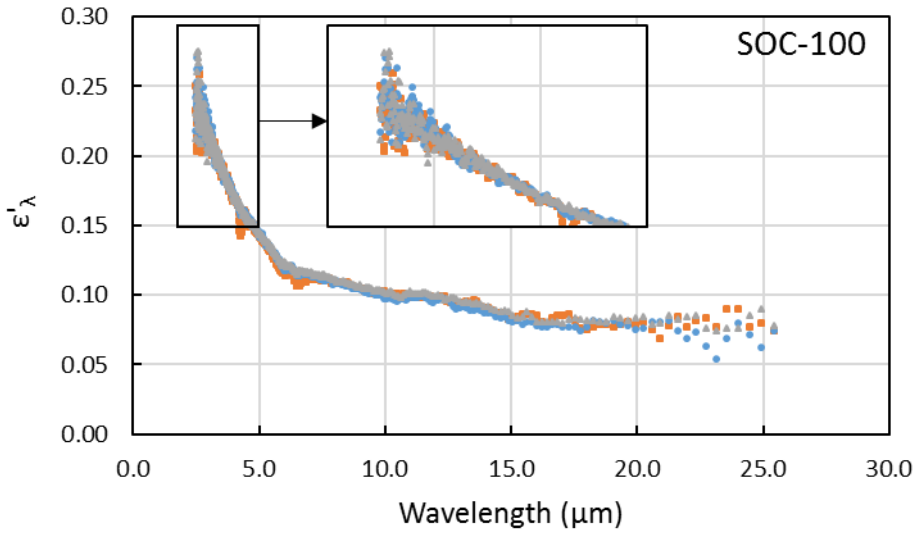

Figure 5-12: Comparison of the results of three identical measurements with the SOC-100

Figure 5-13 presents spectral emissivity of two samples of as-received DP780. Spectral emissivity deviation between these samples is representative of the differences between samples for the other conditions. Each series in Figure 5-13 corresponds to the average of four measurements. Two measurements were performed on each face of the sample and the sample was rotated by 90° between each measurement.

The repeatability of the spectral emissivity measurements is acceptable. The deviation between successive identical measurements is typically smaller than the deviation between measurements performed on different samples.

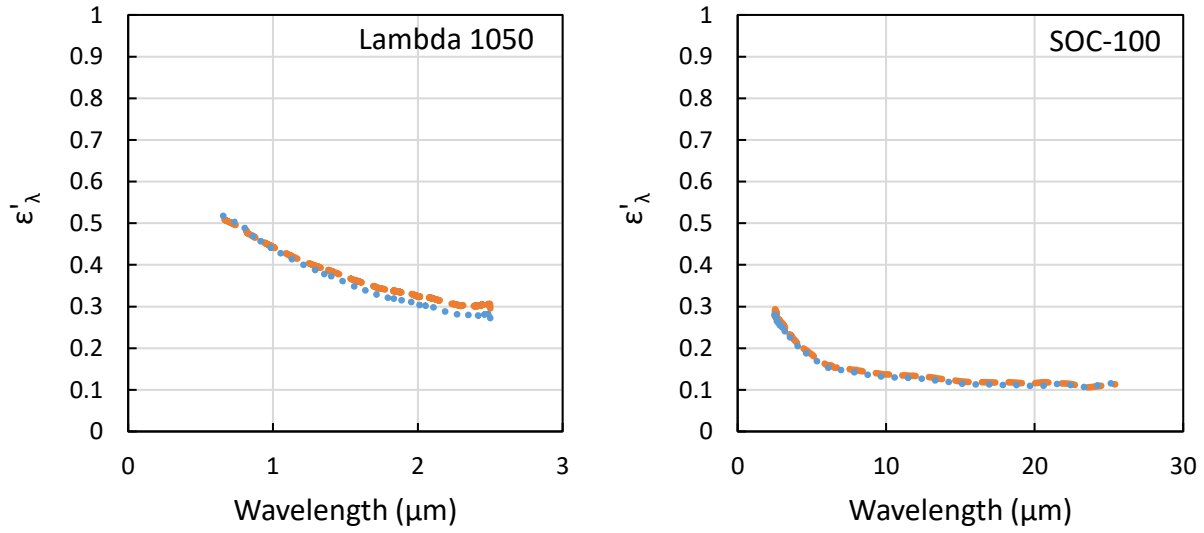

Figure 5-13: Comparison of the emissivities of two samples of as-received DP780

The influence of sample face on spectral emissivity was also investigated. Indeed, the observed spectral emissivity of DP980 has a dependence on specimen face. Figure 5-14 shows spectral emissivity measured on a sample of as-received DP980 for both faces. The specimen was rotated by 90° or translated between each measurement in order to obtain eight data series uniformly distributed on each face. On Figure 5-14, the data appears to be gathered into two groups corresponding to the two specimen faces. Typically, the face with the higher spectral emissivity is the face that looks matte to the naked eye (solid lines). The other face has bright stripes that could be more reflective (dashed lines).

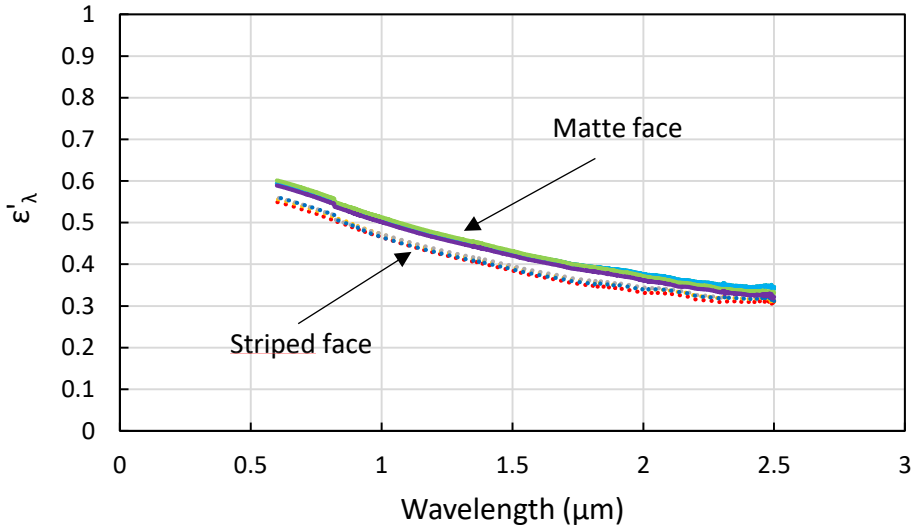

Figure 5-14: Comparison of the emissivities of both faces of a sample of as-received DP980 (continuous upper curves: matte face; dashed lower curves: striped face)

The spectral emissivity of DP780 shows less dependence on specimen face than does the spectral emissivity of DP980. No difference between the faces is detectable with the naked eye when looking at the specimens.

The differences in spectral emissivity between faces show that the steel sheet face selection for temperature measurements can induce temperature reading errors.

Furthermore, differences between samples and faces are smaller than differences observed between conditions in Figure 4-3, Figure 4-4, Figure 5-7 and Figure 5-8. Consequently, the differences observed between conditions are mostly due to surface modifications.

5.4 High-Temperature Spectral Emissivity Measurements

All spectral emissivity measurements presented above were done at room temperature. However, according to Hagen-Rubens' theorem, the spectral emissivity of a metal should increase with its electrical resistivity, via its temperature. To investigate this effect it was then decided to attempt spectral emissivity measurements at temperatures relevant to annealing.

The spectral emissivity of DP980 was measured at high temperature in situ in a Gleeble chamber at the University of Waterloo in an atmosphere composed of 99.999% argon (cf. part 3.3.1.2). The heat cycle that was applied to the steel is shown in Figure 5-15. The cycle is the same as the one that was applied to DP980 in the galvanizing simulator until the first interruption "A" (cf. Figure 3-1). The indicated temperature values were measured using a thermocouple welded in the center of the sample (cf part 3.3.1.2).

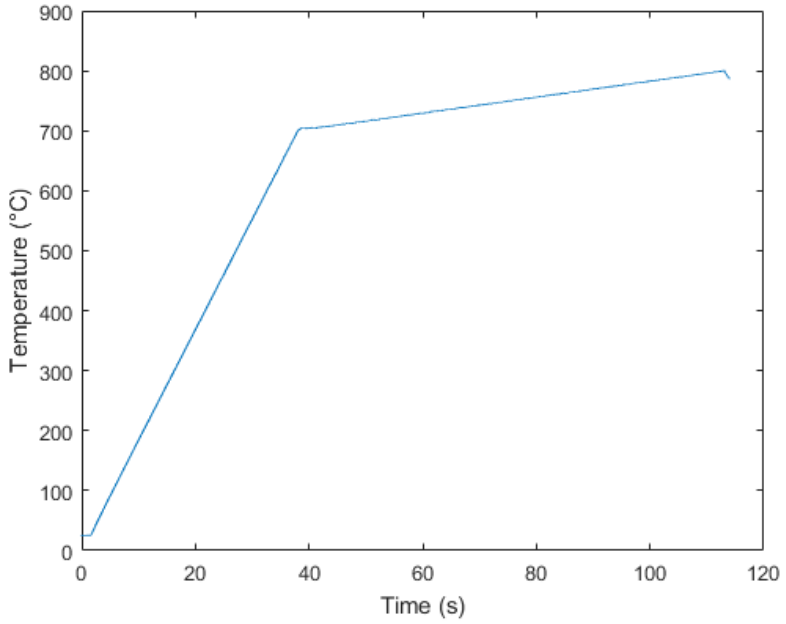

Figure 5-15: Heat cycle applied to the steel in the Gleeble

Normal spectral emissivity as a function of temperature and wavelength is presented in Figure 5-16 for temperatures between 400 and 800 °C and wavelengths between 1.5 and 2.5 µm. This plot indicates that spectral emissivity decreases with wavelength for temperatures below 700°C, in agreement with the results obtained at room temperature. Spectral emissivity increases with temperature until 700 °C, in agreement with electromagnetic theory presented in part 2.3.1 and the growth of oxide similar to Figure 4-4. However, the spectral emissivity decreases for temperatures over 700°C. This phenomenon is easier to see in Figure 5-17, which shows spectral emissivity at a wavelength of 2 µm (the dashed line in Figure 5-16) as a function of temperature.

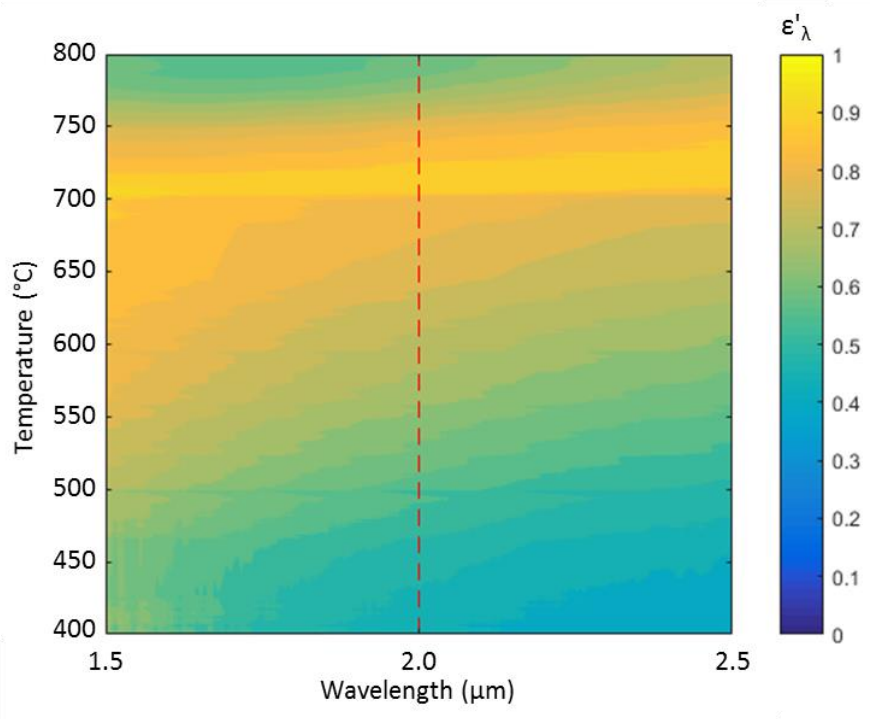

Figure 5-16: Spectral normal emissivity in argon of DP980 as a function of temperature and wavelength

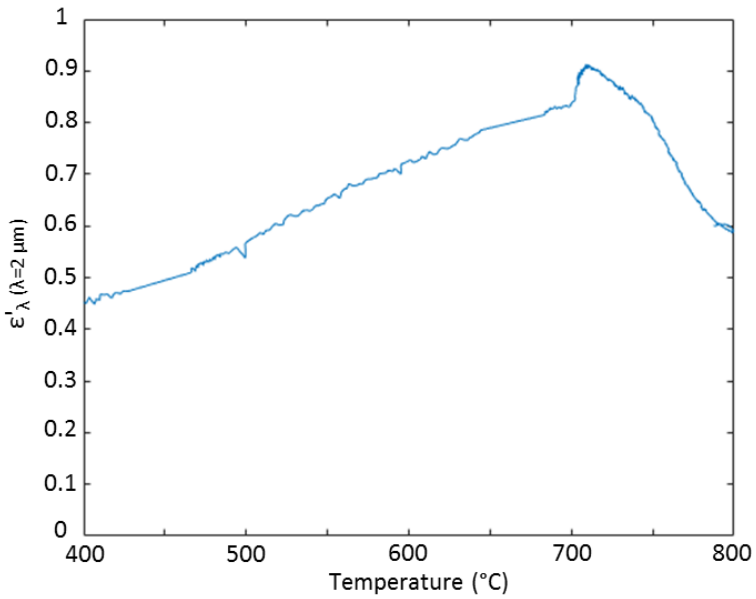

Figure 5-17: Spectral normal emissivity in argon at λ = 2 µm of DP980 as a function of temperature

The reason for the change in spectral emissivity in Figure 5-16 and Figure 5-17 at 700 °C is not clear. It is not due to destructive interference related to the growth of oxide, as studied in the literature review, since spectral emissivity decreases for all wavelengths simultaneously. The formation at 700 °C on the steel surface of a new chemical compound with a low spectral emissivity could explain the change in the sample spectral emissivity.

Figure 5-18 presents the spectral emissivity at room temperature of as-received DP980 ("AR"), DP980 annealed in the simulator ("A"), and DP980 heated in the Gleeble following the cycle presented in Figure 5-15 ("Gleeble"). The sample heat treated in the Gleeble has a completely different spectral emissivity. It is an indication that the surface reactions activated in the Gleeble is different from the oxidation encountered in the galvanizing simulator. The oxide layer seems to be thicker for a sample annealed in the Gleeble since spectral emissivity is high and spectral oscillations are clearly visible, which suggests the interference pattern [50] (cf. part 2.3.2).

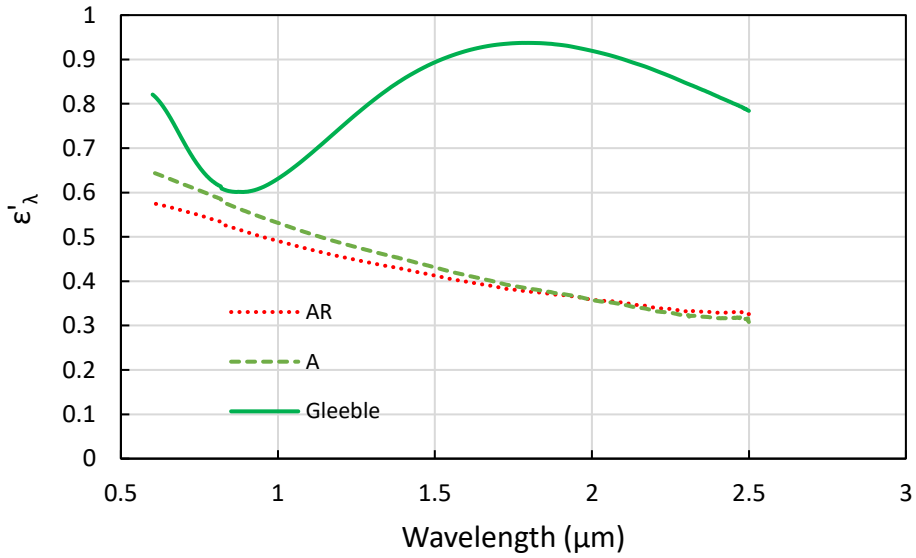

Figure 5-18: Comparison of spectral emissivity at room temperature of DP980 after annealing in the simulator and in the Gleeble

The atmosphere in the Gleeble was composed of 99.999% pure argon. Nevertheless, oxygen concentration in an argon bottle can typically reach 2 parts per million in volume [76], meaning that the expected partial pressure of oxygen in the chamber can be around 0.2 Pa in addition to oxygen from air that was trapped in the chamber. The 2 ppm concentration is much greater than the concentration in the annealing chamber in the galvanizing simulator (2.31×10^{-18} Pa). As described in the Ellingham diagram presented in Figure 5-19, alloying elements and iron itself are susceptible to oxidation at all temperatures of the cycle. Indeed, contrary to part 2.2.2 and Figure 2-2, the standard Gibbs free energy for iron oxidation reactions ΔG_0 (blue lines) is lower than the function $RT \ln p_{O_2}$ (orange line) and $\Delta G < 0$, following Eq. (2-13). This means that iron oxide is expected to grow on the steel surface during heating in the Gleeble, opposite to heating in the simulator. Consequently, spectral emissivity was successfully measured at high temperature, but values measured in the Gleeble cannot be compared with the ones from annealed samples since the oxidation conditions were different.

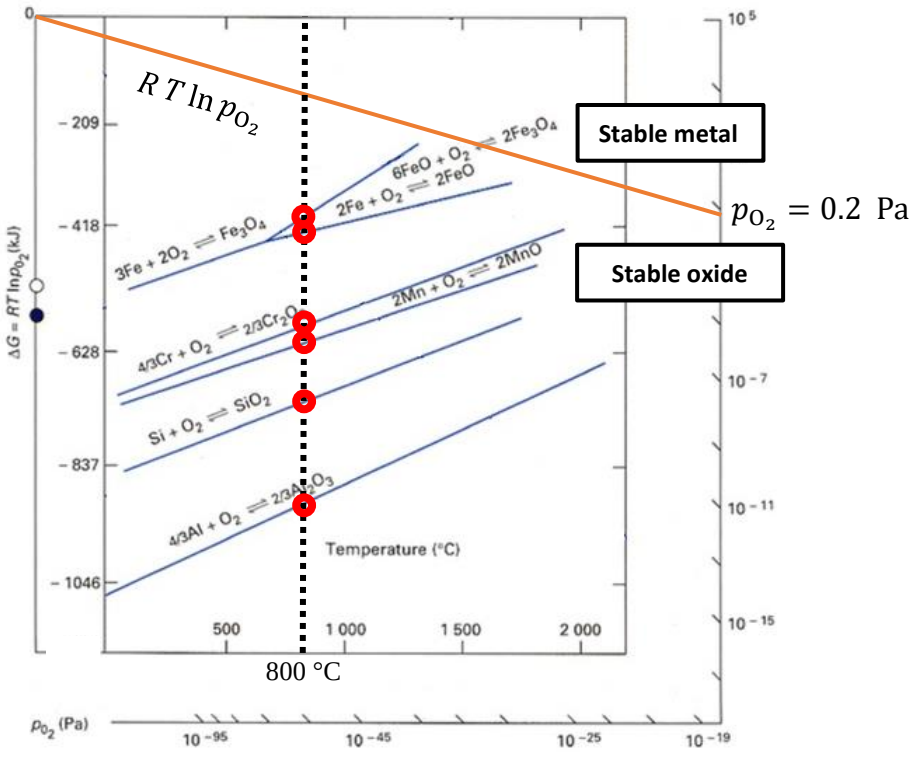

Figure 5-19: Ellingham diagram describing oxidation in the Gleeble [19]

5.5 Coupon Temperature Inhomogeneity

It was noticed, by the end of the project, that the temperatures of the coupons were not spatially homogenous during annealing in the simulator. This difference in temperature is attributed to the flow of gas in the annealing chamber. This gas, when it is injected in the chamber, is cold because of its expansion when it leaves the bottle. Temperature around the thermocouple was close to the nominal temperature, but the sides of the coupons were colder and the center of the coupon was hotter. The true peak annealing temperature at different points of the coupons was estimated by comparing hardness with hardness measured next to the thermocouple on coupons annealed with different peak annealing temperatures. The peak annealing temperature difference between a corner of the coupon and the thermocouple was estimated to be up to 100 °C for DP980 [77]. Then, this temperature spatial inhomogeneity leads to differences in oxidation and thus in the spectral emissivity between the center and the sides of the coupon. Figure 5-20 presents a diagram of a coupon that was annealed in the simulator. The location of the thermocouple on the coupon is symbolized by the black dot. Specimens that were used for spectral emissivity and surface analysis were cut preferentially in the lower part of the coupons, labeled Region (1).

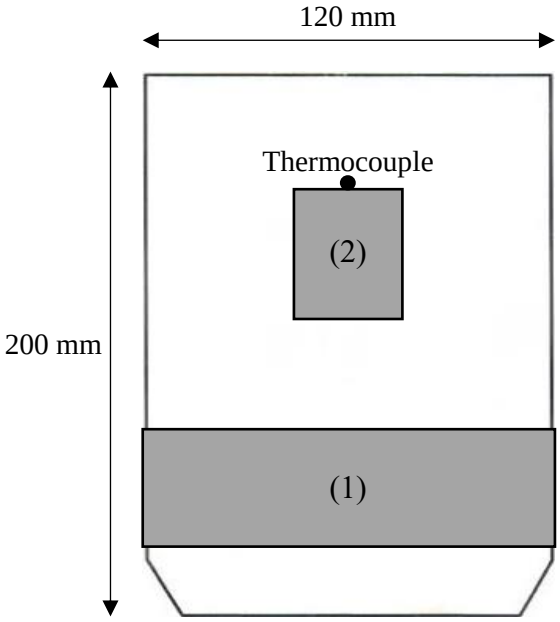

Figure 5-20: Diagram indicating Regions (1) and (2) where samples were cut on the coupon to study temperature heterogeneity

After discovering the temperature heterogeneity, a sample was cut next to the thermocouple of a coupon of DP780 “Full”, labelled Region (2) in order to compare the spectral emissivity of this region with the spectral emissivity of the bottom of the coupon in Region (1). The spectral emissivity curves for these two regions are compared in Figure 5-21. Spectral emissivity near the thermocouple is greater than spectral emissivity at the bottom of the coupon at shorter wavelengths, but approach the same value as the wavelength increases towards 2.5 µm. This trend is the same as the one that was observed during the progression of intercritical annealing in this range of wavelengths between “AR”, “A”, “B” and “Full” conditions. Consequently, annealing at higher temperature seems to be equivalent to annealing for a longer time at lower temperature.

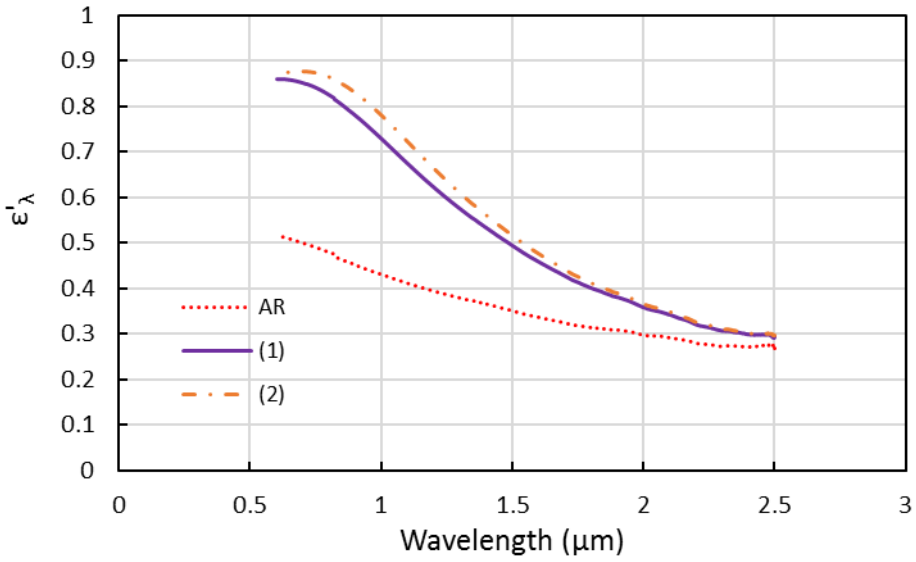

Figure 5-21: Comparison of spectral emissivity of DP780 “AR” measured in Regions (1) and (2) in Figure 5-20 for DP780 “Full”

5.6 Synthesis

The results presented in this chapter have provided confirmation of the following trends:

The oxide thickness and the Mn/Si ratio increase during intercritical annealing of DP780, but do not change as much for DP980. Moreover, among all the topography analysis methods that were employed, only atomic force microscopy seems to give results precise enough to provide a potential explanation of spectral emissivity evolution.

Changing the dew point of the annealing atmosphere from -30 °C to 0 °C reduces surface oxidation of DP780 and then mitigates possible temperature errors. However, increasing the dew point from -30 °C to 0 °C has little effect on DP980. It is possible that transition from external to internal oxidation for DP980 happens at a dew point lower than -30 °C.

The spectral emissivity of DP980 was successfully measured at high temperature in a Gleeble chamber with the available equipment. However, the oxidation state during heating was significantly different from the state obtained in the galvanizing simulator.

The next chapter presents an estimation of the deviations of temperature readings by pyrometry induced by the change in spectral emissivity during intercritical annealing.

CHAPTER 6 GENERAL DISCUSSION

This chapter studies deviations in pyrometry readings that can be induced by spectral emissivity evolution during intercritical annealing. The chapter also presents the effect of the dew point and the effect of the coupon temperature inhomogeneity during intercritical annealing.

6.1 Effect of Spectral Emissivity Evolution during Intercritical Annealing

Near-normal spectral emissivity of DP780 and DP980 for "AR" and "Full" conditions is recalled in Figure 6-1 and Figure 6-2 for wavelengths between 1 and 2.5 µm, which corresponds to most of the wavelengths used for pyrometry in industry according to the survey described in part 3.1.

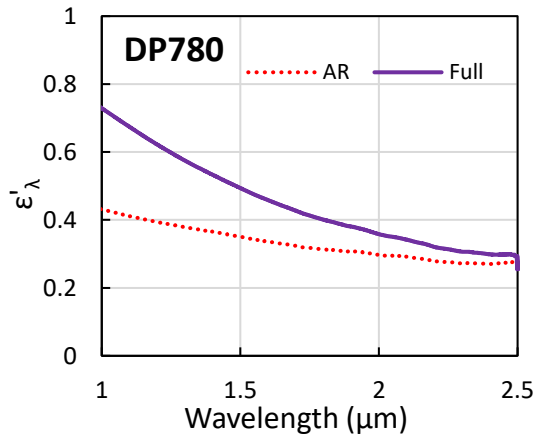

Figure 6-1: Spectral emissivity of DP780 "AR" and "Full" between 1 and 2.5 µm

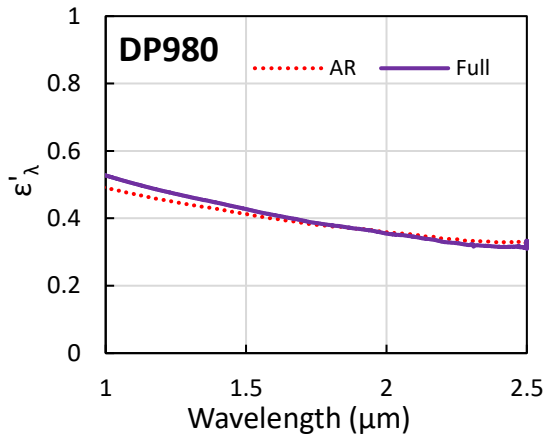

Figure 6-2: Spectral emissivity of DP980 "AR" and "Full" between 1 and 2.5 µm

These changes in spectral emissivity induce the temperature errors presented in Figure 6-3 as a function of wavelength (blue solid line for DP780 and red dashed line for DP980). The values presented in Figure 6-3 correspond to the difference between the true temperature, which would be measured when the spectral emissivity value set in the pyrometer ε'_t is the one of the "Full" condition, and the measured temperature, which would be measured when no correction of spectral emissivity is provided ε'_s (as-received condition). The values are calculated following Eq. (2-5):

$$\Delta T = T_t - T_m = \left[\frac{1}{T_m} - \frac{\lambda}{C_2}\ln\left(\frac{\varepsilon_s'}{\varepsilon_t'}\right)\right]^{-1} - T_m \quad (6\text{-}1)$$

where the measured temperature T_m is 800 °C, the spectral emissivity setting in the pyrometer ε_s' is the value associated with the as-received material, the true spectral emissivity ε_t' is the spectral emissivity of the "Full" condition sample, λ is the wavelength and C_2 = 1.439×10^{-2} m·K.

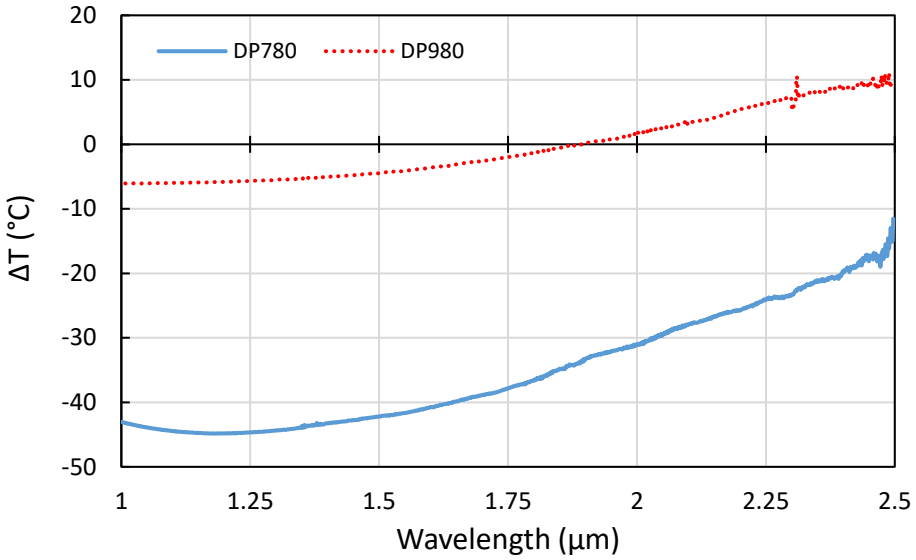

Figure 6-3: Expectable temperature errors for single-wavelength pyrometry

The parts of the spectrum for which temperature error is negative coincide with the parts where spectral emissivity for the "Full" condition is greater than for the "AR" condition. Indeed, a material that has a higher spectral emissivity will emit more radiation and its temperature will be overestimated by a pyrometer.

Temperature errors for DP980 are lower in absolute value than for DP780, since the spectral emissivity changes less in the former case compared to the latter during annealing. Temperature errors are mostly around ±10 °C for DP980 while they can exceed ±45 °C for DP780 in this range of wavelengths, which is consistent with industrial practice (cf. Table 3-1). The change in spectral emissivity could lead to deficient mechanical properties in the case of DP780, since the maximum acceptable temperature error during thermal processing is between 25 and 50 °C [16].

Temperature estimation errors are minimized at wavelengths of about 2 µm for DP980 and between 2.5 and 3 µm for DP780. Performing temperature measurements with pyrometry in these ranges of wavelengths could minimize temperature deviations and reduce the rejection rate of the CGL.

6.2 Effect of Changing the Dew point

It was shown in section 5.2 that increasing the atmospheric dew point from -30 °C to 0 °C during intercritical annealing decreases spectral emissivity evolution. Consequently, increasing the dew point should also affect pyrometric temperature measurements. As recalled in Figure 6-4 and Figure 6-5, the spectral emissivity of DP780 annealed with a dew point of 0 °C ("Full DP 0 °C") is closer to the spectral emissivity of as-received DP780 ("AR") than its spectral emissivity when annealed with a dew point of -30 °C ("Full DP -30 °C").

In the case of DP980, spectral emissivity changes are not significant between "Full DP -30 °C" and "Full DP 0 °C" for wavelengths between 1 and 3 µm.

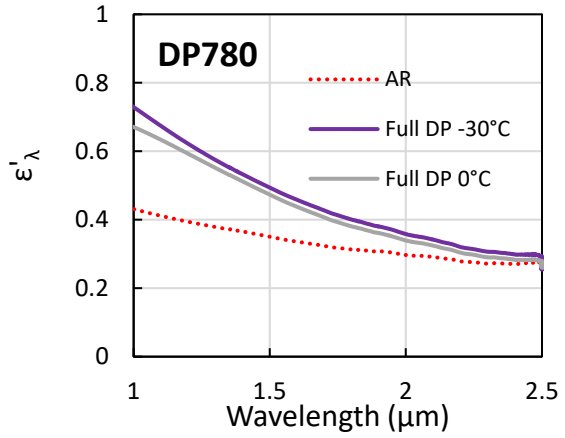

Figure 6-4: Effect of the change in dew point on the spectral emissivity of DP780 between 1 and 2.5 µm

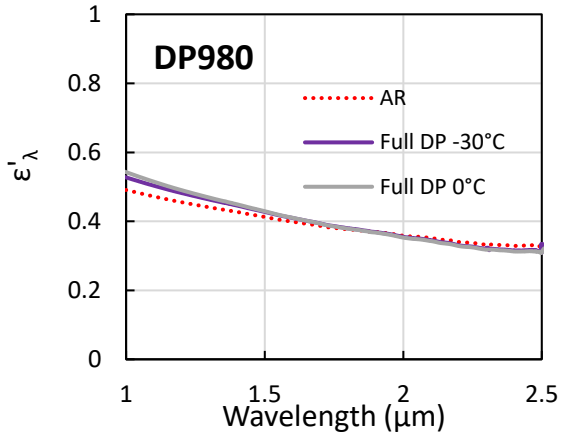

Figure 6-5: Effect of the change in dew point on the spectral emissivity of DP980 between 1 and 2.5 µm

Temperature errors that can be expected during intercritical annealing, based on theoretical calculations, are presented in Figure 6-6 for DP980 (on the left) and for DP780 (on the right). This figure compares errors determined for samples annealed with a dew point of -30 °C (in purple) and with 0 °C (grey). In the case of DP780, temperature errors are lower in absolute value for a dew point of 0 °C. This is due to the fact that the spectral emissivity of samples "Full" annealed with a dew point of 0 °C are closer than samples annealed with a dew point of -30 °C to the spectral emissivity of as-received material.

In the case of DP980, no significant difference in temperature errors is visible with a change in dew point, which reflects the spectral emissivity behavior.

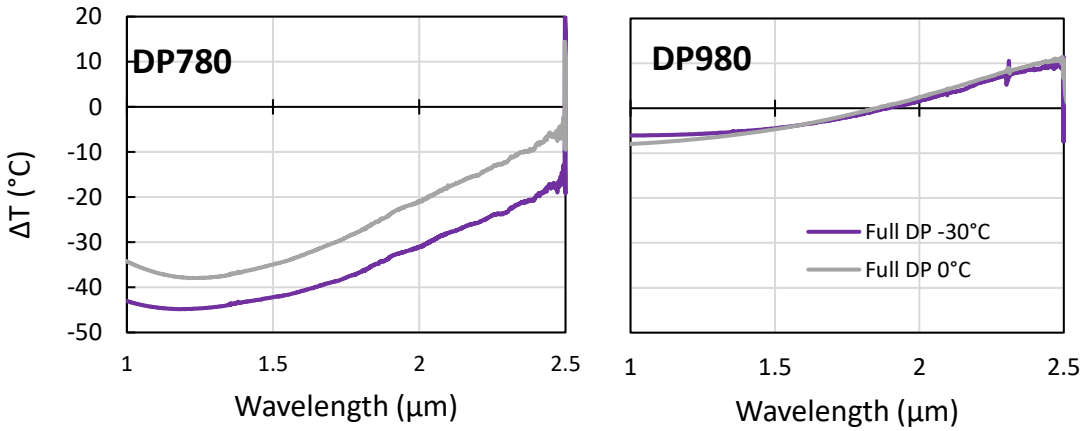

Figure 6-6: Expectable temperature errors for single-wavelength pyrometry when changing the dew point

6.3 Effect of Temperature Inhomogeneity

As explained in section 5.5, it was observed that the coupon temperature was inhomogeneous during intercritical annealing. Consequently, spectral emissivity in Regions (1) and (2) of the coupon, as indicated in Figure 5-20, was different at the end of the annealing cycle. Spectral emissivity of DP780 for wavelengths between 1 and 2.5 µm in as-received condition and in "Full" condition from Regions (1) and (2) is recalled in Figure 6-7.

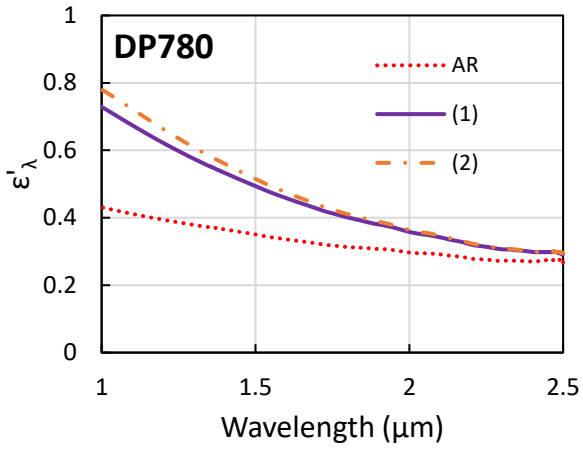

Figure 6-7: Effect of steel temperature inhomogeneity during annealing on the spectral emissivity of DP780 between 1 and 2.5 µm

Temperature deviations that can be expected during intercritical annealing in Regions (1) and (2) is presented in Figure 6-8. Due to a higher spectral emissivity, temperature deviations on the coupon near the thermocouple (Region (2)) that can be expected during annealing are higher in absolute value than in the bottom of the coupon (Region (1)). Difference in temperature deviations between Regions (1) and (2) is below 10 °C in the presented range of wavelengths. This difference is lower than what was observed by Mosser [77], who estimated a temperature difference around 100 °C between Regions (1) and (2) during annealing. Consequently, temperature inhomogeneities due to wedge effects in galvanizing simulator are higher than temperature deviations induced by spectral emissivity differences within the coupon.

Moreover, temperature deviations induced by spectral emissivity variations during intercritical annealing are lower than 50 °C in both regions. If the temperature inhomogeneities estimated by Mosser in the galvanizing simulator are representative of the ones in the industrial CGL, it would mean that steel sheet temperature deviations induced by wedge effect are more significant than temperature deviations induced by spectral emissivity evolutions and would lead to rejection of the sides of the coil due to insufficient mechanical properties [16].

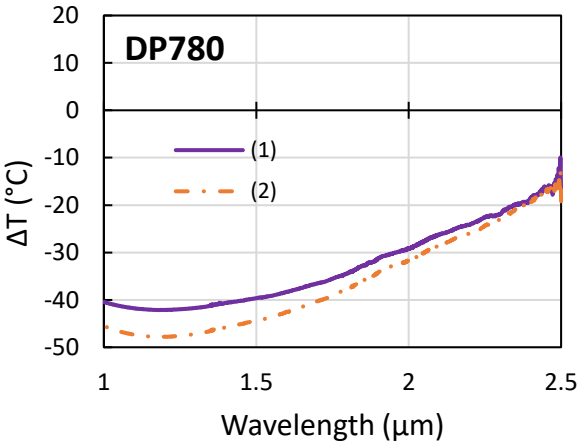

Figure 6-8: Expectable temperature errors in Regions (1) and (2) for single wavelength pyrometry

6.4 Synthesis

Temperature deviations in pyrometry readings induced by spectral emissivity variations during intercritical annealing is around ±45 °C for DP780 and ±10 °C for DP980.

Increasing dew point from -30 °C to 0 °C should decrease temperature errors for DP780 and have little effect on DP980.

The difference of estimated temperature deviations between Regions (1) and (2) of the coupon is lower than the temperature difference induced by edge effect [77].

The spectral emissivity used for pyrometry calculations shown in Figure 6-3, Figure 6-6 and Figure 6-8 was measured at room temperature; since spectral emissivity may also vary with temperature (cf. part 2.3.1), it is possible that temperature deviations presented in Figure 6-3, Figure 6-6 and Figure 6-8 are underestimated.

CHAPTER 7 CONCLUSION AND RECOMMENDATIONS

The impact of selective oxidation on pyrometric temperature measurements during intercritical annealing of dual-phase steels has been presented in this thesis. In this chapter, the main conclusions and a synthesis of the research are presented. Recommendations for future work are also made.

7.1 Conclusions

Results were presented in the article published at the Galvatech 2017, which explained how near-normal spectral emissivity of DP780 and DP980 measured at room temperature evolved after complete and partial intercritical annealing in controlled atmosphere. The article furthermore detailed how this evolution could be explained by selective oxidation. Additional results presented in Chapter 5 and Chapter 6 contributed to addressing the main research objective, which was to ascertain **how selective oxidation during intercritical annealing of DP steels affects temperature measurements acquired by pyrometry**.

In order to reach this objective, the following questions were formulated:

1) How does near-normal spectral emissivity of dual-phase steel evolve during intercritical annealing?
2) How does surface oxidation evolve during annealing?
3) What is the relationship between oxidation state and spectral emissivity?
4) What is the impact of spectral emissivity variation on temperature measurement?

From the presented results, the following conclusions are made:

- **Spectral emissivity measured at room temperature of both DP780 and DP980 increased at short wavelengths (λ<2 µm) during intercritical annealing and decreased at long wavelength (λ>2.5 µm).** Spectral emissivity of DP980 varies less than for DP780 and stabilizes as soon as point “A” is reached during the cycle. Even for the condition “Long”, spectral emissivity is similar to the spectral emissivity of the as-received material. The evolution of spectral emissivity can be related to the transition between different

regimes of interactions between electromagnetic waves and the surface, characterized by optical roughness R_q/λ [57].

- **Oxide thickness increased significantly for DP780 during annealing, while no significant growth was measured for DP980**, according to GDOES results. SEM micrographs revealed that oxide grew on DP780 and DP980 during intercritical annealing.

- **Oxide becomes enriched in manganese and poorer in silicon, an effect even more pronounced when the original surface contains more manganese than silicon**. The oxide morphology is different from one alloy to another: 100 nm diameter nodules for DP780 and plate-like morphology for DP980. The chemical composition of the oxide also differs; surface atomic Mn/Si ratio goes from 2.96 for raw DP780 to 36.0 for DP780 "Full", while the ratio only goes from 1.37 to 4.60 for DP980.The increase in dew point seems to decrease oxide thickening during annealing of DP780. No effect was observed on DP980 oxide thickness and oxide chemical composition. This could be because transition from external to internal oxidation happens at a dew point lower than -30 °C.

- **The spectral emissivity of DP780 evolves monotonically during annealing, similarly to oxide thickness and Mn/Si ratio increase. In the case of DP980, oxide thickness and composition are more stable and spectral emissivity changes little after point "A", even after annealing for 20 min.** This implies a causal relationship between surface oxide growth and changes in oxide chemical composition and spectral emissivity.

- **The change in annealing atmospheric dew point from -30 °C to 0 °C does not significantly affect the spectral emissivity of DP980. However, the change in dew point mitigates the impact of the heat cycle on the spectral emissivity of DP780** since the spectral emissivity of samples annealed with a dew point of 0 °C is closer to that of the raw material than it is to the -30 °C dew point condition. **The increase in dew point seems to decrease oxide thickening during annealing of DP780. No effect was observed on**

DP980 oxide thickness and oxide chemical composition. This could be because transition from external to internal oxidation happens at a dew point lower than -30 °C.

- **The change in spectral emissivity from "AR" to "Full" can induce errors in temperature readings acquired by pyrometry** if spectral emissivity of the raw material is set in the pyrometer. For single-wavelength pyrometry, when the spectral emissivity of the as-received material is set in the pyrometer, **errors can reach ±45 °C for DP780 and ±10 °C for DP980 for wavelengths between 1 and 2.5 µm and a temperature measured at 800 °C**, when the true spectral emissivity of the material is the spectral emissivity for the "Full" condition. When the dew point in the annealing chamber was increased from -30 °C to 0 °C, temperature errors decreased for DP780. In contrast, DP980 was unaffected.

Selective oxidation modifies surface composition and morphology of DP780 and DP980 and alters spectral emissivity. These changes in spectral emissivity induce errors of ±45 °C for DP780 and ±10 °C for DP980 during temperature measurements by SWL pyrometry in the specific studied conditions. These results are similar to the conclusions of the industrial partners (cf. Table 3-1) and may lead to material rejection due to insufficient mechanical properties for DP780 [16]. The different behaviors of DP780 and DP980 can be due to their chemical compositions. In particular, the Mn/Si ratio of DP780 is higher than it is in DP980, leading to a greater oxide enrichment in Mn.

This work constitutes the basis of a model for predicting AHSS spectral emissivity variations during intercritical annealing. This model would enable correction of temperature measurements with pyrometry and consequently improve temperature control during annealing, decreasing rejection rates at the end of the continuous galvanizing line. The next section recommends future studies, which would be pertinent to improve the steel spectral emissivity model.

7.2 Recommendations for Future Work

The literature indicates that spectral emissivity of metals changes with temperature. In the present study, spectral emissivity was measured in the Gleeble following a heating curve representative of industrial intercritical annealing treatments. However, it was shown that samples heated in the Gleeble oxidized in a different manner than they did in the galvanizing simulator due to inadequate atmosphere control. It would be pertinent to find a way to measure spectral emissivity in-situ to confirm the trends measured at room temperature. Construction of a new annealing chamber with an access window would enable measurement of the spectral emissivity of the annealed sample and could afford the benefits of heating and cooling systems and better atmosphere control than exists in the Gleeble.

The literature also indicates that surface roughness has an impact on spectral emissivity. Atomic force microscopy (AFM) was able to capture the topography changes induced by oxidation, owing to the excellent vertical and horizontal resolution of AFM. It would be pertinent to carry on roughness measurement with AFM to see if trends can be observed. Moreover, Ham et al. [61] also showed that it was possible to correlate increase in spectral emissivity of AHSS at long wavelengths (8-12 µm) with roughness measured with white interferometry. They applied mathematical filters on the results to suppress the effect of the topography created by rolling processes on steel and obtained the signature of surface oxide only. Consequently, more work with light interferometry could be pertinent to improve the spectral emissivity model.

Oxide growth is another phenomenon that affects AHSS spectral emissivity. Oxide thickness was measured qualitatively with GDOES. It could be possible to cut cross-sections of samples with focused ion beams and characterize them with transmission electron microscopy in order to measure oxide thickness quantitatively for both materials and for the different conditions and relate it with spectral emissivity. It would also enable observation of possible internal oxidation.

The spectral emissivity of DP980 was shown to be less sensitive to annealing than that of DP780. The hypotheses proposed were that the transition from external to internal oxidation happened at a dew point lower than -30 °C, or that DP980 is intrinsically less sensitive to oxidation than is DP780, due to its chemical composition (especially its Mn/Si ratio). It would then be appropriate to anneal DP980 with a lower dew point than -30 °C (for instance -50 °C or -60 °C), in order to find the

suspected external-internal oxidation transition and observe whether spectral emissivity and oxidation states remain as unchanged during the cycle as they are with a dew point of -30 °C. Understanding how the steel chemical composition influences the transition dew point from external to internal oxidation could help designing steel more resistant to external selective oxidation.

BIBLIOGRAPHY

[1] S. Keeler, M. Kimchi, and P. J. Mconey. (2017). *Advanced High-Strength Steels Application Guidelines Version 6.0*. Available: http://www.worldautosteel.org/projects/advanced-high-strength-steel-application-guidelines/

[2] ULSAB-AVC Consortium. (2001). *Technical Transfer Dispatch #6*. Available: http://www.autosteel.org/~/media/Files/Autosteel/Programs/ULSAB-AVC/avc_ttd6.pdf

[3] K. Daun, "Illustration of wedge method pyrometry," ed, 2017.

[4] X. Che and Z. Xie, "Development of ReFaST pyrometer for measuring surface temperature with unknown emissivity: methodology, implementation, and validation," *IEEE Transactions on Instrumentation and Measurement,* vol. 66, pp. 1845-1855, 2017.

[5] R. Usamentiaga, D. F. Garcia, J. Molleda, F. G. Bulnes, and J. M. Perez, "Temperature measurement using the wedge method: comparison and application to emissivity estimation and compensation," *IEEE Transactions on Instrumentation and Measurement,* vol. 60, pp. 1768-1778, 2011.

[6] International Zinc Association. *The Galvanized Autobody Partnership*. Available: http://www.zinc.org/galvanized-autobody-partnership/

[7] International Zinc Association. *About IZA*. Available: http://www.zinc.org/about/

[8] F. Cabannes, "Pyrométrie optique," 1990.

[9] R. Usamentiaga, P. Venegas, J. Guerediaga, L. Vega, J. Molleda, and F. G. Bulnes, "Infrared thermography for temperature measurement and non-destructive testing," *Sensors,* vol. 14, pp. 12305-12348, 2014.

[10] R. G. Thiessen, E. Bocharova, D. Mattissen, and R. Sebald, "Temperature measurement deviation during annealing of multiphase steels," *Metallurgical and Materials Transactions B,* vol. 41, pp. 857-863, 2010.

[11] P. B. Coates, "Multi-wavelength pyrometry," *Metrologia,* vol. 17, pp. 103-109, 1981.

[12] A. Araùjo, "Multi-spectral pyrometry - a review," *Measurement Science and Technology,* vol. 28, 2017.

[13] C.-D. Wen, "Investigation of steel emissivity behaviors: examination of multispectral radiation thermometry (MRT) emissivity models," *International Journal of Heat and Mass Transfer,* vol. 53, pp. 2035-2043, 2010.

[14] J. Xing, S. Cui, W. Qi, F. Zhang, X. Sun, and W. Sun, "A data processing algorithm for multi-wavelength pyrometry-which does not need to assume the emissivity model in advance," *Measurement,* vol. 67, pp. 92-98, 2015.

[15] V. L. de la Concepción, H. N. Lorusso, and H. G. Svoboda, "Effect of carbon content on microstructure and mechanical properties of dual phase steels," *Procedia Materials Science,* vol. 8, pp. 1047-1056, 2015.

[16] P. Mosser, Q. Somveille, K. Daun, and M. Brochu, "Effect of temperature deviation during intercritical annealing of HSLA and DP980 steels," in *Galvatech 2017*, Tokyo, Japan, 2017, pp. 218-225.

[17] ASTM, "A1079 - Standard specification for steel sheet, complex phase (CP), dual phase (DP) and transformation induced plasticity (TRIP), zinc-coated (galvanized) or zinc-iron alloy-coated (galvannealed) by the hot-dip process," ed, 2017.

[18] D. Huin, P. Flauder, and J. B. Leblond, "Numerical simulation of internal oxidation of steels during annealing treatments," *Oxidation of Metals,* vol. 64, pp. 131-167, 2005.

[19] E. Buscarlet, "Galvanisation et aluminage en continu," *Techniques de l'Ingénieur,* 1996.
[20] X. Vanden Eynde, J. P. Servais, and M. Lamberigts, "Investigation into the surface selective oxidation of dual-phase steels by XPS, SAM and SIMS," *Surface and Interface Analysis,* vol. 35, pp. 1004-1014, 2003.
[21] C. R. Shastry, J. A. Rotole, and T. W. Kaiser, "Characterization of selective oxidation of alloying elements in an advanced high stregth steel from theoretical and experimental viewpoints," in *Galvatech 07*, Osaka, Japan, 2007, pp. 403-408.
[22] L. Cho, M. S. Kim, Y. H. Kim, and B. C. De Cooman, "Influence of minor alloying elements on selective oxidation and reactive wetting of CMnSi TRIP steel during hot dip galvanizing," *Metallurgical and Materials Transactions A,* vol. 45, pp. 4484-4498, 2014.
[23] I. Cvijovic, M. Spiegel, and I. Parezanovic, "The effect of dual phase steel surface roughness on selective oxidation and surface wettability," *Kovove Mater,* vol. 44, pp. 35-39, 2006.
[24] L. Cho, G. S. Jung, and B. C. De Cooman, "On the transition of internal to external selective oxidation on CMnSi TRIP steel," *Metallurgical and Materials Transactions A,* vol. 45, pp. 5158-5172, 2014.
[25] J. Mahieu, S. Claessens, B. De Cooman, F. Goodwin, and J. Kennedylaan, "Surface and sub-surface characterization of Si-, Al-and P-alloyed TRIP-aided steel," in *Galvatech 04*, Chicago, USA, 2004, pp. 529-538.
[26] I. Cvijović, I. Parezanović, and M. Spiegel, "Influence of H2–N2 atmosphere composition and annealing duration on the selective surface oxidation of low-carbon steels," *Corrosion Science,* vol. 48, pp. 980-993, 2006.
[27] H. Liu, F. Li, W. Shi, S. Swaminathan, Y. He, M. Rohwerder, *et al.*, "Challenges in hot-dip galvanizing of high strength dual phase steel: Surface selective oxidation and mechanical property degradation," *Surface and Coatings Technology,* vol. 206, pp. 3428-3436, 2012.
[28] T. Van De Putte, D. Loison, S. Claessens, Z. Zermout, and P. J., "Surface analysis of the selective oxidation during austenitic annealing of CMnSi High strength steel," in *Galvatech 07*, Osaka, Japan, 2007, pp. 415-420.
[29] Y. Suzuki, T. Yamashita, Y. Sugimoto, S. Fujita, and S. Yamaguchi, "Thermodynamic analysis of selective oxidation behavior of Si and Mn-added steel during recrystallization annealing," *ISIJ International,* vol. 96, pp. 11-20, 2010.
[30] I.-R. Sohn, J.-S. Kim, and S. Sridhar, "Effect of dew point and gas flow rate on the surface oxidation of advanced high strength steels," *ISIJ International,* vol. 55, pp. 2008-2017, 2015.
[31] G. Seyed Mousavi and J. McDermid, "Effect of annealing parameters on selective oxidation and reactive wetting of CMnSi Advanced high strength steel," in *Galvatech 2017*, Tokyo, Japan, 2017, pp. 485-492.
[32] J. Staudte, J. M. Mataigne, F. Del Frate, D. Loison, and S. Cremel, "Optimizing the manganese and silicon content for hot dip galvanizing of 3rd generation advanced high strength steels," *Metallurgical Research & Technology,* vol. 111, pp. 17-23, 2014.
[33] A. P. Grosvenor, E. M. Bellhouse, A. Korinek, M. Bugnet, and J. R. McDermid, "XPS and EELS characterization of Mn2SiO4, MnSiO3 and MnAl2O4," *Applied Surface Science,* vol. 379, pp. 242-248, 2016.

[34] M. Pourmajidian and J. McDermid, "The effect of annealing temperature on the selective oxidation of a 0.1C-6Mn-2Si advanced high strength steel during continuous galvanizing heat treatments," in *Galvatech 2017*, Tokyo, Japan, 2017.

[35] F. Menguelti, X. Vanden Eynde, and L. Bordignon, "Effect of annealing parameters on strip surface state of high strength steels and consequences on zinc wetting," in *Galvatech 2011*, Genova, Italy, 2011.

[36] H. Saint-Raymond, F. Bertrand, and D. Huin, "Kinetics of oxidation and reduction of high strength steels in annealing furnaces," in *Galvatech 04*, Chicago, USA, 2004, pp. 383-390.

[37] S. Swaminathan, "Selective surface oxidation and segragation upon short term annealing of model alloys and industrial steel grades," Ph.D, Fakultät für Physik und Astronomie, Ruhr-Universität Bochum, 2007.

[38] C. Wagner, "Reaktionstypen bei der Oxydation von Legierungen," *Berichte der Bunsengesellschaft für physikalische Chemie*, vol. 63, pp. 772-782, 1959.

[39] M. Norden, M. Blumenau, R. Schönenberg, and K.-J. Peters, "Chances and challenges of using preoxidation in hot dip galvanizing of AHSS," in *Galvatech 2011*, Genova, Italy, 2011.

[40] M. Blumenau, C. O. Gusek, M. Norden, and R. Schönenberg, "Industrial use of pre-oxidation during continuous hot-dip coating of (high) alloyed steels," in *Proc., AISTech 2012 Conference, Atlanta, USA*, 2012, pp. 7-10.

[41] R. Khondker, A. Mertens, and J. R. McDermid, "Effect of annealing atmosphere on the galvanizing behavior of a dual-phase steel," *Materials Science and Engineering: A*, vol. 463, pp. 157-165, 2007.

[42] R. Sagl, A. Jarosik, D. Stifter, and G. Angeli, "The role of surface oxides on annealed high-strength steels in hot-dip galvanizing," *Corrosion Science*, vol. 70, pp. 268-275, 2013.

[43] L. Cho, S. Lee, B. C. De Cooman, M. S. Kim, and Y. H. Kim, "Observation of the transition of external to internal oxidation due to dew point control," in *Galvatech 2011*, Genova, Italy, 2011.

[44] M. Maderthaner, A. Jarosik, G. Angeli, and R. Haubner, "Effect of dew point on the selective oxidation of advanced high strength steels," *Materials Science Forum*, vol. 891, pp. 292-297, 2017.

[45] J. R. Howell, M. P. Menguc, and R. Siegel, *Thermal Radiation Heat Transfer*, Sixth ed.: CRC press, 2015.

[46] A. Seifter, "About the meaning of the Hagen-Rubens relation to radiation thermometry," 2003.

[47] L. del Campo, R. B. Pérez-Sáez, L. González-Fernández, X. Esquisabel, I. Fernández, P. González-Martín, *et al.*, "Emissivity measurements on aeronautical alloys," *Journal of Alloys and Compounds*, vol. 489, pp. 482-487, 2010.

[48] K.-H. Weng and C.-D. Wen, "Effect of oxidation on aluminum alloys temperature prediction using multispectral radiation thermometry," *International Journal of Heat and Mass Transfer*, vol. 54, pp. 4834-4843, 2011.

[49] G. Zauner, F. Mayrhofer, and G. Hendorfer, "Optical characterization of growing thin films at high temperatures by analysis of near infrared emissivity variations using CCD thermal imaging," in *QIRT 10*, Québec, Canada, 2010.

[50] L. del Campo, R. B. Pérez-Sáez, and M. J. Tello, "Iron oxidation kinetics study by using infrared spectral emissivity measurements below 570°C," *Corrosion Science,* vol. 50, pp. 194-199, 2008.
[51] B. Roebuck, G. Edwards, and M. G. Gee, "Characterisation of oxidising metal surfaces with a two colour pyrometer," *Materials Science and Technology,* vol. 21, pp. 831-840, 2013.
[52] D. Shi, F. Zou, S. Wang, Z. Zhu, J. Sun, and B. Wang, "Spectral emissivity modeling of steel 201 during the growth of oxidation film over the temperature range from 800 to 1100 K in air," *Infrared Physics & Technology,* vol. 67, pp. 42-48, 2014.
[53] D. Shi, F. Zou, S. Wang, Z. Zhu, and J. Sun, "Effect of surface oxidization on the spectral emissivity of steel 304 at the elevated temperature in air," *Infrared Physics & Technology,* vol. 66, pp. 6-12, Sep 2014.
[54] D. Shi, F. Zou, Z. Zhu, and J. Sun, "Effect of surface oxidization on the normal spectral emissivity of straight carbon steel at 800–1100 K in air," *ISIJ International,* vol. 55, pp. 697-705, 2015.
[55] S. H. Ham, M. Ferté, G. Fricout, L. Depalo, and C. Carteret, "In-situ spectral emissivity measurement of alloy steels during annealing in controlled atmosphere," in *QIRT 2016*, Gdansk, Poland, 2016, pp. 315-321.
[56] C. Shi, K. J. Daun, and M. A. Wells, "Spectral emissivity characteristics of the Usibor® 1500P steel during austenitization in argon and air atmospheres," *International Journal of Heat and Mass Transfer,* vol. 91, pp. 818-828, 2015.
[57] C. D. Wen and I. Mudawar, "Modeling the effects of surface roughness on the emissivity of aluminum alloys," *International Journal of Heat and Mass Transfer,* vol. 49, pp. 4279-4289, Nov 2006.
[58] S. G. Agababov, "Effect of roughness factor on the radiation properties of a solid body with random roughness," *Teplofizika Vysokikh Temperatur,* vol. 13, pp. 314-317, 1975.
[59] S. G. Agababov, "Effect of the roughness factor on radiation properties of solids (experimental check)," *Teplofizika Vysokikh Temperatur,* vol. 8, pp. 770-773, 1970.
[60] S. G. Agababov, "Influence of the geometric characteristics of the relief of the surface of a solid on its radiation properties (determination of the roughness factor)," *Teplofizika Vysokikh Temperatur,* vol. 9, pp. 522-526, 1971.
[61] S. H. Ham, C. Carteret, J. Angulo, and G. Fricout, "Relation between emissivity evolution during annealing and selective oxidation of TRIP steel," *Corrosion Science,* vol. 132, pp. 185-193, 2018.
[62] K. Yu, F. Zhang, D. Liu, and Y. Liu, "Spectral emissivity of type E235B low carbon structural steel with different roughnesses," *Optical Review,* vol. 24, pp. 540-548, 2017.
[63] B. Bhushan, *Introduction to Tribology*: Wiley, 2013.
[64] Q. Somveille, P. Mosser, M. Brochu, and K. Daun, "Effect of oxidation on emissivity for DP780 and DP980 steels," in *Galvatech 2017*, Tokyo, Japan, 2017, pp. 210-217.
[65] ASTM, "E415-14 - Standard Test Method for Analysis of Carbon and Low-Alloy Steel by Spark Atomic Emission Spectrometry," ed, 2014.
[66] L. Chen, R. Fourmentin, and J. R. Mc Dermid, "Morphology and kinetics of interfacial layer formation during continuous hot-dip galvanizing and galvannealing," *Metallurgical and Materials Transactions a-Physical Metallurgy and Materials Science,* vol. 39A, pp. 2128-2142, Sep 2008.

[67] M. F. Modest, *Radiative Heat Transfer*, Third ed.: Academic press, 2013.
[68] ISO, "4287 - Geometrical Product Specifications (GPS) - Surface texture : profile method - Terms, definitions and surface texture parameters," ed, 1997.
[69] H. Liu, Y. He, and L. Li, "Application of thermodynamics and Wagner model on two problems in continuous hot-dip galvanizing," *Applied Surface Science,* vol. 256, pp. 1399-1403, 2009.
[70] Keyence. (2017/02/28). *Instrument de mesure à contact de la rugosité de surface/du profil*. Available: https://www.keyence.eu/frfr/ss/products/microscope/roughness/equipment/surface_01.jsp
[71] T. Iuchi, T. Furukawa, and S. Wada, "Emissivity modeling of metals during the growth of oxide film and comparison of the model with experimental results," *Applied Optics,* vol. 42, p. 2317, 2003.
[72] W. H. Sun, A. K. Tieu, Z. Y. Jiang, H. T. Zhu, and C. Lu, "Oxide scales growth of low-carbon steel at high temperatures," *Journal of Materials Processing Technology,* vol. 155, pp. 1300-1306, Nov 30 2004.
[73] R. M. Bradley and J. M. E. Harper, "Theory of ripple topography induced by ion bombardment," *Journal of Vacuum Science & Technology A: Vacuum, Surfaces, and Films,* vol. 6, pp. 2390-2395, 1988.
[74] M. A. Makeev, R. Cuerno, and A.-L. Barabási, "Morphology of ion-sputtered surfaces," *Nuclear Instruments and Methods in Physics Research Section B: Beam Interactions with Materials and Atoms,* vol. 197, pp. 185-227, 2002.
[75] J. Pan, C. Leygraf, R. F. A. Jargelius-Pettersson, and J. Linden, *Oxidation of Metals,* vol. 50, pp. 431-455, 1998.
[76] Praxair. *Compressed Argon Gas Specifications Sheet*. Available: http://www.praxair.com/-/media/documents/specification-sheets-and-brochures/gases/argon/argon-ar-spec-sheet-ss-p4563.pdf?la=en
[77] P. Mosser, "Caractérisation microstructurale et mécanique d'aciers à haute résistance sujet à la galvanisation continue," Département de Génie Mécanique, Polytechnique Montréal, 2018.

APPENDIX A – THERMAL RADIATION BASICS

All materials emit thermal radiation. The power radiated by a surface is often described by the total hemispherical emissive power $E(T)$, a function of both material and temperature. The quantity $E(T)$ quantifies the power radiated by a surface per unit surface area (W/m^2). The power radiated per unit surface area per unit wavelength and per unit solid angle is the spectral directional emissive power, denoted E'_λ. The subscript λ denotes that the quantity is per unit wavelength and the prime symbol ($'$) indicates that the quantity is per unit solid angle. The quantity E'_λ is a function of material, temperature, wavelength and direction.

Using E'_λ for calculations requires knowledge of the orientation of the radiating surface relative to the observation direction. A typical way to resolve this issue is to quantify the radiated power by calculating spectral directional intensity I'_λ. The quantity I'_λ quantifies the power radiated per unit projected surface area, rather than per unit surface area.

If the material properties are isotropic, intensity is independent of direction. Figure illustrates the distribution of intensity and emissive power over polar angle θ.

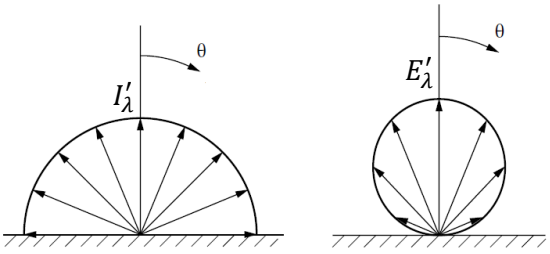

Figure A-1: Angular distribution of intensity and emissive power for a diffuse material [45]

In the case of isotropic materials, intensity is constant while emissive power follows a cosine Lambertian law,

$$E'_\lambda = I'_\lambda \cos\theta \tag{A-1}$$

Materials exhibiting isotropic optical properties and that respect Eq. (A-1) are called “diffuse” or “Lambertian”.

Blackbodies

The blackbody is an ideal body in terms of thermal radiation and is used as a reference for real surfaces. Its three main characteristics are as follow:

- A blackbody absorbs all incident radiation.
- A blackbody is diffuse; its optical properties are isotropic.
- A blackbody possesses a radiation maximum at a certain temperature and wavelength.

For blackbodies, hemispherical spectral emissive power ($E_{b\lambda}$) and directional spectral radiative intensity ($I'_{b\lambda}$) are given by Planck's law,

$$E_{b\lambda}(\lambda,T) = \pi\, I'_{b\lambda}(\lambda,T) = \frac{2\,\pi\,h\,c_0^2}{\lambda^5\left(\exp\left(\frac{h\,c_0}{k_B\,\lambda\,T}\right)-1\right)} = \frac{\pi\,C_1}{\lambda^5\left(\exp\left(\frac{C_2}{\lambda\,T}\right)-1\right)} \qquad \text{(A-2)}$$

where h is Planck's constant (6.626×10^{-34} J·s), c_0 is the speed of light in vacuum (2.998×10^{8} m/s), k_B is Boltzmann's constant (1.381×10^{-23} J/K), and where C_1 and C_2 are the constants $C_1 = 2\,h\,c_0^2 = 1.191\times10^{-16}$ W·m^2/sr and $C_2 = h\,c/k_B = 1.439\times10^{-2}$ m·K.

For low enough values of $\lambda\,T$, Wien's approximation applies $\exp\left(\frac{C_2}{\lambda\,T}\right) \gg 1$; thus, $\exp\left(\frac{C_2}{\lambda\,T}\right) - 1 \approx \exp\left(\frac{C_2}{\lambda\,T}\right)$ in Planck's law (Eq. (A-2)) . A simplified form of $E'_{b\lambda}$ and $I'_{b\lambda}$ results,

$$E_{b\lambda} = \pi\, I'_{b\lambda}(\lambda,T) \approx \frac{\pi\,C_1}{\lambda^5 \exp\left(\frac{C_2}{\lambda\,T}\right)} \qquad \text{(A-3)}$$

Figure illustrates emissive power of a blackbody as a function of wavelength for several temperatures. The visible part of the wavelength spectrum (between 400 and 700 nm) is highlighted in light grey. For 3000 K and 2000 K, spectral emissive power is greater for the higher wavelengths of the visible spectrum, corresponding to the colors red and orange. This explains why heated materials appear red, then orange to the naked eye as they heat. Also, for 5777 K, which is the temperature of the surface of the sun, emissive power is greatest for a wavelength around 500 nm

(green). However, the value of emissive power is quasi-constant on the range of visible wavelengths, which is why the sun looks white to the naked eye, rather than appearing green.

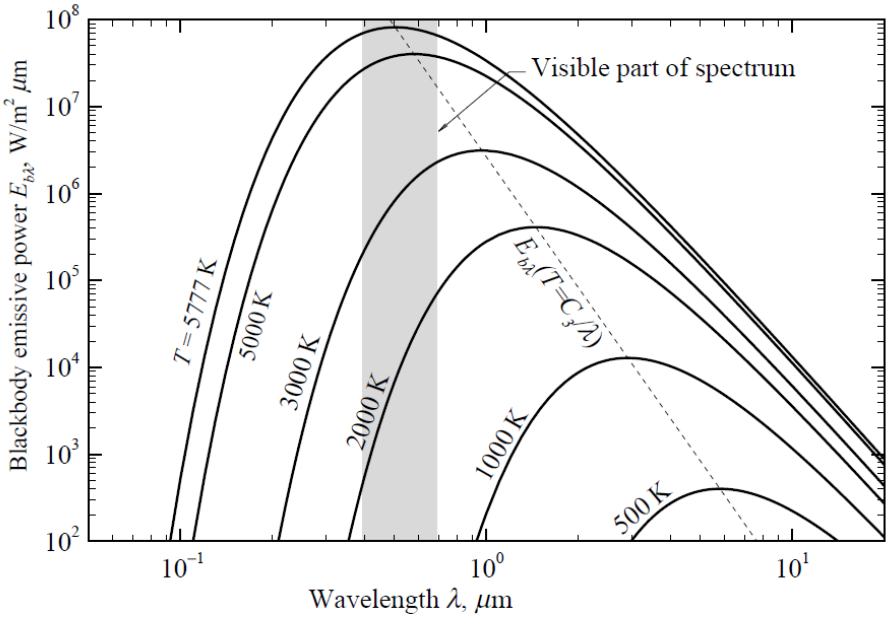

Figure A-2: Blackbody emissive power spectrum [67]

Figure also shows that spectral emissive power possesses a maximum then decreases with along the wavelength domain. The wavelength at which this maximum is attained decreases as temperature increases. It is possible to calculate the values of temperature and wavelength that maximize emissive power by dividing emissive power by T^5, yielding a function f of λT:

$$\frac{E_{b\lambda}}{T^5} = \frac{\pi\, C_1}{(\lambda T)^5 \left(\exp\left(\frac{C_2}{\lambda T}\right) - 1\right)} = f(\lambda T) \tag{A-4}$$

Then, differentiation of f implies that

$$\frac{\partial f}{\partial\, \lambda T} = 0 \;\Leftrightarrow (\lambda T)_{max} = C_3 = 2898\ \mu\text{m} \cdot \text{K} \tag{A-5}$$

where C_3 is a constant (C_3=2898 µm·K). This relation is called Wien's displacement law.

The capacity of a real body to emit thermal radiation is expressed by its emissivity. Emissivity compares the intensity of the real body with the intensity of the blackbody. The most basic form of emissivity is the directional spectral emissivity (ε'_λ), which is the ratio between the directional spectral intensity of a real body and the corresponding quantity for a blackbody.

$$\varepsilon'_\lambda(T,\lambda,\theta,\phi) = \frac{I'_\lambda(T,\lambda,\theta,\phi)}{I'_{b\lambda}(T,\lambda)} \tag{A-6}$$

Bodies possessing directional spectral emissivity independent of wavelength are called greybodies.

Optical Properties of Real Bodies

As schematized in Figure , when a surface is illuminated by radiation, energy is either reflected, absorbed or transmitted.

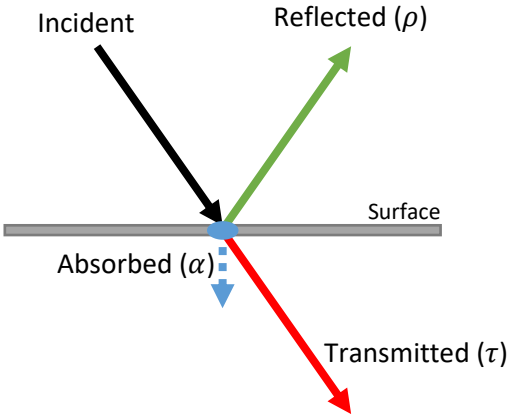

Figure A-3: Absorbed, reflected, and transmitted light

Reflectivity (ρ), absorptivity (α) and transmissivity (τ) are defined as the respective proportions of reflected energy, absorbed energy, and transmitted energy, relative to the incident energy.

The sum of the reflected, absorbed and transmitted energies equal the incident energy, meaning that

$$\rho + \alpha + \tau = 1 \tag{A-7}$$

This study focuses on opaque materials. Therefore, it will be assumed that none of the incident energy is transmitted through the material and that consequently $\tau = 0$. It follows that all the radiation is either reflected or absorbed, and Eq. (A-7) can be modified into

$$\rho + \alpha = 1 \tag{A-8}$$

Reflectivity and absorptivity can also be studied in terms of spectral and directional quantities. Directional spectral absorptivity (α'_λ) expresses the ratio between absorbed energy and incident energy at one wavelength, for one incident direction (θ, ϕ).

In the case of reflectivity, the direction of incident radiation (θ_i, ϕ_i) and the direction of reflected radiation (θ_r, ϕ_r) must be distinguished. On the one hand, directional-hemispherical spectral reflectivity ($\rho'_{\lambda-d/h}$) is defined as the ratio, at one wavelength, between the energy reflected in all directions and the incident energy from one direction (θ_i, ϕ_i). On the other hand, hemispherical-directional spectral emissivity ($\rho'_{\lambda-h/d}$) is defined as the ratio, at one wavelength, between the energy reflected in one direction (θ_r, ϕ_r) and the incident energy coming from all directions.

Then, if incident radiation is uniform over all directions, $\theta_i = \theta_r$ and $\phi_i = \phi_r$, these quantities can be united into directional spectral reflectivity (ρ'_λ) through the Law of Reciprocity, as

$$\rho'_\lambda(\theta_\rho = \theta_i, \phi_\rho = \phi_i) = \rho'_{\lambda-d/h} = \rho'_{\lambda-h/d} \tag{A-9}$$

Eq. (A-8) can be extended to directional spectral quantities as

$$\rho'_\lambda + \alpha'_\lambda = 1 \tag{A-10}$$

According to Kirchhoff's Law, directional spectral emissivity is equal to directional spectral absorptivity in case of thermodynamic equilibrium:

$$\varepsilon'_\lambda = \alpha'_\lambda \tag{A-11}$$

Then, the relationship between emissivity and reflectivity can be expressed as

$$\varepsilon'_\lambda = 1 - \rho'_\lambda \tag{A-12}$$

Saliently, since the thermal radiation of materials depends on temperature, it is possible to estimate the temperature of a component by measuring its radiative intensity via pyrometry.

APPENDIX B – QUESTIONNAIRE SENT TO THE INDUSTRIAL PARTNERS

ZCO-72 GAP PROJECT

Survey for industrial partners on pyrometry in the CGL strip pretreatment furnace

Please it would be appreciated and very helpful for our laboratory research, if you fill out the survey below, by skipping questions that might be of a confidential nature to the company. When the question is confidential, please check the case "Cfdl" in the last column. For each question, if you have comments to add, fill the blank just below the question. All non-confidential results will be combined with those of other companies when reporting the results so that the identity of any responding company cannot be determined. Always indicate if temperatures and temperature error ranges are °C or °F.

Abbreviation's list:

SWL= single wavelength pyrometer *DP= Dual Phase* *Cfdl= Confidential*

DWL= Dual wavelength pyrometer *MWL= Multi-wavelength pyrometer*

CGL= Hot-dip Continuous galvanizing lines

1.	**What grades of DP steels do you process on your CGL?**			Cfdl ☐
2.	**What is the peak annealing temperature range for Dual Phase steels on these lines?**	Min_____	Max_____	Cfdl ☐
3.	**What are the estimated temperature errors (measured vs. expected actual strip T) in your annealing section?**	Min_____	Max_____	Cfdl ☐
4.	**Is there a pre-oxidizing section in your CGL?**	YES ☐	NO ☐	Cfdl ☐
5.	**Which type of sensor do you use for temperature measurement at the exit of the soaking section before jet cooling?**	SWL ☐ DWL ☐ MWL ☐		Cfdl ☐

6. Which Model of sensor? Cfdl ☐

7. If pyrometry is used, what is the spectral range (wavelength λ in μm)? Min_____ Max_____ Cfdl ☐

8. a) Do you use the wedge configuration for your pyrometer measurements at the exit of the soaking section? YES ☐ NO ☐ Cfdl ☐

b) If yes, how do you aim (align) your pyrometer to be sure it it aimed at the deepest part of the wedge? Cfdl ☐

c) Do you apply temperature corrections when transitioning from one coil type/gauge/width to a significantly different one? YES ☐ NO ☐ Cfdl ☐

9. Do you adjust the emissivity measured by the pyrometer from one grade of steel to another? YES ☐ NO ☐ Cfdl ☐

10. Do you adjust the emissivity depending upon surface finish, sheet thickness, surface treatment, waviness etc. ? YES ☐ NO ☐ Cfdl ☐

If yes, please give more details:

APPENDIX C – RESULTS OF THE SURVEY

	A	B	C	D	E	F
1)	-	DP500-DP1000	DP1200	DP590, DP780, DP980	It is possible to run all mix products	DP590, DP980, DP1180
2)	-	760-840°C	750-850°C	760-815°C	780-830°C	750-830°C
3)	-	10-40°C	5-20°C	5°C	10°C	5°C
4)	-	Yes	Yes	No	No	Yes
5)	SWL	SWL	SWL	SWL	SWL	SWL
6)	LAND with Si sensor	Keller MSR CellaTemp® PZ 20	Infrared	LAND	LAND-AMETEK M2 300/1100C-V (S4)	-
7)	1.0 µm	1.1-1.7 µm	1.0-3.0 µm	1.5 µm	1.6 µm	1.0-2.6 µm
8)a)	Yes	No	Yes	Yes	No	Yes
8)b)	Laser pointing	-	Sighting position adjustment	Aiming port	-	Cold alignment, sighting eyepiece
8)c)	No	No	No	No	No	No
9)	No	No	No	No	No	No
10)	No	No	No	No	No	No

The symbol "-" means that no answer was provided or that the question does not apply.

APPENDIX D – GDOES PROFILES

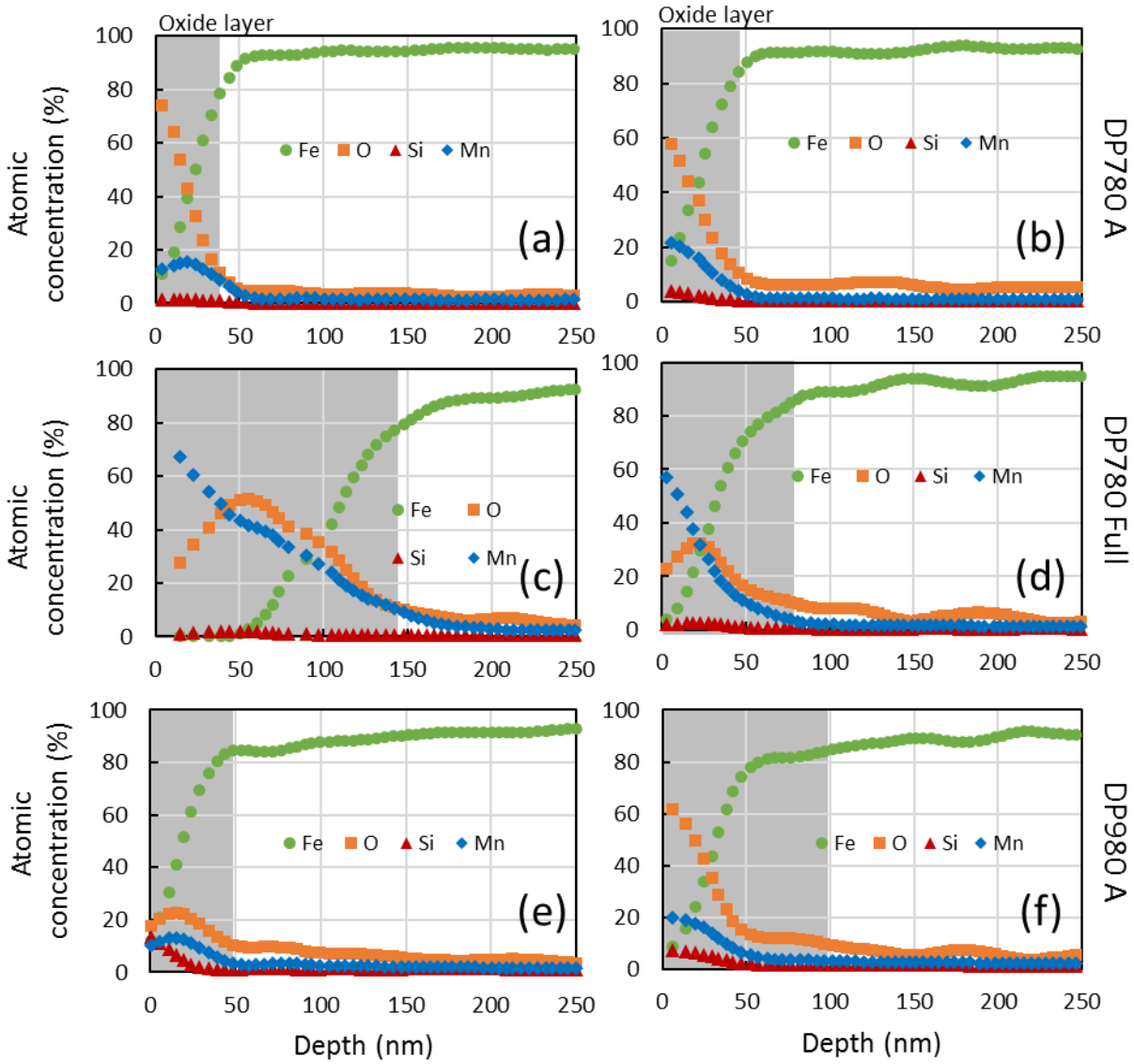

Figure D-1: Surface elemental profiles obtained with GDOES ((a) and (b): DP780 “A”; (c) and (d): DP780 “Full”; (e) and (f): DP980 “A”)

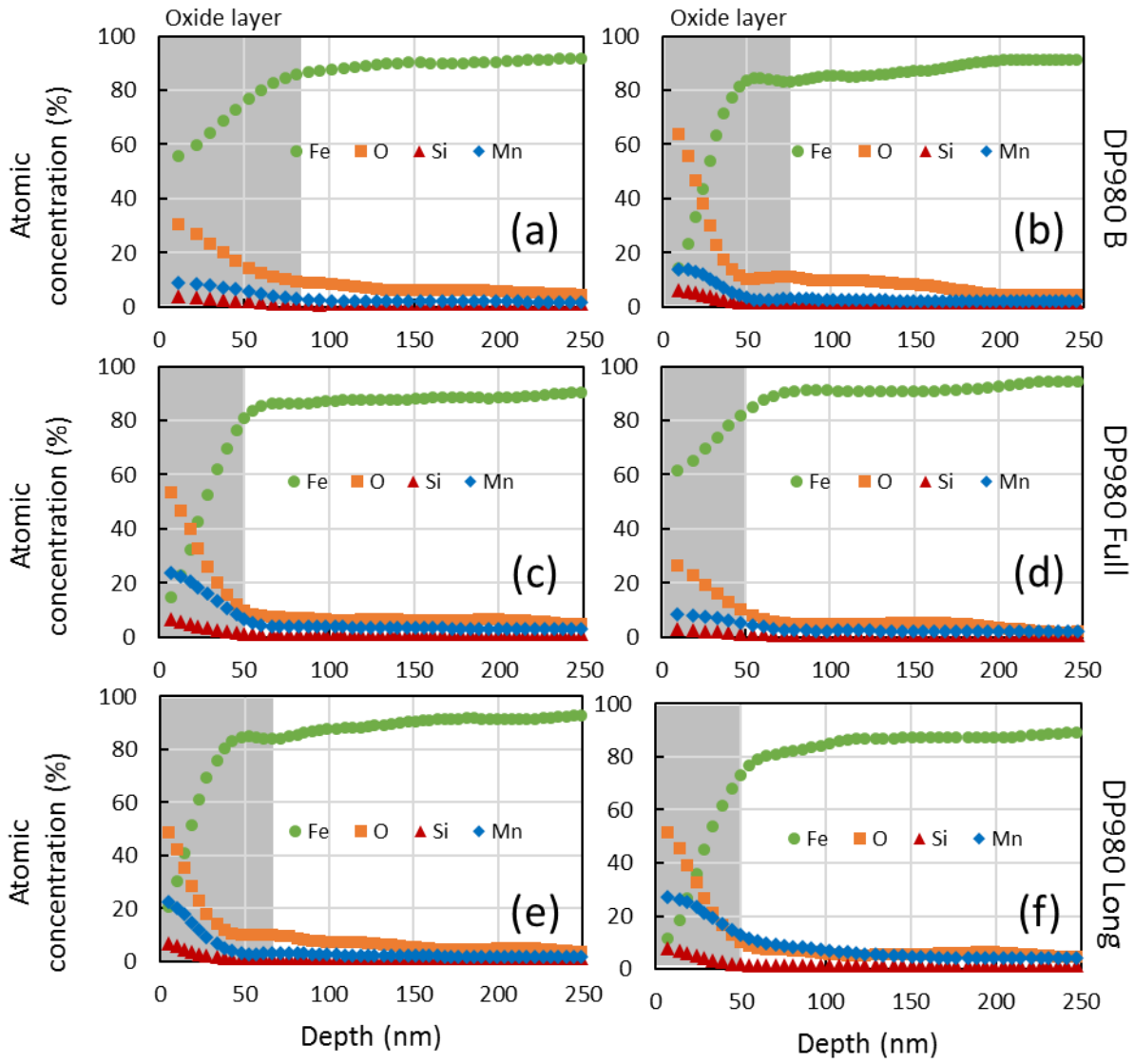

Figure D-2: Surface elemental profiles obtained with GDOES ((a) and (b): DP980 "B"; (c) and (d): DP780 "Full"; (e) and (f): DP780 "Long")

APPENDIX E – ILLUSTRATION OF THREE REGIMES OF INTERACTIONS BETWEEN SPECTRAL EMISSIVITY AND ROUGHNESS

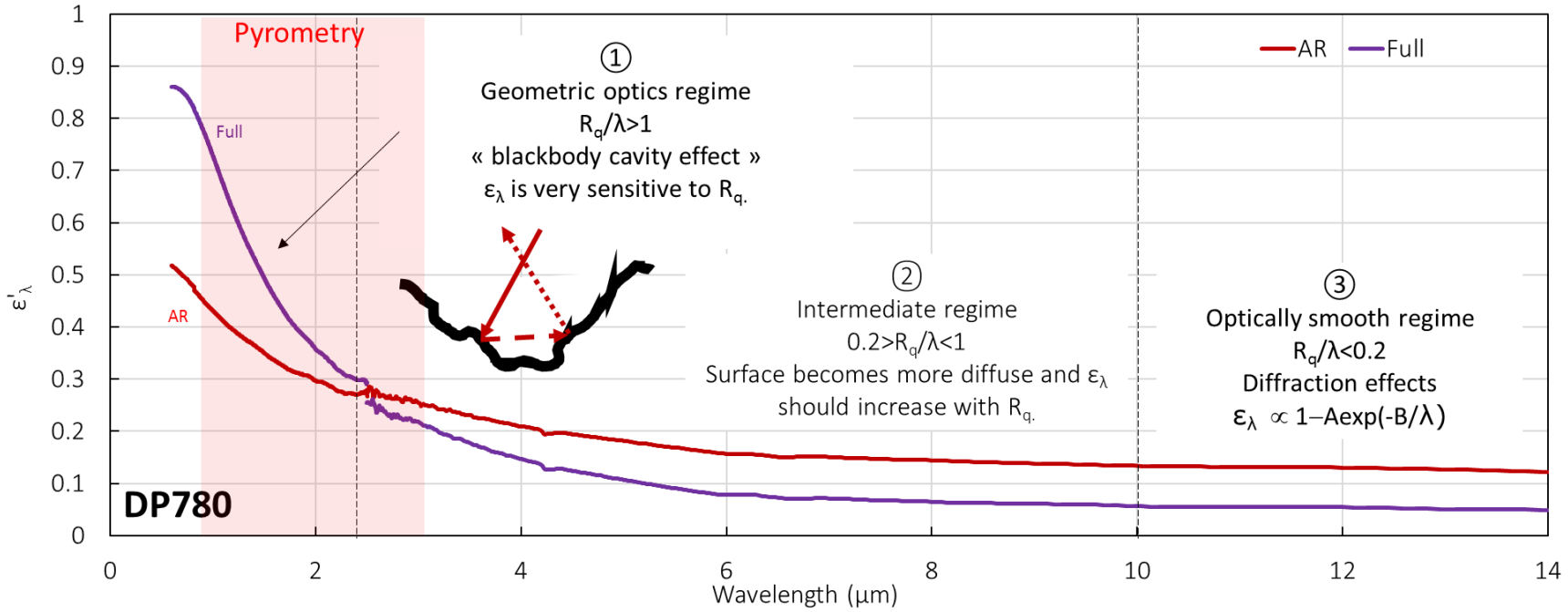

Figure E-1: Comparison of DP780 emissivity results with Wen and Mudawar's theory [57]